Chapter 5
Fluid-Structure Interaction: Variational Formulation

5.1 Introduction

In the previous chapter, we studied some of the basics of the finite element variational formulation for a transient convection-diffusion-reaction equation, which forms a canonical form for the nonlinear fluid-structure interaction equations. In this chapter, we apply the variational formulation to the separate equations governing the fluid and structural domains which were discussed in Section 3.4. We present the variational form of the Navier-Stokes equations written in ALE framework (Eqs. (3.94-3.95)) for the fluid and the structural dynamics equation (Eq. (3.79)) written in the Lagrangian coordinate system along with the boundary conditions mentioned in Section 3.4.4. We carry forward the notations defined in Section 3.4 in this chapter.

5.2 Weak Variational Form for Fluid-Structure Interaction

As mentioned in the previous chapters, fluid-structure interaction problems involve the coupling of two fields- flow and structure. In the current context, we will consider an incompressible Newtonian fluid with a three-dimensional structure for the variational formulation. However, the variational framework is general in its application and can be applied to any differential equation.

5.2.1 Trial and Test Function Spaces

For writing the weak formulations of the equations discussed above, we need to define the appropriate function spaces (see Appendix A4.1 for more details) to select the trial solution and test or weighting functions which are dependent on the spatial

coordinates. For the fluid equation, we define the following spaces

$$\mathscr{V}_{\boldsymbol{\psi}^{\mathrm{f}}} = \{\boldsymbol{\psi}^{\mathrm{f}} \in H^1(\varOmega^{\mathrm{f}}(t)) | \boldsymbol{\psi}^{\mathrm{f}} = \mathbf{0} \text{ on } \varGamma_D^{\mathrm{f}}\}, \tag{5.1}$$

$$\mathscr{V}_q = \{q \in L^2(\varOmega^{\mathrm{f}}(t))\}, \tag{5.2}$$

$$\mathscr{S}_{\boldsymbol{v}^{\mathrm{f}}} = \{\boldsymbol{v}^{\mathrm{f}} \in H^1(\varOmega^{\mathrm{f}}(t)) | \boldsymbol{v}^{\mathrm{f}} = \boldsymbol{v}_D^{\mathrm{f}} \text{ on } \varGamma_D^{\mathrm{f}}\}, \tag{5.3}$$

$$\mathscr{S}_p = \{p \in L^2(\varOmega^{\mathrm{f}}(t))\}, \tag{5.4}$$

where $\mathscr{V}_{\boldsymbol{\psi}^{\mathrm{f}}}$ and $\mathscr{V}_q$ denote the test function spaces for the momentum and continuity equations respectively and $\mathscr{S}_{\boldsymbol{v}^{\mathrm{f}}}$ and $\mathscr{S}_p$ denote the spaces from where we select the trial solution for velocity and pressure respectively.

Similarly, for the structural equation, we define the following function spaces

$$\mathscr{V}_{\boldsymbol{\psi}^{\mathrm{s}}} = \{\boldsymbol{\psi}^{\mathrm{s}} \in H^1(\varOmega^{\mathrm{s}}) | \boldsymbol{\psi}^{\mathrm{s}} = \mathbf{0} \text{ on } \varGamma_D^{\mathrm{s}}\}, \tag{5.5}$$

$$\mathscr{S}_{\boldsymbol{v}^{\mathrm{s}}} = \{\boldsymbol{v}^{\mathrm{s}} \in H^1(\varOmega^{\mathrm{s}}) | \boldsymbol{v}^{\mathrm{s}} = \boldsymbol{v}_D^{\mathrm{s}} \text{ on } \varGamma_D^{\mathrm{s}}\}, \tag{5.6}$$

where $\mathscr{V}_{\boldsymbol{\psi}^{\mathrm{s}}}$ and $\mathscr{S}_{\boldsymbol{v}^{\mathrm{s}}}$ denote the test function and trial solution spaces for the structural velocity respectively.

For the mesh equation, the following spaces are defined

$$\mathscr{V}_{\boldsymbol{\psi}^{\mathrm{m}}} = \{\boldsymbol{\psi}^{\mathrm{m}} \in H^1(\varOmega^{\mathrm{f}}) | \boldsymbol{\psi}^{\mathrm{m}} = \mathbf{0} \text{ on } \varGamma_D^{\mathrm{m}}\}, \tag{5.7}$$

$$\mathscr{S}_{\boldsymbol{u}^{\mathrm{f}}} = \{\boldsymbol{u}^{\mathrm{f}} \in H^1(\varOmega^{\mathrm{f}}) | \boldsymbol{u}^{\mathrm{f}} = \boldsymbol{u}_D^{\mathrm{f}} \text{ on } \varGamma_D^{\mathrm{m}}\}. \tag{5.8}$$

Now that we have the appropriate spaces to select the weighting functions and trial solution, we are ready to form the weak form of the flow and structural equations.

5.2.2 Weak Formulation for FSI

In this section, we derive the weak or variational form for the coupled fluid-structure equations. Let us begin with the incompressible Navier-Stokes equations (Eqs. (3.94-3.95)). The weak form is written by multiplying the equation by a weighting function and then integrating it over the whole domain. Thus, for the flow equations,

$$\int_{\varOmega^{\mathrm{f}}(t)} \left(\rho^{\mathrm{f}} \frac{\partial \boldsymbol{v}^{\mathrm{f}}}{\partial t} \bigg|_{\chi} + \rho^{\mathrm{f}} (\boldsymbol{v}^{\mathrm{f}} - \boldsymbol{w}) \cdot \nabla \boldsymbol{v}^{\mathrm{f}} - \nabla \cdot \boldsymbol{\sigma}^{\mathrm{f}} \right) \cdot \boldsymbol{\psi}^{\mathrm{f}} d\varOmega = \int_{\varOmega^{\mathrm{f}}(t)} \rho^{\mathrm{f}} \boldsymbol{b}^{\mathrm{f}} \cdot \boldsymbol{\psi}^{\mathrm{f}} d\varOmega, \tag{5.9}$$

$$\int_{\varOmega^{\mathrm{f}}(t)} (\nabla \cdot \boldsymbol{v}^{\mathrm{f}}) q d\varOmega = 0, \tag{5.10}$$

Notice that there are higher order derivatives for velocity in the term $\nabla \cdot \boldsymbol{\sigma}^{\mathrm{f}}$ which makes the requirement for the velocity as $\boldsymbol{v}^{\mathrm{f}} \in H^2(\varOmega^{\mathrm{f}}(t))$. Therefore, using Green's identity and Gauss' divergence theorem, we relax this requirement.

$$\int_{\Omega^{\mathrm{f}}(t)} \left(\rho^{\mathrm{f}} \frac{\partial \boldsymbol{v}^{\mathrm{f}}}{\partial t} \bigg|_{\chi} + \rho^{\mathrm{f}} (\boldsymbol{v}^{\mathrm{f}} - \boldsymbol{w}) \cdot \nabla \boldsymbol{v}^{\mathrm{f}} \right) \cdot \boldsymbol{\psi}^{\mathrm{f}} d\Omega + \int_{\Omega^{\mathrm{f}}(t)} \boldsymbol{\sigma}^{\mathrm{f}} : \nabla \boldsymbol{\psi}^{\mathrm{f}} d\Omega$$

$$= \int_{\Omega^{\mathrm{f}}(t)} \rho^{\mathrm{f}} \boldsymbol{b}^{\mathrm{f}} \cdot \boldsymbol{\psi}^{\mathrm{f}} d\Omega + \int_{\Gamma_D^{\mathrm{f}}} \boldsymbol{\sigma}^{\mathrm{f}} \cdot \boldsymbol{\psi}^{\mathrm{f}} d\Gamma + \int_{\Gamma_N^{\mathrm{f}}} \boldsymbol{\sigma}_N^{\mathrm{f}} \cdot \boldsymbol{\psi}^{\mathrm{f}} d\Gamma + \int_{\Gamma(t)} (\boldsymbol{\sigma}^{\mathrm{f}} \cdot \boldsymbol{n}^{\mathrm{f}}) \cdot \boldsymbol{\psi}^{\mathrm{f}} d\Gamma,$$

$$(5.11)$$

$$\int_{\Omega^{\mathrm{f}}(t)} (\nabla \cdot \boldsymbol{v}^{\mathrm{f}}) q \, d\Omega = 0. \tag{5.12}$$

Now, the continuity requirement on the velocity is $H^1(\Omega^{\mathrm{f}}(t))$ and the definitions of the function spaces in Section 5.2.1 can be employed. Recalling that $\boldsymbol{\psi}^{\mathrm{f}} = \boldsymbol{0}$ on Γ_D^{f},

$$\int_{\Omega^{\mathrm{f}}(t)} \left(\rho^{\mathrm{f}} \frac{\partial \boldsymbol{v}^{\mathrm{f}}}{\partial t} \bigg|_{\chi} + \rho^{\mathrm{f}} (\boldsymbol{v}^{\mathrm{f}} - \boldsymbol{w}) \cdot \nabla \boldsymbol{v}^{\mathrm{f}} \right) \cdot \boldsymbol{\psi}^{\mathrm{f}} d\Omega + \int_{\Omega^{\mathrm{f}}(t)} \boldsymbol{\sigma}^{\mathrm{f}} : \nabla \boldsymbol{\psi}^{\mathrm{f}} d\Omega$$

$$= \int_{\Omega^{\mathrm{f}}(t)} \rho^{\mathrm{f}} \boldsymbol{b}^{\mathrm{f}} \cdot \boldsymbol{\psi}^{\mathrm{f}} d\Omega + \int_{\Gamma_N^{\mathrm{f}}} \boldsymbol{\sigma}_N^{\mathrm{f}} \cdot \boldsymbol{\psi}^{\mathrm{f}} d\Gamma + \int_{\Gamma(t)} (\boldsymbol{\sigma}^{\mathrm{f}} \cdot \boldsymbol{n}^{\mathrm{f}}) \cdot \boldsymbol{\psi}^{\mathrm{f}} d\Gamma, \tag{5.13}$$

$$\int_{\Omega^{\mathrm{f}}(t)} (\nabla \cdot \boldsymbol{v}^{\mathrm{f}}) q \, d\Omega = 0. \tag{5.14}$$

We can combine the weak form of the momentum and continuity equations to write the variational statement as: find $[\boldsymbol{v}^{\mathrm{f}}, p] \in \mathscr{S}_{\boldsymbol{v}^{\mathrm{f}}} \times \mathscr{S}_p$ such that $\forall [\boldsymbol{\psi}^{\mathrm{f}}, q] \in \mathscr{V}_{\boldsymbol{\psi}^{\mathrm{f}}} \times \mathscr{V}_q$,

$$\int_{\Omega^{\mathrm{f}}(t)} \left(\rho^{\mathrm{f}} \frac{\partial \boldsymbol{v}^{\mathrm{f}}}{\partial t} \bigg|_{\chi} + \rho^{\mathrm{f}} (\boldsymbol{v}^{\mathrm{f}} - \boldsymbol{w}) \cdot \nabla \boldsymbol{v}^{\mathrm{f}} \right) \cdot \boldsymbol{\psi}^{\mathrm{f}} d\Omega + \int_{\Omega^{\mathrm{f}}(t)} \boldsymbol{\sigma}^{\mathrm{f}} : \nabla \boldsymbol{\psi}^{\mathrm{f}} d\Omega$$

$$+ \int_{\Omega^{\mathrm{f}}(t)} (\nabla \cdot \boldsymbol{v}^{\mathrm{f}}) q \, d\Omega = \int_{\Omega^{\mathrm{f}}(t)} \rho^{\mathrm{f}} \boldsymbol{b}^{\mathrm{f}} \cdot \boldsymbol{\psi}^{\mathrm{f}} d\Omega + \int_{\Gamma_N^{\mathrm{f}}} \boldsymbol{\sigma}_N^{\mathrm{f}} \cdot \boldsymbol{\psi}^{\mathrm{f}} d\Gamma + \int_{\Gamma(t)} (\boldsymbol{\sigma}^{\mathrm{f}} \cdot \boldsymbol{n}^{\mathrm{f}}) \cdot \boldsymbol{\psi}^{\mathrm{f}} d\Gamma.$$

$$(5.15)$$

Proceeding in a similar way for the structural equation, we can write the variational statement as: find $\boldsymbol{v}^{\mathrm{s}} \in \mathscr{S}_{\boldsymbol{v}^{\mathrm{s}}}$ such that $\forall \boldsymbol{\psi}^{\mathrm{s}} \in \mathscr{V}_{\boldsymbol{\psi}^{\mathrm{s}}}$,

$$\int_{\Omega^{\mathrm{s}}} \left(\rho^{\mathrm{s}} \frac{\partial \boldsymbol{v}^{\mathrm{s}}}{\partial t} \right) \cdot \boldsymbol{\psi}^{\mathrm{s}} d\Omega + \int_{\Omega^{\mathrm{s}}} \boldsymbol{\sigma}^{\mathrm{s}} : \nabla \boldsymbol{\psi}^{\mathrm{s}} d\Omega$$

$$= \int_{\Omega^{\mathrm{s}}} \rho^{\mathrm{s}} \boldsymbol{b}^{\mathrm{s}} \cdot \boldsymbol{\psi}^{\mathrm{s}} d\Omega + \int_{\Gamma_N^{\mathrm{s}}} \boldsymbol{\sigma}_N^{\mathrm{s}} \cdot \boldsymbol{\psi}^{\mathrm{s}} d\Gamma + \int_{\Gamma} (\boldsymbol{\sigma}^{\mathrm{s}} \cdot \boldsymbol{n}^{\mathrm{s}}) \cdot \boldsymbol{\psi}^{\mathrm{s}} d\Gamma. \tag{5.16}$$

Similarly for the mesh equation, we get: find $\boldsymbol{u}^{\mathrm{f}} \in \mathscr{S}_{\boldsymbol{u}^{\mathrm{f}}}$ such that $\forall \boldsymbol{\psi}^{\mathrm{m}} \in \mathscr{V}_{\boldsymbol{\psi}^{\mathrm{m}}}$,

$$\int_{\Omega^{\mathrm{f}}} \nabla \boldsymbol{\psi}^{\mathrm{m}} : \boldsymbol{\sigma}^{\mathrm{m}} d\Omega = 0, \tag{5.17}$$

where $\boldsymbol{\sigma}^{\mathrm{m}} = (1 + k_{\mathrm{m}})[\nabla \boldsymbol{u}^{\mathrm{f}} + (\nabla \boldsymbol{u}^{\mathrm{f}})^T + (\nabla \cdot \boldsymbol{u}^{\mathrm{f}}) \boldsymbol{I}]$.

Remark 5.1. The velocity continuity condition at the fluid-structure interface is satisfied by moving the fluid domain such that the velocity of the fluid domain at the

fluid-structure boundary is the same as the structural velocity at the boundary. After solving for the fluid displacement field $\boldsymbol{u}^{\mathrm{f}}$, the spatial coordinates are updated as $\boldsymbol{x} = \boldsymbol{\chi} + \boldsymbol{u}^{\mathrm{f}}(\boldsymbol{\chi},t)$ for all $\boldsymbol{x} \in \Omega^{\mathrm{f}}(t)$ and $\boldsymbol{\chi} \in \Omega^{\mathrm{f}}(0)$.

5.3 Semi-Discrete Temporal Discretization

As the independent variables in the FSI equations are the spatial and temporal coordinates, we need to discretize the domain in both space and time. One way of doing this is to define the trial and test function spaces in the weak form such that they are space and time dependent. Such methods lead to what are called space-time finite element methods. In the present case, we will utilize a simpler approach of discretizing the temporal variable by Taylor series (similar to finite difference methods) such that the trial and test function spaces have only spatial dependence. An example of such discrete time stepping is the generalized-α time integration [44, 111] technique for integrating in time from time step t^{n} to $t^{\mathrm{n}+1}$. While one can use any other time integration technique, we will present the formulation using the generalized-α method for the rest of this chapter.

5.3.1 Generalized-α Time Integration

Here, we discuss the generalized-α [44, 111] predictor-corrector method for the temporal discretization. It enables a user-controlled high frequency damping via a single parameter called the spectral radius ρ_∞, which allows for a coarser discretization in time. We solve the equation at the time interval $\mathrm{n} + \alpha$ while integrating the equation from n to n$+1$ in time. Suppose the equation can be written as $G(\partial_t u^{\mathrm{n}+\alpha_{\mathrm{m}}}, u^{\mathrm{n}+\alpha}, \phi^{\mathrm{n}+\alpha}) = 0$, where $G(\cdot)$ can be a nonlinear function of the variable ϕ and its first and second-order derivatives, i.e., $u = \partial_t \phi$ and $\partial_t u = \partial_{tt}^2 \phi$, respectively. The expressions for the variables and their derivatives in the equation can be written as

$$\phi^{\mathrm{n}+1} = \phi^{\mathrm{n}} + \Delta t u^{\mathrm{n}} + \Delta t^2 \left(\beta \partial_t u^{\mathrm{n}+1} + (1/2 - \beta) \partial_t u^{\mathrm{n}} \right), \tag{5.18}$$

$$u^{\mathrm{n}+1} = u^{\mathrm{n}} + \Delta t \left(\gamma \partial_t u^{\mathrm{n}+1} + (1 - \gamma) \partial_t u^{\mathrm{n}} \right), \tag{5.19}$$

$$\partial_t u^{\mathrm{n}+\alpha_{\mathrm{m}}} = \partial_t u^{\mathrm{n}} + \alpha_{\mathrm{m}} \left(\partial_t u^{\mathrm{n}+1} - \partial_t u^{\mathrm{n}} \right), \tag{5.20}$$

$$u^{\mathrm{n}+\alpha} = u^{\mathrm{n}} + \alpha (u^{\mathrm{n}+1} - u^{\mathrm{n}}), \tag{5.21}$$

$$\phi^{\mathrm{n}+\alpha} = \phi^{\mathrm{n}} + \alpha (\phi^{\mathrm{n}+1} - \phi^{\mathrm{n}}), \tag{5.22}$$

where Δt is the time step size, α_{m}, α, β and γ are defined as

$$\alpha_m = \frac{1}{2}\left(\frac{3-\rho_\infty}{1+\rho_\infty}\right), \quad \alpha = \frac{1}{1+\rho_\infty}, \quad \beta = \frac{1}{4}(1+\alpha_m - \alpha)^2, \quad \gamma = \frac{1}{2} + \alpha_m - \alpha.$$

$$(5.23)$$

Note that the above time integration method simplifies to the following methods under the given conditions:

- Crank-Nicolson method: $\rho_\infty = 1$
- Gear's two-step method: $\rho_\infty = 0$
- Implicit Euler (Backward Euler) method: $\alpha = \alpha_m = \gamma = 1$

The predictor-corrector algorithm within a time step from n to n + 1 consists of the following steps:

1. Predict the variables at n + 1.
2. Evaluate the variables at the intermediate time interval $n + \alpha$.
3. Linearize the nonlinear equation $G(\partial_t u^{n+\alpha_m}, u^{n+\alpha}, \phi^{n+\alpha}) = 0$ with the help of Newton-Raphson method.
4. Calculate the increments in the variables by solving the linear system of equations.
5. Update the variables at $n + \alpha$.
6. Correct the variables at n + 1 and proceed to the next nonlinear iteration.

5.3.2 Semi-Discrete Temporal Discretization Applied to FSI

For the fluid equations, the generalized-α expressions for the fluid velocity v^f and acceleration $\partial_t v^f$ can be written as:

$$v^{f,n+1} = v^{f,n} + \Delta t(\gamma^f \partial_t v^{f,n+1} + (1-\gamma^f)\partial_t v^{f,n}), \tag{5.24}$$

$$\partial_t v^{f,n+\alpha_m^f} = \partial_t v^{f,n} + \alpha_m^f(\partial_t v^{f,n+1} - \partial_t v^{f,n}), \tag{5.25}$$

$$v^{f,n+\alpha^f} = v^{f,n} + \alpha^f(v^{f,n+1} - v^{f,n}). \tag{5.26}$$

On the other hand, the expressions for the structural equation involving the structural velocity v^s, position φ^s and acceleration $\partial_t v^s$ are

$$\varphi^{s,n+1} = \varphi^{s,n} + \Delta t v^{s,n} + \Delta t^2\left(\left(\frac{1}{2} - \beta^s\right)\partial_t v^{s,n} + \beta^s \partial_t v^{s,n+1}\right), \tag{5.27}$$

$$v^{s,n+1} = v^{s,n} + \Delta t\left((1-\gamma^s)\partial_t v^{s,n} + \gamma^s \partial_t v^{s,n+1}\right), \tag{5.28}$$

$$\partial_t v^{s,n+\alpha_m^s} = \partial_t v^{s,n} + \alpha_m^s(\partial_t v^{s,n+1} - \partial_t v^{s,n}), \tag{5.29}$$

$$v^{n+\alpha^s} = v^{s,n} + \alpha^s(v^{s,n+1} - v^{s,n}), \tag{5.30}$$

$$\varphi^{n+\alpha^s} = \varphi^{s,n} + \alpha^s(\varphi^{s,n+1} - \varphi^{s,n}), \tag{5.31}$$

The equations written in the semi-discrete form are solved at the time level $t^{n+\alpha}$ and the values at t^{n+1} are updated via the predictor-corrector algorithm.

5.4 Finite Element Space Discretization for FSI

The next step is to select finite element spaces $\mathscr{V}^h$ and $\mathscr{S}^h$ from the space of test and trial functions $\mathscr{V}$ and $\mathscr{S}$ respectively. We discretize the domain Ω into non-intersecting finite elements $\Omega = \cup_{e=1}^{n_{el}} \Omega^e$. The discrete spaces for trial and test functions for the fluid equations are defined as

$$\mathscr{V}_{\psi^f}^h = \{\psi_h^f \in H^1(\Omega^f(t^{n+1})) | \psi_h^f|_{\Omega^e} \in \mathbb{P}_m(\Omega^e) \forall e \text{ and } \psi_h^f = \mathbf{0} \text{ on } \Gamma_D^f\}, \quad (5.32)$$

$$\mathscr{V}_q^h = \{q_h \in L^2(\Omega^f(t^{n+1})) | q_h|_{\Omega^e} \in \mathbb{P}_m(\Omega^e) \forall e\}, \quad (5.33)$$

$$\mathscr{S}_{v^f}^h = \{v_h^f \in H^1(\Omega^f(t^{n+1})) | v_h^f|_{\Omega^e} \in \mathbb{P}_m(\Omega^e) \forall e \text{ and } v_h^f = v_D^f \text{ on } \Gamma_D^f\}, \quad (5.34)$$

$$\mathscr{S}_p^h = \{p_h \in L^2(\Omega^f(t^{n+1})) | p_h|_{\Omega^e} \in \mathbb{P}_m(\Omega^e) \forall e\}, \quad (5.35)$$

where $\mathbb{P}_m(\Omega^e)$ is the space of polynomials of degree $\leq m$.

The finite element variational statement for the element Ω^e for the fluid equations can thus be written as: find $[v_h^{f,n+\alpha^f}, p_h^{n+1}] \in \mathscr{S}_{v^f}^h \times \mathscr{S}_p^h$ such that $\forall [\psi_h^f, q_h] \in \mathscr{V}_{\psi^f}^h \times \mathscr{V}_q^h$,

$$\int_{\Omega^f(t^{n+1})} \left(\rho^f \partial_t v_h^{f,n+\alpha_m^f} \Big|_{\chi} + \rho^f (v_h^{f,n+\alpha^f} - w) \cdot \nabla v_h^{f,n+\alpha^f} \right) \cdot \psi_h^f d\Omega$$

$$+ \int_{\Omega^f(t^{n+1})} \sigma_h^{f,n+\alpha^f} : \nabla \psi_h^f d\Omega + \int_{\Omega^f(t^{n+1})} (\nabla \cdot v_h^{f,n+\alpha^f}) q_h d\Omega$$

$$= \int_{\Omega^f(t^{n+1})} \rho^f b_h^{f,n+\alpha^f} \cdot \psi_h^f d\Omega + \int_{\Gamma_N^f} \sigma_N^{f,n+\alpha^f} \cdot \psi_h^f d\Gamma + \int_{\Gamma(t^{n+1})} (\sigma_h^{f,n+\alpha^f} \cdot n^f) \cdot \psi_h^f d\Gamma.$$

$$(5.36)$$

The above equation consists of the Galerkin formulation without any stabilization terms for the fluid domain. For it to be stable for convection-dominated regimes, one needs compatible polynomial spaces for velocity-pressure coupling or stabilization terms (see Appendix A5.1). Here, we employ Petrov-Galerkin stabilization for stability in convection-dominated regimes. The extra stabilization terms are introduced as:

$$\int_{\Omega^f(t^{n+1})} \left(\rho^f \partial_t v_h^{f,n+\alpha_m^f} \Big|_{\chi} + \rho^f (v_h^{f,n+\alpha^f} - w) \cdot \nabla v_h^{f,n+\alpha^f} \right) \cdot \psi_h^f d\Omega$$

$$+ \int_{\Omega^f(t^{n+1})} \sigma_h^{f,n+\alpha^f} : \nabla \psi_h^f d\Omega + \sum_{e=1}^{n_{el}} \int_{\Omega^e} \tau_m (\rho^f (v_h^{f,n+\alpha^f} - w) \cdot \nabla \psi_h^f + \nabla q_h) \cdot R_m d\Omega^e$$

$$+ \int_{\Omega^f(t^{n+1})} (\nabla \cdot \boldsymbol{v}_h^{f,n+\alpha^f}) q_h d\Omega + \sum_{e=1}^{n_{el}} \int_{\Omega^e} \nabla \cdot \boldsymbol{\psi}_h^f \tau_c R_c d\Omega^e$$

$$= \int_{\Omega^f(t^{n+1})} \rho^f \boldsymbol{b}_h^{f,n+\alpha^f} \cdot \boldsymbol{\psi}_h^f d\Omega + \int_{\Gamma_N^f} \boldsymbol{\sigma}_N^{f,n+\alpha^f} \cdot \boldsymbol{\psi}_h^f d\Gamma + \int_{\Gamma(t^{n+1})} (\boldsymbol{\sigma}_h^{f,n+\alpha^f} \cdot \boldsymbol{n}^f) \cdot \boldsymbol{\psi}_h^f d\Gamma.$$

$$(5.37)$$

where the second line represents the stabilization term for the momentum equation and the second term in the third line depicts the same for the continuity equation. R_m and R_c are the residual of the momentum and continuity equations respectively. The stabilization parameters τ_m and τ_c are the least-squares metrics added to the element-level integrals [193, 34, 209, 67] defined as

$$\tau_m = \left[\left(\frac{2\rho^f}{\Delta t}\right)^2 + (\rho^f)^2 (\boldsymbol{v}_h^{f,n+\alpha^f} - \boldsymbol{w}) \cdot \boldsymbol{G}(\boldsymbol{v}_h^{f,n+\alpha^f} - \boldsymbol{w}) + C_I(\mu^f)^2 \boldsymbol{G} : \boldsymbol{G} \right]^{-1/2},$$

$$(5.38)$$

$$\tau_c = \frac{1}{8 \mathrm{tr}(\boldsymbol{G}) \tau_m},$$

$$(5.39)$$

where C_I is a constant derived from inverse estimates [83], $\mathrm{tr}()$ denotes the trace and $\boldsymbol{G}$ is the contravariant metric tensor given by

$$\boldsymbol{G} = \left(\frac{\partial \boldsymbol{\xi}}{\partial \boldsymbol{x}}\right)^T \frac{\partial \boldsymbol{\xi}}{\partial \boldsymbol{x}},$$

$$(5.40)$$

where $\boldsymbol{x}$ and $\boldsymbol{\xi}$ are the physical and parametric coordinates respectively.

Coming to the structural equation, we define the finite spaces as follows:

$$\mathscr{V}_{\boldsymbol{\psi}^s}^h = \{\boldsymbol{\psi}_h^s \in H^1(\Omega^s) \big| \boldsymbol{\psi}_h^s|_{\Omega^e} \in \mathbb{P}_m(\Omega^e) \forall e \text{ and } \boldsymbol{\psi}_h^s = \boldsymbol{0} \text{ on } \Gamma_D^s\}, \qquad (5.41)$$

$$\mathscr{S}_{\boldsymbol{v}^s}^h = \{\boldsymbol{v}_h^s \in H^1(\Omega^s) \big| \boldsymbol{v}_h^s|_{\Omega^e} \in \mathbb{P}_m(\Omega^e) \forall e \text{ and } \boldsymbol{v}_h^s = \boldsymbol{v}_D^s \text{ on } \Gamma_D^s\}, \qquad (5.42)$$

and the finite element variational statement is written as: find $\boldsymbol{v}_h^{s,n+\alpha^s} \in \mathscr{S}_{\boldsymbol{v}^s}^h$ such that $\forall \boldsymbol{\psi}_h^s \in \mathscr{V}_{\boldsymbol{\psi}^s}^h$,

$$\int_{\Omega^s} \left(\rho^s \partial_t \boldsymbol{v}_h^{s,n+\alpha_m^s}\right) \cdot \boldsymbol{\psi}_h^s d\Omega + \int_{\Omega^s} \boldsymbol{\sigma}_h^{s,n+\alpha^s} : \nabla \boldsymbol{\psi}_h^s d\Omega$$

$$= \int_{\Omega^s} \rho^s \boldsymbol{b}_h^{s,n+\alpha^s} \cdot \boldsymbol{\psi}_h^s d\Omega + \int_{\Gamma_N^s} \boldsymbol{\sigma}_N^{s,n+\alpha^s} \cdot \boldsymbol{\psi}_h^s d\Gamma + \int_\Gamma (\boldsymbol{\sigma}_h^{s,n+\alpha^s} \cdot \boldsymbol{n}^s) \cdot \boldsymbol{\psi}_h^s d\Gamma. \quad (5.43)$$

Similarly for the mesh equation, we define the finite element spaces and the variational statement is written as: find $\boldsymbol{u}_h^{f,n+1} \in \mathscr{S}_{\boldsymbol{u}^f}^h$ such that $\forall \boldsymbol{\psi}_h^m \in \mathscr{V}_{\boldsymbol{\psi}^m}^h$,

$$\int_{\Omega^f} \nabla \boldsymbol{\psi}_h^m : \boldsymbol{\sigma}_h^{m,n+1} d\Omega = 0. \qquad (5.44)$$

5.5 Matrix Form of the Linear System of Equations

After the assembly across all the finite elements and mapping to the global nodes for the FSI equations and utilizing linearization strategies like Newton-Raphson, the finite element formulation can be finally written in the matrix form. For the fluid equations, the matrix form looks like the following

$$\begin{pmatrix} \boldsymbol{K}^{\mathrm{f}} & -\boldsymbol{G}^{\mathrm{f}} \\ (\boldsymbol{G}^{\mathrm{f}})^{T} & \boldsymbol{C}^{\mathrm{f}} \end{pmatrix} \begin{pmatrix} \Delta \underline{\boldsymbol{v}}_{\mathrm{h}}^{\mathrm{f},\mathrm{n}+\alpha^{\mathrm{f}}} \\ \Delta \underline{p}_{\mathrm{h}}^{\mathrm{n}+1} \end{pmatrix} = \begin{pmatrix} \boldsymbol{F}^{\mathrm{f}} \\ \boldsymbol{0} \end{pmatrix}, \tag{5.45}$$

where $\boldsymbol{K}^{\mathrm{f}}$ consists of the transient, convection, viscous and convective stabilization terms, $\boldsymbol{G}^{\mathrm{f}}$ is the gradient operator, $(\boldsymbol{G}^{\mathrm{f}})^{T}$ is the divergence operator for the continuity equation and $\boldsymbol{C}^{\mathrm{f}}$ consists of the stabilization terms corresponding to pressure-pressure coupling. The increments in the velocity and pressure for the Newton-Raphson iterative procedure are given by $\Delta \underline{\boldsymbol{v}}_{\mathrm{h}}^{\mathrm{f},\mathrm{n}+\alpha^{\mathrm{f}}}$ and $\Delta \underline{p}_{\mathrm{h}}^{\mathrm{n}+1}$ respectively.

Similarly, for the structural and mesh equation, we get the following matrix forms:

$$(\boldsymbol{K}^{\mathrm{s}}) \left(\Delta \underline{\boldsymbol{v}}_{\mathrm{h}}^{\mathrm{s},\mathrm{n}+\alpha^{\mathrm{s}}} \right) = (\boldsymbol{F}^{\mathrm{s}}), \tag{5.46}$$

$$(\boldsymbol{K}^{\mathrm{m}}) \left(\Delta \underline{\boldsymbol{u}}_{\mathrm{h}}^{\mathrm{f},\mathrm{n}+1} \right) = (\boldsymbol{0}), \tag{5.47}$$

where $\boldsymbol{K}^{\mathrm{s}}$ and $\boldsymbol{K}^{\mathrm{m}}$ are the linearized matrices for the respective equations.

5.6 Solution Procedure

After the temporal and spatial discretization of the FSI equations, they can be solved by either monolithic or partitioned solution strategies. These strategies are discussed in the current section. In the monolithic strategy, the whole problem is considered as a single field and all the components are advanced simultaneously in time. On the other hand, *partitioning* is the process of spatial separation of the discrete model into the interacting components which are called *partitions*. On the other hand, the temporal discretization can also be decomposed into what is called *splitting* within a particular time step size (See Fig. 5.1). The time splitting can be additive or multiplicative.

To understand this concept, consider a very simplified problem of two fields X and Y coupled with each other and advancing in time as shown in Fig. 5.2. Fields X and Y solve for the variables $x(t)$ and $y(t)$ respectively and are coupled as follows:

$$5\dot{x} + 2x - 3y = f(t), \tag{5.48}$$
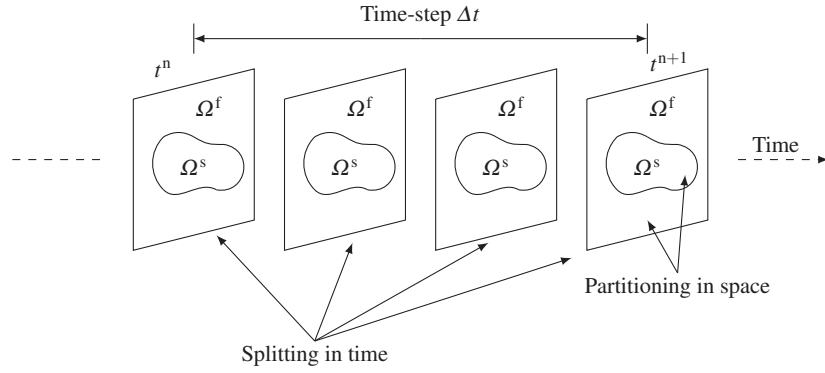$$\dot{y} + 8y - 7x = g(t), \tag{5.49}$$

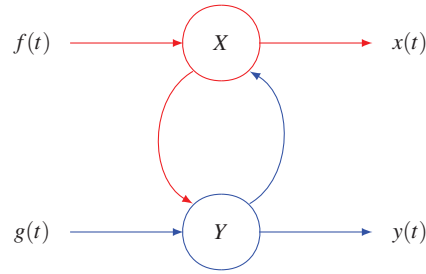**Fig. 5.1** Partition in spatial and splitting in the temporal discretizations.

Fig. 5.2 Coupled fields X and Y advancing in time t.

where $f(t)$ and $g(t)$ are the applied forces on the system. Discretizing the system in time using backward Euler,

$$\begin{pmatrix} 5+2\Delta t & -3\Delta t \\ -7\Delta t & 1+8\Delta t \end{pmatrix} \begin{pmatrix} x^{n+1} \\ y^{n+1} \end{pmatrix} = \begin{pmatrix} \Delta t f(t^{n+1})+5x^n \\ \Delta t g(t^{n+1})+y^n \end{pmatrix} \tag{5.50}$$

whre Δt is the time step size. If one solves Eq. (5.50) directly in a time step, the technique is termed as monolithic.

For a partitioned procedure, both the fields are advanced in time separately. It consists of a predictor-corrector algorithm as follows in a particular time step:

1. Predictor step: $y_P^{n+1} = y^n$ or $y_P^{n+1} = y^n + \Delta t \dot{y}^n$
2. Transfer of data: Send the predicted value to the second field
3. Advance the second field:

$$x^{n+1} = \frac{1}{5+2\Delta t}(\Delta t f(t^{n+1})+5x^n+3\Delta t y_P^{n+1}) \tag{5.51}$$

4. Corrector step:

$$y^{n+1} = \frac{1}{1+8\Delta t}\left(\Delta t g(t^{n+1}) + y^n + 7\Delta t x^{n+1}\right) \qquad (5.52)$$
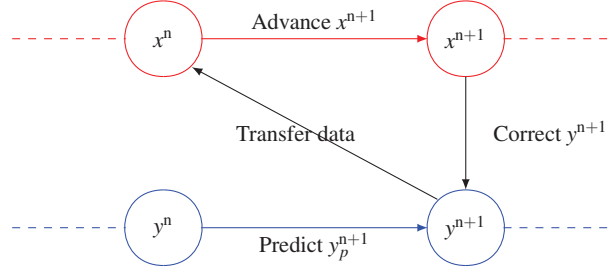
Fig. 5.3 Partitioned staggered technique for coupled fields X and Y advancing in time t.
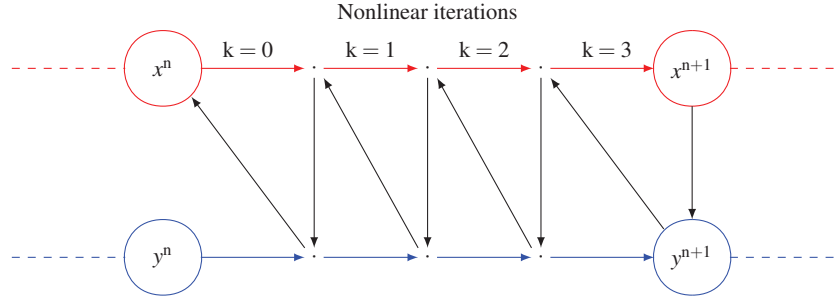
Fig. 5.4 Partitioned iterative staggered technique for coupled fields X and Y advancing in time t.

The above algorithm is called *staggered partitioned* procedure (Fig. 5.3). For linear problems, it is observed that staggering does not harm stability and accuracy of the problem, given the condition that the predictor is chosen properly. But for more general nonlinear problems, stability could become an issue. On the other hand, accuracy is degraded compared to the same problem solved by a monolithic scheme. This can be resolved by iterating the staggered procedure within a time step so that the scheme now forms a predictor-multicorrector format (Fig. 5.4). For nonlinear problems, these iterations help in the convergence and capture of the nonlinearities. However, these multiple iterations add to the computational cost and a monolithic scheme could be more advantageous for some problems in that case. Therefore, there is a tradeoff based on the type of problem being solved. Further details can be found in [129, 64]. Next, we briefly look into how these strategies differ for an FSI problem, before going into the details in the upcoming chapters.

5.6.1 Monolithic Solution for FSI

In the monolithic technique, the fluid and structural velocities are advanced in time simultaneously and both the fluid and structure are considered as a combined field. Note that when written in a combined field form, the dynamic equilibrium at the fluid-structure interface is satisfied naturally and we don't need to worry about the transfer of forces along the interface. This technique will be discussed in more detail in Chapter 6.
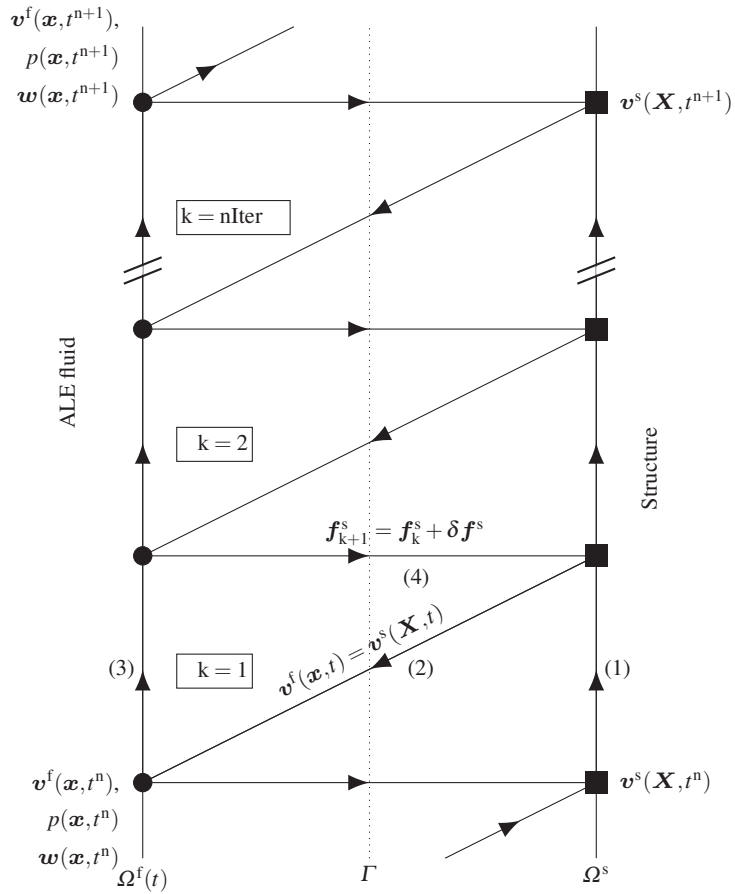

Fig. 5.5 Partitioned iterative staggered technique for coupled fluid-structure interaction system.

5.6.2 Partitioned Solution for FSI

In the partitioned procedure for FSI problems, we solve the fluid and structural fields separately and transfer the interface data between the fields. As the equations involved are nonlinear in nature, we opt for the predictor-multicorrector partitioned staggered procedure presented above. The matrices involved in the solution are given in Eqs. (5.45), (5.46) and (5.47) for the fluid, structure and mesh equations. The steps involved in a particular nonlinear iteration of the algorithm are given below:

1. Solve Eq. (5.46) for the predictor structural velocity $(v_{(k+1)}^{s,n+1})$ based on the fluid forces evaluated at the previous time step, $f_{(k)}^{s,n}$
2. Transfer the structural velocity at the fluid-structure interface to the fluid solver by maintaining the velocity continuity condition at the interface and satisfying the ALE mesh compatibility. This is carried out as follows:

   - Equate mesh displacement to the structural displacement at the interface

   $$u_{(k+1)}^{m,n+1} = u_{(k+1)}^{s,n+1}, \text{ on } \Gamma \qquad (5.53)$$

   - Equate fluid velocity to mesh velocity at the interface to satisfy conservation property of moving mesh elements in the fluid domain

   $$v_{(k+1)}^{f,n+\alpha^f} = w_{(k+1)}^{n+\alpha^f}, \text{ on } \Gamma, \qquad (5.54)$$

   where

   $$w_{(k+1)}^{n+\alpha^f} = \frac{u_{(k+1)}^{m,n+1} - u_{(k+1)}^{m,n}}{\Delta t} = v_{(k+1)}^{s,n+\alpha^s}, \text{ on } \Gamma \qquad (5.55)$$

3. Solve Eq. (5.47) for the displacements of the fluid nodes and calculate mesh velocity field; and solve Eq. (5.45) for getting the updated velocity $(v_{(k+1)}^{f,n+1})$ and pressure $(p_{(k+1)}^{n+1})$ and evaluate the fluid forces
4. Transfer the corrected fluid forces to the structural solver to satisfy the dynamic equilibrium at the fluid-structure interface, i.e., $f_{(k+1)}^{s,n+\alpha^s} = f_{(k)}^{s,n+\alpha^s} + \delta f^s$

The above steps form a nonlinear iteration. The fluid-structure coupling then advances in time at the end of the nonlinear iteration steps once the convergence criteria has been achieved. This scheme is shown in Fig. 5.5. The various challenges with the transfer of forces along the interface and the satisfaction of the equilibrium conditions have been discussed in detail in Chapter 7. Several techniques to ensure accurate and conservative transfer of data across the fluid-structure interface are also discussed.

To summarize, we began with the fluid-structure continuum equations and expressed the variational finite element form for the stabilized fluid system, structural system and mesh equation. We then briefly discussed the two main strategies for

solving the coupled FSI system while noting some of the major difference between them. In the next few chapters, we deal with these two approaches in further detail.

Appendix

A5.1 The Pressure-Velocity Coupling

Consider the Stokes equations for incompressible Newtonian flows in a domain $\Omega^{\mathrm{f}} \subset \mathbb{R}^d$ with a boundary Γ consisting of the Dirichlet and Neumann boundaries Γ_D and Γ_N respectively:

$$-\mu^{\mathrm{f}}\nabla^2 \boldsymbol{v}^{\mathrm{f}} + \nabla p = \rho^{\mathrm{f}}\boldsymbol{b}^{\mathrm{f}}, \qquad \text{on } \Omega^{\mathrm{f}}, \qquad (5.56)$$

$$\nabla \cdot \boldsymbol{v}^{\mathrm{f}} = 0, \qquad \text{on } \Omega^{\mathrm{f}}, \qquad (5.57)$$

$$\boldsymbol{v}^{\mathrm{f}} = \boldsymbol{v}_D^{\mathrm{f}}, \qquad \text{on } \Gamma_D^{\mathrm{f}}, \qquad (5.58)$$

$$-\nabla \boldsymbol{v}^{\mathrm{f}} \cdot \boldsymbol{n} + p\boldsymbol{n} = \boldsymbol{h}^{\mathrm{f}}, \qquad \text{on } \Gamma_N^{\mathrm{f}}, \qquad (5.59)$$

where $\boldsymbol{v}^{\mathrm{f}}$ and p are the fluid velocity and pressure respectively, $\boldsymbol{v}_D^{\mathrm{f}}$ and $\boldsymbol{h}^{\mathrm{f}}$ denote the Dirichlet and Neumann conditions respectively. The weak statement can be written as: find $[\boldsymbol{v}^{\mathrm{f}}, p] \in \mathscr{S}_{\boldsymbol{v}^{\mathrm{f}}} \times \mathscr{S}_p$ such that $\forall [\boldsymbol{\psi}^{\mathrm{f}}, q] \in \mathscr{V}_{\boldsymbol{\psi}^{\mathrm{f}}} \times \mathscr{V}_q$,

$$\int_{\Omega^{\mathrm{f}}} \nabla \boldsymbol{\psi}^{\mathrm{f}} : \left(\mu^{\mathrm{f}}\nabla \boldsymbol{v}^{\mathrm{f}} - p\boldsymbol{I} \right) d\Omega = \int_{\Omega^{\mathrm{f}}} \boldsymbol{\psi}^{\mathrm{f}} \cdot \rho^{\mathrm{f}}\boldsymbol{b}^{\mathrm{f}} d\Omega, \qquad (5.60)$$

$$\int_{\Omega^{\mathrm{f}}} q(\nabla \cdot \boldsymbol{v}^{\mathrm{f}}) d\Omega = 0, \qquad (5.61)$$

which in the compact form can be written as

$$a(\boldsymbol{\psi}^{\mathrm{f}}, \boldsymbol{v}^{\mathrm{f}}) + b(\boldsymbol{\psi}^{\mathrm{f}}, p) = (\boldsymbol{\psi}^{\mathrm{f}}, \rho^{\mathrm{f}}\boldsymbol{b}^{\mathrm{f}}), \qquad (5.62)$$

$$b(\boldsymbol{v}^{\mathrm{f}}, q) = 0, \qquad (5.63)$$

where

$$a(\boldsymbol{\psi}^{\mathrm{f}}, \boldsymbol{v}^{\mathrm{f}}) = \int_{\Omega^{\mathrm{f}}} \nabla \boldsymbol{\psi}^{\mathrm{f}} : \mu^{\mathrm{f}}\nabla \boldsymbol{v}^{\mathrm{f}} d\Omega, \qquad b(\boldsymbol{\psi}^{\mathrm{f}}, p) = \int_{\Omega^{\mathrm{f}}} \nabla \boldsymbol{\psi}^{\mathrm{f}} : (-p\boldsymbol{I}) d\Omega. \quad (5.64)$$

Remark 5.2. Equations (5.62) and (5.63) represent the saddle point of the Lagrangian functional

$$\mathscr{I}(\boldsymbol{\psi}^{\mathrm{f}}, q) = \frac{1}{2}a(\boldsymbol{\psi}^{\mathrm{f}}, \boldsymbol{\psi}^{\mathrm{f}}) + b(\boldsymbol{\psi}^{\mathrm{f}}, q) - (\boldsymbol{\psi}^{\mathrm{f}}, \rho^{\mathrm{f}}\boldsymbol{b}^{\mathrm{f}}). \qquad (5.65)$$

A saddle point problem is to find a solution $(\boldsymbol{v}^{\text{f}}, p)$ such that the functional is minimized with respect to the first argument and maximized with respect to the second one, i.e., $\mathscr{I}(\boldsymbol{v}^{\text{f}}, q) \leq \mathscr{I}(\boldsymbol{v}^{\text{f}}, p) \leq \mathscr{I}(\boldsymbol{\psi}^{\text{f}}, p)$.

Similarly, for each element domain Ω^e, the variational finite element discretization is written as: find $[\boldsymbol{v}_{\text{h}}^{\text{f}}, p_{\text{h}}] \in \mathscr{S}_{\boldsymbol{v}^{\text{f}}}^{\text{h}} \times \mathscr{S}_p^{\text{h}}$ such that $\forall [\boldsymbol{\psi}_{\text{h}}^{\text{f}}, q_{\text{h}}] \in \mathscr{V}_{\boldsymbol{\psi}^{\text{f}}}^{\text{h}} \times \mathscr{V}_q^{\text{h}}$,

$$\int_{\Omega^e} \nabla \boldsymbol{\psi}_{\text{h}}^{\text{f}} : \left(\mu^{\text{f}} \nabla \boldsymbol{v}_{\text{h}}^{\text{f}} - p_{\text{h}} \boldsymbol{I} \right) d\Omega = \int_{\Omega^e} \boldsymbol{\psi}_{\text{h}}^{\text{f}} \cdot \rho^{\text{f}} \boldsymbol{b}^{\text{f}} d\Omega, \tag{5.66}$$

$$\int_{\Omega^e} q_{\text{h}} (\nabla \cdot \boldsymbol{v}_{\text{h}}^{\text{f}}) d\Omega = 0. \tag{5.67}$$

Using the polynomial approximation as $v_{\text{h}(j)}^{\text{f}} = \sum_{i=1}^{nen} N_i v_{i(j)}^{\text{f}}$ for each velocity component j and $p_{\text{h}} = \sum_{i=1}^{nen} M_i p_i$ and using the Galerkin formulation, the final linear matrix system after assembling the contributions from each element can be written as

$$\begin{pmatrix} \boldsymbol{A} & -\boldsymbol{B} \\ \boldsymbol{B}^T & \boldsymbol{0} \end{pmatrix} \begin{pmatrix} \underline{\boldsymbol{v}}^{\text{f}} \\ \underline{p} \end{pmatrix} = \begin{pmatrix} \boldsymbol{f}_m \\ \boldsymbol{0} \end{pmatrix}, \tag{5.68}$$

where $\underline{\boldsymbol{v}}^{\text{f}}$ and $\underline{p}$ are the unknown vectors for velocity components and pressure respectively at each finite element node, $\boldsymbol{f}_m$ is the right-hand side vector and $\boldsymbol{A}$, $\boldsymbol{B}$ are the block matrices in the left-hand side. Equation (5.68) is the matrix representation of the saddle point problem. To solve the problem, the left-hand side matrix has to be non-singular, or invertible, which can be satisfied mainly by the following methods.

Mixed Finite Element Methods

The polynomial spaces for the velocity and pressure should be compatible with each other based on the requirement of $\text{null}(\boldsymbol{B}) = 0$. A necessary, but not sufficient condition to ensure this criteria is that $\dim \mathscr{V}_q^{\text{h}} \leq \dim \mathscr{V}_{\boldsymbol{\psi}^{\text{f}}}^{\text{h}}$. The sufficient condition is called Ladyzhenskaya-Babŭska-Brezzi (LBB) or inf-sup condition:

Theorem 5.1. *There exists a $\beta > 0$ for the bilinear form $b(\boldsymbol{\psi}_{\text{h}}^{\text{f}}, q_{\text{h}})$ such that*

$$\inf_{q_{\text{h}} \in \mathscr{V}_q^{\text{h}}} \sup_{\boldsymbol{\psi}_{\text{h}}^{\text{f}} \in \mathscr{V}_{\boldsymbol{\psi}^{\text{f}}}^{\text{h}}} \frac{b(\boldsymbol{\psi}_{\text{h}}^{\text{f}}, q_{\text{h}})}{||\boldsymbol{\psi}_{\text{h}}^{\text{f}}||_{\mathscr{V}_{\boldsymbol{\psi}_{\text{h}}^{\text{f}}}} ||q_{\text{h}}||_{\mathscr{V}_p^{\text{h}}}} \geq \beta, \tag{5.69}$$

where β is independent of the mesh size h.

The polynomial spaces for velocity and pressure which satisfy the LBB condition are said to be compatible and LBB stable. For such cases, there exists a unique $\boldsymbol{v}_{\text{h}}^{\text{f}} \in \mathscr{S}_{\boldsymbol{\psi}_{\text{h}}^{\text{f}}}^{\text{h}}$ and $p_{\text{h}} \in \mathscr{S}_q^{\text{h}}$ for the weak form of the equation.

Stabilization Methods

There is a way to circumvent the LBB condition. Till now, we have seen that the only major requirement is for the left-hand side matrix to be non-singular which is not possible due to the zero block matrix. To enforce this positive definiteness property to the global left-hand side matrix, we can modify the weak form of the equation such that we do not get the zero block matrix. These type of methods can be categorized into *Petrov-Galerkin* techniques. In contrast to Galerkin method where we take the weighting function space to be the same as the trial solution space, in the Petrov-Galerkin methods, we perturb the weighting function by certain amount. More details about these methods can be found in [56].

Chapter 6
Quasi-Monolithic Fluid-Structure Formulation

6.1 Introduction

In this chapter, we deal with the first type of strategy in solving the fluid-structure interaction system, namely, monolithic techniques. As mentioned in the previous chapter, one of the advantages of such techniques is the numerical stability of the body-fitted fluid-structure interface, while partitioned techniques suffer from instabilities [39, 66]. Partitioned techniques [147] tend to involve nonlinear iterations per time step for maintaining stability, which increases the computational cost. Thus, monolithic techniques offer an alternative for techniques which can be computationally efficient and stable for low structure-to-fluid mass ratios.

The body-fitted arbitrary Lagrangian-Eulerian (ALE) based methods employing a monolithic approach [90, 88, 179, 78, 3] assemble the fluid and structural equations in a single block matrix and solve them simultaneously at each iteration. This strategy offers numerical stability for problems involving strong added mass effects, however lacks the flexibility and modularity of using the existing stable codes for solving fluid and structural equations.

We present a quasi-monolithic technique for fluid-structure interaction which is inspired by the one-fluid formulation in [217] for studying multiphase problems and the combined fluid-particle formulation [91]. A similar technique called the one-field formulation was considered in [138] for fluid-structure coupling which was only first-order accurate in time. One of the salient features of the formulation is that the kinematic and dynamic continuity conditions along the interface are absorbed in the formulation and are satisfied implicitly, unlike partitioned techniques [147, 64, 63] in which interface conditions have to be enforced explicitly and tractions evaluated along the interface [218]. The ALE mesh equation is decoupled from the rest of the fluid-structure system, thus making the formulation, quasi-monolithic. Such decoupling allows to linearize the Navier-Stokes equations without losing the stability and accuracy leading to solving the coupled system only once per time step, thus reducing the computational cost.

We begin with the variational description of the combined fluid-structure system. We then discuss the quasi-monolithic and the fully stabilized quasi-monolithic formulations for the FSI problems with their implementations and verify them with standard FSI benchmarks available in the literature. Finally, we demonstrate the quasi-monolithic framework for a flapping dynamics problem of a flexible foil.

6.2 Weak Variational Form

In this section, we write the weak variational form of the fluid-structure system in a combined-field form.

6.2.1 Combined Fluid-Structure Formulation

In order to write the weak form of the combined fluid-structure formulation, let us first introduce the trial function spaces $\mathscr{S}_{\boldsymbol{v}}$ and $\mathscr{S}_p$ along with their corresponding test function spaces $\mathscr{V}_{\boldsymbol{\psi}}$ and $\mathscr{V}_q$ for velocity and pressure, respectively. The trial function spaces for the combined field are defined as

$$
\begin{aligned}
\mathscr{S}_{\boldsymbol{v}} = \Big\{ (\boldsymbol{v}^{\mathrm{f}}, \boldsymbol{v}^{\mathrm{s}}) &\in H^1(\Omega^{\mathrm{f}}(t)) \times H^1(\Omega^{\mathrm{s}}) \big| \\
& \boldsymbol{v}^{\mathrm{f}}(\boldsymbol{\varphi}^{\mathrm{s}}(\boldsymbol{X}, t)) = \boldsymbol{v}^{\mathrm{s}}(\boldsymbol{X}, t) \text{ on } \Gamma, \\
& \boldsymbol{v}^{\mathrm{f}}(\boldsymbol{x}, t) = \boldsymbol{v}_D^{\mathrm{f}} \text{ on } \Gamma_D^{\mathrm{f}} \text{ and } \boldsymbol{v}^{\mathrm{s}}(\boldsymbol{X}, t) = \boldsymbol{v}_D^{\mathrm{s}} \text{ on } \Gamma_D^{\mathrm{s}} \Big\}, \\
\mathscr{S}_p = \{ p &\in L^2(\Omega^{\mathrm{f}}(t)) \}.
\end{aligned}
$$

Note that the trial function spaces and the corresponding test function spaces differ only at the Dirichlet boundary. Thus, the test function spaces can be defined as

$$
\begin{aligned}
\mathscr{V}_{\boldsymbol{\psi}} = \Big\{ (\boldsymbol{\psi}^{\mathrm{f}}, \boldsymbol{\psi}^{\mathrm{s}}) &\in H^1(\Omega^{\mathrm{f}}(t)) \times H^1(\Omega^{\mathrm{s}}) \big| \\
& \boldsymbol{\psi}^{\mathrm{f}}(\boldsymbol{\varphi}^{\mathrm{s}}(\boldsymbol{X}, t)) = \boldsymbol{\psi}^{\mathrm{s}}(\boldsymbol{X}) \text{ on } \Gamma, \\
& \boldsymbol{\psi}^{\mathrm{f}}(\boldsymbol{x}) = 0 \text{ on } \Gamma_D^{\mathrm{f}} \text{ and } \boldsymbol{\psi}^{\mathrm{s}}(\boldsymbol{X}) = 0 \text{ on } \Gamma_D^{\mathrm{s}} \Big\}, \\
\mathscr{V}_q = \{ q &\in L^2(\Omega^{\mathrm{f}}(t)) \}.
\end{aligned}
$$

One may observe that the test functions of fluid and structural velocities are defined on different domains $\Omega^{\mathrm{f}}(t)$ and Ω^{s} which satisfy the matching condition along the interface,

$$
\boldsymbol{\psi}^{\mathrm{f}}(\boldsymbol{x}) = \boldsymbol{\psi}^{\mathrm{s}}(\boldsymbol{X}) \quad \forall \boldsymbol{X} \in \Gamma, \tag{6.1}
$$

where $\boldsymbol{x} = \boldsymbol{\varphi}^{\mathrm{s}}(\boldsymbol{X}, t)$ with $\boldsymbol{\varphi}^{\mathrm{s}}$ being the mapping function. The weak form of the Navier-Stokes Eqs. (3.94) and (3.95) in the ALE framework is

$$\int_{\Omega^{\mathrm{f}}(t)} \rho^{\mathrm{f}} \left(\left.\frac{\partial \boldsymbol{v}^{\mathrm{f}}}{\partial t}\right|_{\boldsymbol{\chi}} + (\boldsymbol{v}^{\mathrm{f}} - \boldsymbol{w}) \cdot \nabla \boldsymbol{v}^{\mathrm{f}} \right) \cdot \boldsymbol{\psi}^{\mathrm{f}} d\boldsymbol{x} + \int_{\Omega^{\mathrm{f}}(t)} \boldsymbol{\sigma}^{\mathrm{f}} : \nabla \boldsymbol{\psi}^{\mathrm{f}} d\boldsymbol{x} =$$

$$\int_{\Omega^{\mathrm{f}}(t)} \rho^{\mathrm{f}} \boldsymbol{b}^{\mathrm{f}} \cdot \boldsymbol{\psi}^{\mathrm{f}} d\boldsymbol{x} + \int_{\Gamma_N^{\mathrm{f}}} \boldsymbol{\sigma}_N^{\mathrm{f}} \cdot \boldsymbol{\psi}^{\mathrm{f}} d\Gamma + \int_{\Gamma(t)} \left(\boldsymbol{\sigma}^{\mathrm{f}}(\boldsymbol{x},t) \cdot \boldsymbol{n}^{\mathrm{f}} \right) \cdot \boldsymbol{\psi}^{\mathrm{f}} d\Gamma, \qquad (6.2)$$

$$\int_{\Omega^{\mathrm{f}}(t)} (\nabla \cdot \boldsymbol{v}^{\mathrm{f}}) q d\boldsymbol{x} = 0. \qquad (6.3)$$

The weak forms presented in Eqs. (6.2) and (6.3) are obtained by multiplying Eq. (3.94) with $\boldsymbol{\psi}^{\mathrm{f}}$ and Eq. (3.77) with q using a dot product, then integrating them over the fluid domain $\Omega^{\mathrm{f}}(t)$. Similarly, we can define the weak form of the structural equilibrium Eq. (3.87) as

$$\int_{\Omega^{\mathrm{s}}} \rho^{\mathrm{s}} \frac{\partial \boldsymbol{v}^{\mathrm{s}}}{\partial t} \cdot \boldsymbol{\psi}^{\mathrm{s}} d\boldsymbol{X} + \int_{\Omega^{\mathrm{s}}} \boldsymbol{\sigma}^{\mathrm{s}} : \nabla \boldsymbol{\psi}^{\mathrm{s}} d\boldsymbol{X} =$$

$$\int_{\Omega^{\mathrm{s}}} \rho^{\mathrm{s}} \boldsymbol{b}^{\mathrm{s}} \cdot \boldsymbol{\psi}^{\mathrm{s}} d\boldsymbol{X} + \int_{\Gamma_N^{\mathrm{s}}} \boldsymbol{\sigma}_N^{\mathrm{s}} \cdot \boldsymbol{\psi}^{\mathrm{s}} d\Gamma + \int_{\Gamma} (\boldsymbol{\sigma}^{\mathrm{s}}(\boldsymbol{X},t) \cdot \boldsymbol{n}^{\mathrm{s}}) \cdot \boldsymbol{\psi}^{\mathrm{s}}(\boldsymbol{X}) d\Gamma. \qquad (6.4)$$

Furthermore, the weak form for the traction continuity condition given in Eq. (3.97) will be

$$\int_{\Gamma(t)} \left(\boldsymbol{\sigma}^{\mathrm{f}}(\boldsymbol{x},t) \cdot \boldsymbol{n}^{\mathrm{f}} \right) \cdot \boldsymbol{\psi}^{\mathrm{f}}(\boldsymbol{x}) d\Gamma + \int_{\Gamma} (\boldsymbol{\sigma}^{\mathrm{s}}(\boldsymbol{X},t) \cdot \boldsymbol{n}^{\mathrm{s}}) \cdot \boldsymbol{\psi}^{\mathrm{s}}(\boldsymbol{X}) d\Gamma = 0, \qquad (6.5)$$

where $\boldsymbol{\psi}^{\mathrm{f}}$ and $\boldsymbol{\psi}^{\mathrm{s}}$ are required to satisfy $\boldsymbol{\psi}^{\mathrm{f}}(\boldsymbol{\varphi}^{\mathrm{s}}(\cdot)) = \boldsymbol{\psi}^{\mathrm{s}}(\cdot)$ on Γ. A detailed derivation of the above weak form in Eq. (6.5) from its strong form in Eq. (3.97) can be found in [138]. Now we can combine Eqs. (6.2)-(6.4) using Eqs. (6.5) and (6.1) to construct a single unique relation for the combined fluid-structure domain, which is given as: find $[\boldsymbol{v}^{\mathrm{f}}, \boldsymbol{v}^{\mathrm{s}}, p] \in \mathscr{S}_v \times \mathscr{S}_p$ such that $\forall [\boldsymbol{\psi}^{\mathrm{f}}, \boldsymbol{\psi}^{\mathrm{s}}, q] \in \mathscr{V}_\psi \times \mathscr{V}_q$:

$$\int_{\Omega^{\mathrm{f}}(t)} \rho^{\mathrm{f}} \left(\left.\frac{\partial \boldsymbol{v}^{\mathrm{f}}}{\partial t}\right|_{\boldsymbol{\chi}} + (\boldsymbol{v}^{\mathrm{f}} - \boldsymbol{w}) \cdot \nabla \boldsymbol{v}^{\mathrm{f}} \right) \cdot \boldsymbol{\psi}^{\mathrm{f}}(\boldsymbol{x}) d\boldsymbol{x} + \int_{\Omega^{\mathrm{f}}(t)} \boldsymbol{\sigma}^{\mathrm{f}} : \nabla \boldsymbol{\psi}^{\mathrm{f}} d\boldsymbol{x}$$

$$- \int_{\Omega^{\mathrm{f}}(t)} (\nabla \cdot \boldsymbol{v}^{\mathrm{f}}) q d\boldsymbol{x}$$

$$+ \int_{\Omega^{\mathrm{s}}} \rho^{\mathrm{s}} \frac{\partial \boldsymbol{v}^{\mathrm{s}}}{\partial t} \cdot \boldsymbol{\psi}^{\mathrm{s}} d\boldsymbol{X} + \int_{\Omega^{\mathrm{s}}} \boldsymbol{\sigma}^{\mathrm{s}} : \nabla \boldsymbol{\psi}^{\mathrm{s}} d\boldsymbol{X} =$$

$$\int_{\Omega^{\mathrm{f}}(t)} \rho^{\mathrm{f}} \boldsymbol{b}^{\mathrm{f}} \cdot \boldsymbol{\psi}^{\mathrm{f}} d\boldsymbol{x} + \int_{\Gamma_N^{\mathrm{f}}} \boldsymbol{\sigma}_N^{\mathrm{f}} \cdot \boldsymbol{\psi}^{\mathrm{f}} d\Gamma + \int_{\Omega^{\mathrm{s}}} \rho^{\mathrm{s}} \boldsymbol{b}^{\mathrm{s}} \cdot \boldsymbol{\psi}^{\mathrm{s}} d\boldsymbol{X} + \int_{\Gamma_N^{\mathrm{s}}} \boldsymbol{\sigma}_N^{\mathrm{s}} \cdot \boldsymbol{\psi}^{\mathrm{s}} d\Gamma. \qquad (6.6)$$

As can be observed, the velocity continuity (kinematic condition) at the interface is enforced in the function space and the traction continuity (dynamic equilibrium) is implicitly built in the formulation. Thus, the crucial idea is to solve the fluid and the structural domains as a single unique domain $\Omega = \Omega^{\mathrm{f}} \cup \Omega^{\mathrm{s}}$.

6.2.2 Finite Element Space Discretization

In contrast to many FSI schemes available in the literature [109, 172] which apply a finite-volume discretization for the fluid equations in combination with a finite-element discretization for the structural equations, a spatial discretization with finite elements is applied throughout this formulation. We adopt the Galerkin finite element formulation to discretize the weak formulation in Eq. (6.6). As mentioned in Appendix A5.1, the pressure-velocity coupling can be solved either by satisfying the LBB condition or using stabilization methods. Stabilization methods give an additional advantage of stability in convection-dominated regimes.

Here, we apply both approaches to the quasi-monolithic formulation. Section 6.3 deals with the formulation where we approximate the fluid velocity, pressure and structural velocity using $\mathbb{P}_2/\mathbb{P}_1/\mathbb{P}_2$ isoparametric elements, to satisfy the inf-sup or LBB condition for well-posedness. On the other hand, Section 6.5 discusses the stabilized quasi-monolithic technique. $\mathscr{T}_\mathrm{h}^\mathrm{f}(t)$ and $\mathscr{T}_\mathrm{h}^\mathrm{s}$ represent the triangular mesh on domains $\Omega^\mathrm{f}(t)$ and Ω^s, respectively. To increase the computational efficiency, we assume that the edges of the isoparametric elements are straight unless they represent either the interface or curved boundaries.

6.3 Quasi-Monolithic Formulation

In this section, we will present the second-order time discretization of the combined fluid-structure formulation given Section 6.2.1. The explicit construction of the interface at the start of each time step decouples the fluid-structure interface and ALE mesh from the computation of fluid-structure variables $(v^\mathrm{f}, p, v^\mathrm{s})$. Additionally, the decoupling of the ALE mesh enables us to determine the convective velocity of the fluid flow explicitly and linearize the nonlinear Navier-Stokes equations. Hence, the quasi-monolithic formulation does not require nonlinear iterations per time step.

6.3.1 Second-Order in Time Discretization

Let $\mathbb{P}_2(\Omega_\mathrm{h})$ denote the standard second-order Lagrange finite element space on domain $\Omega_\mathrm{h} = \Omega_\mathrm{h}^\mathrm{f} \cup \Omega_\mathrm{h}^\mathrm{s}$. First, we employ the second-order extrapolation to describe the deformation vector $\varphi_\mathrm{h}^\mathrm{s,n}$ of the structure as

$$\varphi_\mathrm{h}^\mathrm{s,n}(X_i) = \varphi_\mathrm{h}^\mathrm{s,n-1}(X_i) + \frac{3\Delta t}{2} v_\mathrm{h}^\mathrm{s,n-1}(X_i) - \frac{\Delta t}{2} v_\mathrm{h}^\mathrm{s,n-2}(X_i) \qquad \forall X_i \in \mathscr{T}_\mathrm{h}^\mathrm{s}. \quad (6.7)$$

We then use $\varphi_\mathrm{h}^\mathrm{s,n}(X_i)$ to update the ALE mesh displacement vector $u_\mathrm{h}^\mathrm{f,n}$ for the interface nodes through Eq. (3.105). Now that we have both the boundary conditions Eqs. (3.105) and (3.106) required for solving the ALE Eq. (3.104), we

solve Eq. (3.104) employing $\mathbb{P}_1$ finite element space. The assumption made in Section 6.2.2 that all the isoparametric element edges are straight unless they are on the interface or curved boundaries enables us to use $\mathbb{P}_1$ finite element discretization instead of the $\mathbb{P}_2$. As a result of this, the size of the system of linear equations required for solving the ALE mesh displacement vector, $u_h^{f,n}$, for finite element space with $\mathbb{P}_1$ discretization would be smaller than for the $\mathbb{P}_2$ discretization space without losing the accuracy of the coupled fluid-structure solver.

We now use the solution of $u_h^{f,n}$ computed on the $\mathbb{P}_1$ finite element space to update the location of triangular mesh $\mathscr{T}_{h,t^n}^f$ vertices using the Eq. (3.107). Since the interior edges are straight, we can position the non-vertex computational node at the center of the edge. In this way, we are able to determine the ALE mesh displacement for all the $\mathbb{P}_2$ finite element mesh $\mathscr{T}_{h,t^n}^f$ computational nodes even by solving the ALE Eq. (3.104) on a $\mathbb{P}_1$ finite element mesh.

Let us now define $\mathbb{P}_m/\mathbb{P}_{m-1}/\mathbb{P}_m$ solution space $\mathscr{V}_h$ as

$$
\mathscr{V}_h(t^n, \boldsymbol{\varphi}_h^{s,n}, \alpha, \boldsymbol{b}) = \Big\{ (\boldsymbol{v}_h^f, p_h, \boldsymbol{v}_h^s) : \boldsymbol{v}_h^f \in \mathbb{P}_m(\Omega_{h,t^n}^f), p_h \in \mathbb{P}_{m-1}(\Omega_{h,t^n}^f), \boldsymbol{v}_h^s \in \mathbb{P}_m(\Omega_h^s),
$$
$$
\forall \, \boldsymbol{X}_i \in \mathscr{T}_h^{\Gamma}, \, \boldsymbol{v}_h^f(\boldsymbol{\varphi}_h^{s,n}(\boldsymbol{X}_i)) = \alpha \boldsymbol{v}_h^s(\boldsymbol{X}_i) + \boldsymbol{b} \Big\}, \tag{6.8}
$$

where $\mathscr{T}_h^{\Gamma}$ is the mesh on the fluid-structure interface Γ. There are two parameters α and $\boldsymbol{b}$ in the definition of Eq. (6.8). These two parameters enable us to enforce the following condition on the fluid-structure interface. The test function space is chosen to be $\mathscr{V}_h(t^n, \boldsymbol{\varphi}_h^{s,n}, 1, \boldsymbol{0})$. By setting $\alpha = \frac{3}{4}$ and $\boldsymbol{b} = \frac{1}{2} \boldsymbol{v}_h^{s,n-1} - \frac{1}{4} \boldsymbol{v}_h^{s,n-2}$, and then finding $(\boldsymbol{v}_h^{f,n}, p_h, \boldsymbol{v}_h^{s,n}) \in \mathscr{V}_h(t^n, \boldsymbol{\varphi}_h^{s,n}, \alpha, \boldsymbol{b})$ we can enforce the following condition:

$$
\boldsymbol{v}_h^{f,n}(\boldsymbol{\varphi}_h^{s,n}(\boldsymbol{X}_i)) = \frac{3}{4} \boldsymbol{v}_h^{s,n}(\boldsymbol{X}_i) + \frac{1}{2} \boldsymbol{v}_h^{s,n-1}(\boldsymbol{X}_i) - \frac{1}{4} \boldsymbol{v}_h^{s,n-2}(\boldsymbol{X}_i). \tag{6.9}
$$

The above equation is required to be valid for any $\boldsymbol{X}_i$ representing a grid point on $\mathscr{T}_h^{\Gamma}$. Equation (6.9) is required to prove the energy based stability of the quasi-monolithic formulation which has been shown in [139]. Fortunately, the accuracy is also maintained since Eq. (6.9) is a second-order approximation of the interface condition Eq. (3.96).

We now define a second-order time-accurate extrapolation function as

$$
\check{\boldsymbol{v}}_h^f(\boldsymbol{\Psi}_h^n(\boldsymbol{x}, t^n)) = 2\boldsymbol{v}_h^{f,n-1}(\boldsymbol{\Psi}_h^n(\boldsymbol{x}, t^{n-1})) - \boldsymbol{v}_h^{f,n-2}(\boldsymbol{\Psi}_h^n(\boldsymbol{x}, t^{n-2})) \tag{6.10}
$$

where $\boldsymbol{\Psi}_h^n(\cdot, t^{n-j})$ is the backward mapping function for the spatial grid points on the mesh $\mathscr{T}_{h,t^n}^f$ to $\mathscr{T}_{h,t^{n-j}}^f$ and mesh velocity $\boldsymbol{w}_h^n(\boldsymbol{x})$ is defined as

$$
\boldsymbol{w}_h^n(\boldsymbol{x}) = \sum_{i=1}^{G} \psi_i^{f,n}(\boldsymbol{x}) \frac{1}{\Delta t} \left((\boldsymbol{x}_i^n - \boldsymbol{x}_i^{n-1}) + \frac{1}{2} (\boldsymbol{x}_i^{n-1} - \boldsymbol{x}_i^{n-2}) - \frac{1}{2} (\boldsymbol{x}_i^{n-2} - \boldsymbol{x}_i^{n-3}) \right)
$$
$$
= \sum_{i=1}^{G} \psi_i^{f,n}(\boldsymbol{x}) \frac{1}{\Delta t} \left(\boldsymbol{x}_i^n - \frac{1}{2} \boldsymbol{x}_i^{n-1} - \boldsymbol{x}_i^{n-2} + \frac{1}{2} \boldsymbol{x}_i^{n-3} \right), \tag{6.11}
$$

where G is the total number of grid points and $\psi_i^{\mathrm{f,n}}$ denotes the shape function in the fluid domain. Here, $w_{\mathrm{h}}^{\mathrm{n}}$ is a second-order approximation of the fluid mesh velocity $\partial_t \Psi_{\mathrm{h}}^{\mathrm{n}}(x, t^{\mathrm{n}})$ as can be seen from the expression:

$$f'(t^{\mathrm{n}}) = \frac{1}{\Delta t}\left(f(t^{\mathrm{n}}) - \frac{1}{2}f(t^{\mathrm{n-1}}) - f(t^{\mathrm{n-2}}) + \frac{1}{2}f(t^{\mathrm{n-3}})\right) + O(\Delta t^2).$$

We next show that

$$w_{\mathrm{h}}^{\mathrm{n}}(x_j^{\mathrm{n}}) = \check{v}_{\mathrm{h}}^{\mathrm{f}}(x_j^{\mathrm{n}}) \qquad \text{on} \quad \Gamma_{\mathrm{h},t^{\mathrm{n}}}. \tag{6.12}$$

To prove the above equation, we rewrite Eq. (6.11) as

$$\begin{aligned} w_{\mathrm{h}}^{\mathrm{n}}(x_j^{\mathrm{n}}) =& \frac{1}{\Delta t}\left((x_j^{\mathrm{n}} - x_j^{\mathrm{n-1}}) + \frac{1}{2}\left(x_j^{\mathrm{n-1}} - x_j^{\mathrm{n-2}}\right) - \frac{1}{2}\left(x_j^{\mathrm{n-2}} - x_j^{\mathrm{n-3}}\right)\right) \\ =& \frac{\varphi_{\mathrm{h}}^{\mathrm{s,n}}(X_j) - \varphi_{\mathrm{h}}^{\mathrm{s,n-1}}(X_j)}{\Delta t} + \frac{\varphi_{\mathrm{h}}^{\mathrm{s,n-1}}(X_j) - \varphi_{\mathrm{h}}^{\mathrm{s,n-2}}(X_j)}{2\Delta t} \\ & - \frac{\varphi_{\mathrm{h}}^{\mathrm{s,n-2}}(X_j) - \varphi_{\mathrm{h}}^{\mathrm{s,n-3}}(X_j)}{2\Delta t} \ \forall \ X_j \in \Gamma_{\mathrm{h},t^{\mathrm{n}}}. \end{aligned} \tag{6.13}$$

By substituting the definition of $\varphi^{\mathrm{s,n}}(X)$ from Eq. (6.7) into the above Eq. (6.13) and simplifying, we get

$$\begin{aligned} w_{\mathrm{h}}^{\mathrm{n}}(x_j^{\mathrm{n}}) =& 2\left(\frac{3}{4}v_{\mathrm{h}}^{\mathrm{s,n-1}}(X_j) + \frac{1}{2}v_{\mathrm{h}}^{\mathrm{s,n-2}}(X_j) - \frac{1}{4}v_{\mathrm{h}}^{\mathrm{s,n-3}}(X_j)\right) \\ & - \left(\frac{3}{4}v_{\mathrm{h}}^{\mathrm{s,n-2}}(X_j) + \frac{1}{2}v_{\mathrm{h}}^{\mathrm{s,n-3}}(X_j) - \frac{1}{4}v_{\mathrm{h}}^{\mathrm{s,n-4}}(X_j)\right). \end{aligned}$$

With the aid of Eq. (6.9), we can finally obtain $w_{\mathrm{h}}^{\mathrm{n}}(x_j^{\mathrm{n}}) = \check{v}_{\mathrm{h}}^{\mathrm{f}}(x_j^{\mathrm{n}})$ from the above equation. A detailed energy based proof on the stability of the quasi-monolithic formulation can be found in [139]. We next proceed to write the complete fluid-structure formulation.

6.3.2 Complete Scheme

In this subsection, we present the fully discretized finite element form of the quasi-monolithic formulation. The variational statement reads as:

$$\text{find} \quad (v_{\mathrm{h}}^{\mathrm{f,n}}, p_{\mathrm{h}}^{\mathrm{f,n}}, v_{\mathrm{h}}^{\mathrm{s,n}}) \in \mathscr{V}_{\mathrm{h}}\left(t^{\mathrm{n}}, \varphi_{\mathrm{h}}^{\mathrm{s,n}}, \frac{3}{4}, \frac{1}{2}v_{\mathrm{h}}^{\mathrm{s,n-1}} - \frac{1}{4}v_{\mathrm{h}}^{\mathrm{s,n-2}}\right)$$

with $v_{\mathrm{h}}^{\mathrm{f,n}}|_{\Gamma_D^{\mathrm{f}}} = v_D^{\mathrm{f}}$ and $v_{\mathrm{h}}^{\mathrm{s,n}}|_{\Gamma_D^{\mathrm{s}}} = v_D^{\mathrm{s}}$ so that for any finite element triple

$$(\psi^{\mathrm{f}}, q^{\mathrm{f}}, \psi^{\mathrm{s}}) \in \mathscr{V}_{\mathrm{h}}(t^{\mathrm{n}}, \varphi_{\mathrm{h}}^{\mathrm{s,n}}, 1, \mathbf{0}) \tag{6.14}$$

with $\psi_h^f|_{\Gamma_D^f} = 0$ and $\psi_h^s|_{\Gamma_D^s} = 0$, such that

$$
\begin{aligned}
\int_{\Omega_h^f(t^n)} &\left[\frac{\rho^f}{\Delta t} \left(\frac{3}{2} v_h^{f,n}(\boldsymbol{x}) - 2v_h^{f,n-1}(\boldsymbol{\Psi}_h^n(\boldsymbol{x},t^{n-1})) + \frac{1}{2} v_h^{f,n-2}(\boldsymbol{\Psi}_h^n(\boldsymbol{x},t^{n-2})) \right) \right. \\
&\left. + \left(\check{v}_h^f - \boldsymbol{w}_h^n \right) \cdot \nabla v_h^{f,n} + \frac{1}{2} \left(\nabla \check{v}_h^f \right) v_h^{f,n} \right] \cdot \psi^f d\boldsymbol{x} \\
&+ \int_{\Omega_h^f(t^n)} \mu^f \left(\nabla v_h^{f,n} + (\nabla v_h^{f,n})^T \right) : \nabla \psi^f d\boldsymbol{x} \bigg\} \, A \\
&- \int_{\Omega_h^f(t^n)} p_h^{f,n} (\nabla \cdot \psi^f) d\boldsymbol{x} \bigg\} \, B \\
&- \int_{\Omega_h^f(t^n)} q^f (\nabla \cdot v_h^{f,n}) d\boldsymbol{x} \bigg\} \, C \\
&+ \int_{\Omega_h^s} \frac{\rho^s}{\Delta t} \left(\frac{3}{2} v_h^{s,n} - 2v_h^{s,n-1} + \frac{1}{2} v_h^{s,n-2} \right) \cdot \psi^s d\boldsymbol{X} \\
&+ \frac{1}{2} \int_{\Omega_h^s} \left(\boldsymbol{\sigma}^s(\varphi_h^{s,n-1}) + \boldsymbol{\sigma}^s(\varphi_h^{s,n+1}) \right) : \nabla \psi^s d\boldsymbol{X} \bigg\} \, D \\
= \int_{\Omega_h^f(t^n)} &\rho^f \boldsymbol{b}^f \cdot \psi^f d\boldsymbol{x} + \int_{(\Gamma_H^f)_h} \boldsymbol{\sigma}_N^f \cdot \psi^f d\Gamma + \int_{\Omega_h^s} \rho^s \boldsymbol{b}^s \cdot \psi^s d\boldsymbol{X} + \int_{(\Gamma_N^s)_h} \boldsymbol{\sigma}_N^s \cdot \psi^f d\Gamma, \bigg\} \, E
\end{aligned}
$$

$$(6.15)$$

where A contains the transient, convective and diffusive contributions, B and C are the pressure and continuity terms respectively, D represents the momentum equation for the structure and E consists of the external body force and boundary conditions. The technique of adding the term $\frac{1}{2} \left(\nabla \check{v}_h^f \right) v_h^{f,n}$ in part A of Eq. (6.15) is to stabilize the convective term, which is discussed in detail in [207].

For linearly elastic materials, we can represent $\boldsymbol{\sigma}^s(\varphi^{s,n+1})$ from the part D in Eq. (6.15) using Eq. (6.7) as

$$
\boldsymbol{\sigma}^s(\varphi^{s,n+1}) = \boldsymbol{\sigma}^s \left(\varphi^{s,n} + \frac{\Delta t}{2} \left(3v^{s,n} - v^{s,n-1} \right) \right). \tag{6.16}
$$

Similarly for nonlinear material, we can approximate the last term of part D from Eq. (6.15) as

$$
\int_{\Omega_h^s} \boldsymbol{\sigma}^s(\varphi_h^{s,n+1}) : \nabla \psi^s d\boldsymbol{X} \tag{6.17}
$$

by the sum of a known forcing term and a linear term for the unknown $v_h^{s,n}$,

$$
\int_{\Omega_h^s} \boldsymbol{\sigma}^s \left(\varphi_h^{s,n} - \frac{\Delta t}{2} v_h^{s,n-1} \right) : \nabla \psi^s d\boldsymbol{X} + \frac{3\Delta t}{2} A_s \left(\nabla \left(\varphi_h^{s,n} - \frac{\Delta t}{2} v_h^{s,n-1} \right); \nabla v_h^{s,n}, \nabla \psi^s \right). \tag{6.18}
$$

We have ignored a remainder term of size $O(\Delta t^2)$ in the above linearization. For a St. Venant-Kirchhoff material (see for example [138, 10]), the quantity A_s can be written as

$$
A_s(\boldsymbol{F}; \boldsymbol{g}, \boldsymbol{H}) = \int_{\Omega^s} \left(\lambda^s (\mathrm{tr}\boldsymbol{E}) \boldsymbol{H} : \boldsymbol{g} + \frac{\lambda^s}{4} \mathrm{tr}(\boldsymbol{H}^T \boldsymbol{F} + \boldsymbol{F}^T \boldsymbol{H}) \mathrm{tr}(\boldsymbol{g}^T \boldsymbol{F} + \boldsymbol{F}^T \boldsymbol{g}) \right.
$$

$$
\left. + \mu^s \boldsymbol{E} : (\boldsymbol{H}^T \boldsymbol{g} + \boldsymbol{g}^T \boldsymbol{H}) + \frac{\mu^s}{2} (\boldsymbol{H}^T \boldsymbol{F} + \boldsymbol{F}^T \boldsymbol{H}) : (\boldsymbol{g}^T \boldsymbol{F} + \boldsymbol{F}^T \boldsymbol{g}) \right), \qquad (6.19)
$$

where $\boldsymbol{E} = \frac{1}{2} \left(\boldsymbol{F}\boldsymbol{F}^T - \boldsymbol{I} \right)$ and $\boldsymbol{H} : \boldsymbol{g} = \mathrm{tr}(\boldsymbol{H}^T \boldsymbol{g})$. $A_s(\boldsymbol{F}; \boldsymbol{g}, \boldsymbol{H})$ is a bilinear functional of $\boldsymbol{g}$ and $\boldsymbol{H}$. Therefore, $\boldsymbol{g}$ and $\boldsymbol{H}$ for Eq. (6.18) will be $\nabla \boldsymbol{v}_h^{s,n}$ and $\nabla \psi^s$, respectively.

6.3.3 Algorithm

The presented variational formulation discussed above is expressed in the algorithmic format in this section. Suppose a mesh $\mathscr{T}_h^s$ for the structural reference domain Ω^s shares a part of its boundary grid points with $\mathscr{T}_\Gamma^h$ along Γ. Assume that $\boldsymbol{v}_h^{f,n-1}, \boldsymbol{v}_h^{s,n-1}$, and $\boldsymbol{\varphi}_h^{s,n-1}$ are known for the mesh $\mathscr{T}_{h,t^{n-1}}^f$ which is defined on the domain $\Omega_h^f(t^{n-1})$. Here, $\Omega_h^f(t^{n-1})$ denotes the numerical approximation for the fluid domain at time t^{n-1}. It should be noted that we have considered $\mathbb{P}_m / \mathbb{P}_{m-1} / \mathbb{P}_m$ elements. To ensure the optimal rate of approximation on an isoparametric finite element mesh, all the constituent elements are considered as straight-edged standard Lagrangian elements. The basic steps to be performed in the quasi-monolithic combined fluid-structure formulation are summarized below:

Algorithm 1 Second-order quasi-monolithic formulation for fluid-structure interactions

---

1. Start from known solutions of the field variables $\boldsymbol{v}_h^{f,n-1}, \boldsymbol{v}_h^{f,n-2}, \boldsymbol{v}_h^{s,n-1}, \boldsymbol{v}_h^{s,n-2}, \boldsymbol{\varphi}_h^{s,n-1}$ at time t^{n-1}
2. Advance from t^{n-1} to t^n
   (a) Define the structural position $\boldsymbol{\varphi}_h^{s,n}$ using Eq. (6.7)
   (b) Determine positions of vertices of triangles on the fluid domain $\Omega_h^f(t^n)$
       by solving Eq. (3.104) using $\mathbb{P}_1$ elements on $\Omega_h^f(0)$
   (c) Use result from (b) to determine the updated mesh of $\Omega_h^f(t^n)$
   (d) Evaluate $\check{\boldsymbol{v}}_h^f$ and $\boldsymbol{w}_h^n$ by Eqs. (6.10) and (6.11)
   (e) Solve for the updated field properties $\boldsymbol{v}_h^{f,n}, p_h^n$, and $\boldsymbol{v}_h^{s,n}$ at current time t^n using Eq. (6.15)

At each time step, the scheme is solved only once and no nonlinear iterations are necessary for this mathematically nonlinear problem.

6.4 Extension to Multiple Flexible-Bodies

One the key features of the quasi-monolithic with explicit interface updating formulation given in Section 6.3 is that it can be easily extended for FSI problems involving multiple flexible structures. For the case of multiple flexible bodies, let us consider that the solid domain Ω^s is defined as $\Omega^s = \Omega_1^s \cup \Omega_2^s \cdots \Omega_j^s$, where j is the number of flexible bodies interacting with the fluid Ω^f. Each of these flexible structures should satisfy the dynamic equilibrium Eq. (3.79) i.e.

$$\rho_j^s \frac{\partial^2 \varphi_j^s}{\partial t^2} = \nabla \cdot \sigma_j^s + \rho_j^s b_j^s, \qquad \text{on} \quad \Omega_j^s, \tag{6.20}$$

The interface traction and velocity continuity conditions in Eqs. (3.96-3.97) will remain the same since $\Gamma = \Gamma_1 \cup \Gamma_2 \cup \cdots \Gamma_j$, where Γ_j is the interface between Ω^f and Ω_j^s. We can write down the weak-form of the dynamic equilibrium Eq. (6.20) in the similar manner to Eq. (6.4) as

$$\int_{\Omega_j^s} \rho_j^s \frac{\partial v_j^s}{\partial t} \cdot \psi^s dX + \int_{\Omega_j^s} \sigma_j^s : \nabla \psi^s dX =$$

$$\int_{\Omega_j^s} \rho_j^s b_j^s \cdot \psi^s dX + \int_{\Gamma_{N,j}^s} \sigma_{N,j}^s \cdot \psi^s d\Gamma + \int_{\Gamma_j} \left(\sigma_j^s(X,t) \cdot n^s \right) \cdot \psi^s(X) d\Gamma, \tag{6.21}$$

where $\Gamma_{N,j}^s$ represents the Neumann boundary of Ω_j^s and $\sigma_{N,j}^s$ is the traction function along $\Gamma_{N,j}^s$. The subscript j in ρ^s, v^s, σ^s and b^s represent the structural density, velocity, first Piola-Kirchhoff stress tensor and the body force acting on the jth flexible structure. Now, we can merge Eqs. (6.2, 6.21, 3.96-3.97) to construct the weak-form of the combined fluid-structure formulation for multiple flexible structures. The resulting weak-form is

$$\int_{\Omega^f(t)} \rho^f \left(\partial_t v^f(x,t) + (v^f - w) \cdot \nabla v^f \right) \cdot \psi^f(x) dx + \int_{\Omega^f(t)} \sigma^f : \nabla \psi^f dx$$

$$- \int_{\Omega^f(t)} (\nabla \cdot v^f) q dx$$

$$+ \sum_j \int_{\Omega_j^s} \rho_j^s \partial_t v_j^s \cdot \psi^s dX + \sum_j \int_{\Omega_j^s} \sigma_j^s : \nabla \psi^s dX =$$

$$\int_{\Omega^f(t)} \rho^f b^f \cdot \psi^f dx + \int_{\Gamma_N^f} \sigma_N^f \cdot \psi^f d\Gamma + \sum_j \int_{\Omega_j^s} \rho_j^s b_j^s \cdot \psi^s dX + \sum_j \int_{\Gamma_{N,j}^s} \sigma_{N,j}^s \cdot \psi^s d\Gamma.$$

$$\tag{6.22}$$

Let us consider that $\mathscr{T}_{h,j}^s$ represents the finite element discretization of the flexible structure Ω_j^s. The explicit extrapolation of the structural deformation vector for each Lagrangian node (X_j) on structural meshes $\mathscr{T}_{h,i}^s$ will be

$$\boldsymbol{\varphi}_{\mathrm{h},j}^{\mathrm{s,n}}(\boldsymbol{X}_i) = \boldsymbol{\varphi}_{\mathrm{h},j}^{\mathrm{s,n-1}}(\boldsymbol{X}_i) + \frac{3\Delta t}{2}\boldsymbol{v}_{\mathrm{h},j}^{\mathrm{s,n-1}}(\boldsymbol{X}_i) - \frac{\Delta t}{2}\boldsymbol{v}_{\mathrm{h},j}^{\mathrm{s,n-2}}(\boldsymbol{X}_i) \qquad \forall \boldsymbol{X}_i \in \mathscr{T}_{\mathrm{h},j}^{\mathrm{s}},$$

(6.23)

where $\boldsymbol{\varphi}_{\mathrm{h},j}^{\mathrm{s,n}}$ is the jth flexible structure's deformation vector at time step t^{n}. The fully discretized quasi-monolithic combined fluid-structure formulation for multiple flexible bodies using BDF2 is given as

$$\int_{\Omega_{\mathrm{h}}^{\mathrm{f}}(t^{\mathrm{n}})} \left[\frac{\rho^{\mathrm{f}}}{\Delta t} \left(\frac{3}{2}\boldsymbol{v}_{\mathrm{h}}^{\mathrm{f,n}}(\boldsymbol{x}) - 2\boldsymbol{v}_{\mathrm{h}}^{\mathrm{f,n-1}}(\boldsymbol{\Psi}_{\mathrm{h}}^{\mathrm{n}}(\boldsymbol{x},t^{\mathrm{n-1}})) + \frac{1}{2}\boldsymbol{v}_{\mathrm{h}}^{\mathrm{f,n-2}}(\boldsymbol{\Psi}_{\mathrm{h}}^{\mathrm{n}}(\boldsymbol{x},t^{\mathrm{n-2}})) \right) \right.$$
$$\left. + \left(\check{\boldsymbol{v}}_{\mathrm{h}}^{\mathrm{f}} - \boldsymbol{w}_{\mathrm{h}}^{\mathrm{n}} \right) \cdot \nabla \boldsymbol{v}_{\mathrm{h}}^{\mathrm{f,n}} + \frac{1}{2} \left(\nabla \check{\boldsymbol{v}}_{\mathrm{h}}^{\mathrm{f}} \right) \boldsymbol{v}_{\mathrm{h}}^{\mathrm{f,n}} \right] \cdot \boldsymbol{\psi}^{\mathrm{f}} d\boldsymbol{x}$$
$$+ \int_{\Omega_{\mathrm{h}}^{\mathrm{f}}(t^{\mathrm{n}})} \mu^{\mathrm{f}} \left(\nabla \boldsymbol{v}_{\mathrm{h}}^{\mathrm{f,n}} + (\nabla \boldsymbol{v}_{\mathrm{h}}^{\mathrm{f,n}})^T \right) : \nabla \boldsymbol{\psi}^{\mathrm{f}} d\boldsymbol{x} - \int_{\Omega_{\mathrm{h}}^{\mathrm{f}}(t^{\mathrm{n}})} p_{\mathrm{h}}^{\mathrm{f,n}}(\nabla \cdot \boldsymbol{\psi}^{\mathrm{f}}) d\boldsymbol{x}$$
$$- \int_{\Omega_{\mathrm{h}}^{\mathrm{f}}(t^{\mathrm{n}})} q^{\mathrm{f}}(\nabla \cdot \boldsymbol{v}_{\mathrm{h}}^{\mathrm{f,n}}) d\boldsymbol{x}$$
$$+ \sum_j \int_{\Omega_{\mathrm{h},j}^{\mathrm{s}}} \frac{\rho_j^{\mathrm{s}}}{\Delta t} \left(\frac{3}{2}\boldsymbol{v}_{\mathrm{h},j}^{\mathrm{s,n}} - 2\boldsymbol{v}_{\mathrm{h},j}^{\mathrm{s,n-1}} + \frac{1}{2}\boldsymbol{v}_{\mathrm{h},j}^{\mathrm{s,n-2}} \right) \cdot \boldsymbol{\psi}^{\mathrm{s}} d\boldsymbol{X}$$
$$+ \sum_j \frac{1}{2} \int_{\Omega_{\mathrm{h},j}^{\mathrm{s}}} \left(\boldsymbol{\sigma}^{\mathrm{s}}(\boldsymbol{\varphi}_{\mathrm{h},j}^{\mathrm{s,n-1}}) + \boldsymbol{\sigma}^{\mathrm{s}}(\boldsymbol{\varphi}_{\mathrm{h},j}^{\mathrm{s,n+1}}) \right) : \nabla \boldsymbol{\psi}^{\mathrm{s}} d\boldsymbol{X}$$
$$= \int_{\Omega_{\mathrm{h}}^{\mathrm{f}}(t^{\mathrm{n}})} \rho^{\mathrm{f}}\boldsymbol{b}^{\mathrm{f}} \cdot \boldsymbol{\psi}^{\mathrm{f}} d\boldsymbol{x} + \int_{(\Gamma_N^{\mathrm{f}})_{\mathrm{h}}} \boldsymbol{\sigma}_N^{\mathrm{f}} \cdot \boldsymbol{\psi}^{\mathrm{f}} d\Gamma$$
$$+ \sum_j \int_{\Omega_{\mathrm{h},j}^{\mathrm{s}}} \rho_j^{\mathrm{s}}\boldsymbol{b}_j^{\mathrm{s}} \cdot \boldsymbol{\psi}^{\mathrm{s}} d\boldsymbol{X} + \sum_j \int_{(\Gamma_{N,j}^{\mathrm{s}})_{\mathrm{h}}} \boldsymbol{\sigma}_{N,j}^{\mathrm{s}} \cdot \boldsymbol{\psi}^{\mathrm{s}} d\Gamma.$$

(6.24)

The algorithm of the quasi-monolithic combined fluid-structure formulation for multiple flexible structures is identical to the one presented for single flexible structure presented in Section 6.3.3. The only difference is that multiple solid meshes $\mathscr{T}_{\mathrm{h},i}^{\mathrm{s}}$ corresponding to each flexible structure are considered.

6.5 Fully Stabilized Quasi-Monolithic Formulation

One of the limitations of the Galerkin finite element discretization used for discretizing $\Omega^{\mathrm{f}}(t)$ and Ω^{s} of the quasi-monolithic formulation presented in Section 6.3 is the presence of non-physical spurious oscillations for convection-dominant problems [56]. As discussed in Chapter 4, these oscillations are circumvented by replacing the traditional Galerkin method with Petrov-Galerkin stabilization methods which utilize weighting functions that have more weightage for the upstream section of the flow [34, 92]. Such streamwise upwind techniques can be interpreted as combina-

tion of traditional Galerkin method and a stabilization term calculated at the interior of an element. This elemental level stabilization term introduces artificial numerical diffusion which stabilizes the spurious oscillations. The weak-form of the combined fluid-structure formulation given in Eq. (6.6) can be written in the Galerkin/Least square (GLS) stabilization form as

$$
\left.\begin{aligned}
\int_{\Omega_{\mathrm{h}}^{\mathrm{f}}(t)} \rho^{\mathrm{f}} \left(\partial_t v^{\mathrm{f}} + (v^{\mathrm{f}} - w) \cdot \nabla v^{\mathrm{f}} \right) \cdot \psi^{\mathrm{f}} d\Omega + \int_{\Omega^{\mathrm{f}}(t)} \sigma^{\mathrm{f}} : \nabla \psi^{\mathrm{f}} d\Omega \\
- \int_{\Omega^{\mathrm{f}}(t)} (\nabla \cdot v^{\mathrm{f}}) q \, d\Omega
\end{aligned}\right\} A
$$

$$
\left.\begin{aligned}
+ \sum_{e=1}^{n_{\mathrm{el}}} \int_{\Omega^{\mathrm{e}}} \tau_m \left[\rho^{\mathrm{f}} (v^{\mathrm{f}} - w) \cdot \nabla \psi^{\mathrm{f}} + \nabla q \right] \cdot \\
\left[\rho^{\mathrm{f}} \partial_t v^{\mathrm{f}} + \rho^{\mathrm{f}} (v^{\mathrm{f}} - w) \cdot \nabla v^{\mathrm{f}} - \nabla \cdot \sigma^{\mathrm{f}} - \rho^{\mathrm{f}} b^{\mathrm{f}} \right] d\Omega^{\mathrm{e}}
\end{aligned}\right\} B
$$

$$
\left. + \sum_{e=1}^{n_{\mathrm{el}}} \int_{\Omega^{\mathrm{e}}} \nabla \cdot \psi^{\mathrm{f}} \tau_c \nabla \cdot v^{\mathrm{f}} d\Omega^{\mathrm{e}} \right\} D
$$

$$
\left. + \int_{\Omega^{\mathrm{s}}} \rho^{\mathrm{s}} \partial_t v^{\mathrm{s}} \cdot \psi^{\mathrm{s}} d\Omega + \int_{\Omega^{\mathrm{s}}} \sigma^{\mathrm{s}} : \nabla \psi^{\mathrm{s}} d\Omega = \right\} E
$$

$$
\left. \int_{\Omega_{\mathrm{h}}^{\mathrm{f}}(t)} \rho^{\mathrm{f}} b^{\mathrm{f}} \cdot \psi^{\mathrm{f}} d\Omega + \int_{(\Gamma_N^{\mathrm{f}})_{\mathrm{h}}} \sigma_N^{\mathrm{f}} \cdot \psi^{\mathrm{f}} d\Gamma + \int_{\Omega_{\mathrm{h}}^{\mathrm{s}}} \rho^{\mathrm{s}} b^{\mathrm{s}} \cdot \psi^{\mathrm{s}} d\Omega + \int_{(\Gamma_N^{\mathrm{s}})_{\mathrm{h}}} \sigma_N^{\mathrm{s}} \cdot \psi^{\mathrm{s}} d\Gamma. \right\} F
$$

$$(6.25)$$

One can observe that terms A, E and F combine to form the Galerkin weak-form in Eq. (6.6). The terms B and C represent the local element level GLS stabilization terms where B is the convective stabilization to damp the spurious oscillations and C is the pressure stabilization to circumvent the inf-sup condition. Unlike the finite element mesh discretization in Section 6.2.2 where fluid velocity, pressure and structural velocity were approximated using $\mathbb{P}_2/\mathbb{P}_1/\mathbb{P}_2$ isoparametric elements to justify the inf-sup condition or LBB condition for well-posedness, the above stabilized combined fluid-structure weak-form in Eq. (6.25) is approximated using six-node wedge or eight-node hex element with equal order for both fluid velocity and pressure. Equal order approximation for fluid velocity and pressure simplifies the computational framework significantly. The stabilizing parameters τ_m and τ_c in the terms B and C respectively are the least squares metrics [34, 193, 97, 67]. The convective stabilization parameter τ_m is defined as [3]

$$
\tau_m = \left[\left(\frac{2\rho^{\mathrm{f}}}{\Delta t} \right)^2 + \left(\rho^{\mathrm{f}} \right)^2 \left(v^{\mathrm{f}} - w \right) \cdot G \cdot \left(v^{\mathrm{f}} - w \right) + 12(\mu^{\mathrm{f}})^2 G : G \right]^{-\frac{1}{2}}, \quad (6.26)
$$

where G is the elemental contravariant metric tensor which is defined as

$$
G = \left(\frac{\partial \xi}{\partial x} \right)^T \frac{\partial \xi}{\partial x}, \quad (6.27)
$$

where $\boldsymbol{\xi}$ is local element level coordinate system and it depends on the element shape. The least squares metric τ_c for the continuity equation is defined as

$$\tau_c = \frac{1}{8 \operatorname{tr}(\boldsymbol{G}) \tau_m}. \tag{6.28}$$

The stabilization in the variational form provides stability to the velocity field in convection dominated regimes of the fluid domain and circumvents the Babuska-Brezzi condition which is required to be satisfied by any standard mixed Galerkin method. The element metric tensor $\boldsymbol{G}$ deals with different element topology for different mesh discretizations and has been greatly studied in the literature.

The fully discretized quasi-monolithic stabilized fluid-structure formulation for multiple structures using BDF2 can be written as

$$\int_{\Omega_{\mathrm{h}}^{\mathrm{f}}(t^{\mathrm{n}})} \left[\frac{\rho^{\mathrm{f}}}{\Delta t} \left(\frac{3}{2} v_{\mathrm{h}}^{\mathrm{f,n}}(\boldsymbol{x}) - 2 v_{\mathrm{h}}^{\mathrm{f,n-1}}(\boldsymbol{\Psi}_{\mathrm{h}}^{\mathrm{n}}(\boldsymbol{x}, t^{\mathrm{n-1}})) + \frac{1}{2} v_{\mathrm{h}}^{\mathrm{f,n-2}}(\boldsymbol{\Psi}_{\mathrm{h}}^{\mathrm{n}}(\boldsymbol{x}, t^{\mathrm{n-2}})) \right) \right.$$
$$\left. + \left(\check{\boldsymbol{v}}_{\mathrm{h}}^{\mathrm{f}} - \boldsymbol{w}_{\mathrm{h}}^{\mathrm{n}} \right) \cdot \nabla v_{\mathrm{h}}^{\mathrm{f,n}} + \frac{1}{2} \left(\nabla \check{\boldsymbol{v}}_{\mathrm{h}}^{\mathrm{f}} \right) v_{\mathrm{h}}^{\mathrm{f,n}} \right] \cdot \psi^{\mathrm{f}} d\boldsymbol{x}$$
$$+ \int_{\Omega_{\mathrm{h}}^{\mathrm{f}}(t^{\mathrm{n}})} \mu^{\mathrm{f}} \left(\nabla v_{\mathrm{h}}^{\mathrm{f,n}} + (\nabla v_{\mathrm{h}}^{\mathrm{f,n}})^T \right) : \nabla \psi^{\mathrm{f}} d\boldsymbol{x} - \int_{\Omega_{\mathrm{h}}^{\mathrm{f}}(t^{\mathrm{n}})} p_{\mathrm{h}}^{\mathrm{f,n}} (\nabla \cdot \psi^{\mathrm{f}}) d\boldsymbol{x}$$
$$- \int_{\Omega_{\mathrm{h}}^{\mathrm{f}}(t^{\mathrm{n}})} q^{\mathrm{f}} (\nabla \cdot v_{\mathrm{h}}^{\mathrm{f,n}}) d\boldsymbol{x}$$
$$+ \sum_{e=1}^{n_{\mathrm{el}}} \int_{\Omega_{\mathrm{h}}^{\mathrm{e}}} \tau_m \left[\rho^{\mathrm{f}} \left(\check{\boldsymbol{v}}_{\mathrm{h}}^{\mathrm{f}} - \boldsymbol{w}_{\mathrm{h}}^{\mathrm{n}} \right) \cdot \nabla \psi^{\mathrm{f}} + \nabla q \right] \cdot$$
$$\left[\frac{\rho^{\mathrm{f}}}{\Delta t} \left(1.5 v_{\mathrm{h}}^{\mathrm{f,n}} - 2 v_{\mathrm{h}}^{\mathrm{f,n-1}} + 0.5 v_{\mathrm{h}}^{\mathrm{f,n-2}} \right) + \rho^{\mathrm{f}} \left(\check{\boldsymbol{v}}_{\mathrm{h}}^{\mathrm{f}} - \boldsymbol{w}_{\mathrm{h}}^{\mathrm{n}} \right) \cdot \nabla v_{\mathrm{h}}^{\mathrm{f,n}} - \nabla \cdot \sigma_{\mathrm{h}}^{\mathrm{f,n}} - \rho^{\mathrm{f}} \boldsymbol{b}^{\mathrm{f}} \right] d\Omega^{\mathrm{e}}$$
$$+ \sum_{e=1}^{n_{\mathrm{el}}} \int_{\Omega_{\mathrm{h}}^{\mathrm{e}}} \nabla \cdot \psi^{\mathrm{f}} \tau_c \nabla \cdot v_{\mathrm{h}}^{\mathrm{f,n}} d\Omega^{\mathrm{e}}$$
$$+ \sum_j \int_{\Omega_{\mathrm{h},j}^{\mathrm{s}}} \frac{\rho_j^{\mathrm{s}}}{\Delta t} \left(\frac{3}{2} v_{\mathrm{h},j}^{\mathrm{s,n}} - 2 v_{\mathrm{h},j}^{\mathrm{s,n-1}} + \frac{1}{2} v_{\mathrm{h},j}^{\mathrm{s,n-2}} \right) \cdot \psi^{\mathrm{s}} d\boldsymbol{X}$$
$$+ \sum_j \frac{1}{2} \int_{\Omega_{\mathrm{h},j}^{\mathrm{s}}} \left(\sigma^{\mathrm{s}}(\varphi_{\mathrm{h},j}^{\mathrm{s,n-1}}) + \sigma^{\mathrm{s}}(\varphi_{\mathrm{h},j}^{\mathrm{s,n+1}}) \right) : \nabla \psi^{\mathrm{s}} d\boldsymbol{X}$$
$$= \int_{\Omega_{\mathrm{h},t^{\mathrm{n}}}^{\mathrm{f}}} \rho^{\mathrm{f}} \boldsymbol{b}^{\mathrm{f}} \cdot \psi^{\mathrm{f}} d\boldsymbol{x} + \int_{(\Gamma_N^{\mathrm{f}})_{\mathrm{h}}} \sigma_N^{\mathrm{f}} \cdot \psi^{\mathrm{f}} d\Gamma$$
$$+ \sum_j \int_{\Omega_{\mathrm{h},j}^{\mathrm{s}}} \rho_j^{\mathrm{s}} \boldsymbol{b}_j^{\mathrm{s}} \cdot \psi^{\mathrm{s}} d\boldsymbol{X} + \sum_j \int_{(\Gamma_{N,j}^{\mathrm{s}})_{\mathrm{h}}} \sigma_{N,j}^{\mathrm{s}} \cdot \psi^{\mathrm{s}} d\Gamma. \tag{6.29}$$

The implementation of the above fully stabilized quasi-monolithic combined fluid-structure formulation differs slightly from the implementation in Section 6.3. Instead of Eq. (6.10) we define an alternative second-order time accurate explicit

function given by

$$\check{v}_{\mathrm{h}}^{\mathrm{f}}(\boldsymbol{\Psi}_{\mathrm{h}}^{\mathrm{n}}(\boldsymbol{x},t^{\mathrm{n}})) = 2.25 v_{\mathrm{h}}^{\mathrm{f,n-1}}(\boldsymbol{\Psi}_{\mathrm{h}}^{\mathrm{n}}(\boldsymbol{x},t^{\mathrm{n-1}})) - 1.5 v_{\mathrm{h}}^{\mathrm{f,n-2}}(\boldsymbol{\Psi}_{\mathrm{h}}^{\mathrm{n}}(\boldsymbol{x},t^{\mathrm{n-2}}))$$
$$+ 0.25 v_{\mathrm{h}}^{\mathrm{f,n-3}}(\boldsymbol{\Psi}_{\mathrm{h}}^{\mathrm{n}}(\boldsymbol{x},t^{\mathrm{n-3}})). \tag{6.30}$$

Similarly, we also define an alternate function for $\boldsymbol{w}_{\mathrm{h}}^{\mathrm{n}}$ as

$$\boldsymbol{w}_{\mathrm{h}}^{\mathrm{n}}(\boldsymbol{x}) = \sum_{i=1}^{G} \psi_{i}^{\mathrm{f,n}}(\boldsymbol{x}) \frac{1}{\Delta t} \left(\frac{3}{2} x_{i}^{\mathrm{n}} - 2 x_{i}^{\mathrm{n-1}} + \frac{1}{2} x_{i}^{\mathrm{n-2}} \right). \tag{6.31}$$

By redefining $\check{v}_{\mathrm{h}}^{\mathrm{f}}$ and $\boldsymbol{w}_{\mathrm{h}}$ in Eqs. (6.30-6.31) enables us to implement the exact interface continuity i.e.

$$v_{\mathrm{h}}^{\mathrm{f,n}} = v_{\mathrm{h}}^{\mathrm{s,n}} \tag{6.32}$$

instead of the second-order approximation in time given by Eq. (6.10). Unlike the velocity continuity in Eq. (3.96) which requires us to enforce the condition explicitly, we can satisfy the velocity continuity in Eq. (6.32) implicitly by treating the fluid and its corresponding solid node on the interface as a single unique node. Thereby, we can decrease the size of the algebraic system of equations required per time step compared to the implementation presented in Section 6.3.

6.5.1 Algorithm

Unlike the quasi-monolithic combined fluid-structure formulation in Section 6.3 where we have considered $\mathbb{P}_{m}/\mathbb{P}_{m-1}/\mathbb{P}_{m}$ elements to satisfy the inf-sup or LBB condition, here we use equal order elements for both fluid pressure and velocity. The incremental velocity, pressure and eddy viscosity are computed via the matrix-free implementation of the restarted Generalized Minimal RESidual (GMRES) [185]. The basic steps to be performed in the fully-stabilized quasi-monolithic combined fluid-structure formulation are summarized below:

Algorithm 2 Second-order fully stabilized quasi-monolithic formulation for fluid-structure interactions

---

1. Start from known solutions of the field variables $\boldsymbol{v}_h^{f,n-1}, \boldsymbol{v}_h^{f,n-2}, \boldsymbol{v}_h^{s,n-1}, \boldsymbol{v}_h^{s,n-2}, \boldsymbol{\varphi}_h^{s,n-1}$ at time t^{n-1}
2. Advance from t^{n-1} to t^n
   (a) Define the structural position $\boldsymbol{\varphi}_h^{s,n}$ using Eq. (6.7)
   (b) Determine positions of vertices of triangles on the fluid domain $\Omega_h^f(t^n)$
       by solving Eq. (3.104) on $\Omega_h^f(0)$
   (c) Use result from (b) to determine the updated mesh of $\Omega_h^f(t^n)$
   (d) Evaluate $\check{\boldsymbol{v}}_h^f$ and $\boldsymbol{w}_h^n$ by Eqs. (6.30) and (6.31)
   (e) Determine the element level stabilization parameters τ_m and τ_c using
       Eqs. (6.26) and (6.28) respectively
   (f) Solve for the updated field properties $\boldsymbol{v}_h^{f,n}, p_h^n$, and $\boldsymbol{v}_h^{s,n}$ at current time t^n
       using Eq. (6.29)

Similar to the quasi-monolithic formulation presented in Section 6.3, the fully-stabilized quasi-monolithic formulation also solves the combined fluid-structure system only once per time step. A matrix-free version of Krylov subspace iterative solvers are utilized to solve the equations system for the fluid-structure interaction. To scale the fluid-structure solver for large scale computations using distributed memory parallel cluster, we next present the parallel finite element implementation of three dimensional incompressible flow interacting with generic elastic structures for high Reynolds number flow.

6.6 Parallel Implementation

In this section, a parallel fluid-structure interaction strategy for supercomputers based on a hybrid approach is presented. Fluid-structure simulation codes pose serious challenges in terms of implementation and parallel efficiency for large scale problems due to non-local embedded interfaces. In this work, the fluid-structure code based on the stabilized formulation has been parallelized using two strategies: first, the Message Passing Interface (MPI) implementation [2] , where the parallelization is based on a standard domain decomposition master-slave strategy. Secondly, the OpenMP implementation [167]: to treat many-core processors and to exploit thread-levele parallelism of multicore architecture. Since the communications between threads are done via shared memory, a reduction of the communication cost between processors is expected. This hybrid parallelization combines MPI tasks and OpenMP threads to exploit the different levels of parallelism. The present implementation of MPI/OpenMP is general and does not make any assumption regarding the geometry and mesh topologies of fluid-structure system.

The parallelization strategy involves implementation of the fluid and solid solvers to handle both distributed memory and shared memory using the message passing interface [2] and open multi processing [167]. Since both the quasi-monolithic

formulations solve the FSI variables $v^{f,n}, v^{s,n}, \varphi^{s,n}$ and p^n on the combined fluid-structure domain $\Omega_h(t^n)$ at the domain decomposition level we do not distinguish between the fluid and solid domains. The combined fluid-solid mesh is decomposed via an automatic graph partitioner [118] into evenly sized subgrids which can be made-up of both fluid and solid or just fluid or just solid elements. While these subgrids communicate via MPI with a typial master-slave strategy, the internal loops are parallelized using OpenMP to take the advantage from the shared memory in multicore clusters. We next discuss specific details of the hybrid model, with emphasis on the parallel strategy and the linear solver.

(a) initial fluid-structure mesh   (b) decomposed fluid-structure mesh
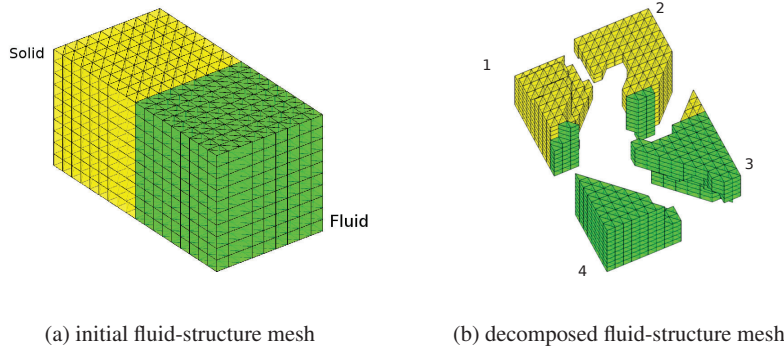
Fig. 6.1 A graphical representation of the combined fluid (green)-structure (yellow) mesh into four subgrids labeled 1, 2, 3 and 4 respectively.

Figure 6.1 demonstrates the domain decomposition strategy described above with the aid of graphical representation. One or more than one subgrid can be assigned to each processor. As mentioned earlier, the communication between the processors is performed with the aid of MPI protocol through a master processor and the element level matrix construction on multiple subgrids in a processor use the OpenMP. One of the key features of our implementation is that we never construct a global left-hand side (LHS) or right-hand side (RHS) matrices. Instead, we only construct element level matrices at subgrid level. The interface nodes on each subgrid communicate the nodal RHS matrix and GMRES(k)/CG AP vector product data through the master processor to include the contributions of the adjacent element present in a different subgrid. We have considered two types of linear solvers: firstly, we implemented conjugate gradient (CG) method for solving the ALE equation and secondly, restarted generalized minimal residual (GMRES-k) method for solving the combined fluid-structure equation. For both these methods, we have used diagonal preconditioners to improve the convergence. Apart from the parallel communication during the AP vector product, the implementation of the CG and GMRES(k) is largely standard, and more details on the linear solver algorithms can be found in [185] and [220]. We summarize the basic step involved in the parallel quasi-monolithic formulation as follow:

Algorithm 3 Parallel implementation of second-order quasi-monolithic formulation for fluid-structure interactions

---

I. Perform the domain decomposition using auto graph partitioner into M subgrids

II. Distribute the M subgrids to N number of processor. For load balancing,
   we assume that M is divisible by N and each processor gets P number of subgrids

  1. On each processor with known solutions of the field variables $\boldsymbol{v}_h^{f,n-1}, \boldsymbol{v}_h^{f,n-2}, \boldsymbol{v}_h^{s,n-1}, \boldsymbol{v}_h^{s,n-2}, \boldsymbol{\varphi}_h^{s,n-1}$
   for the assigned subgrid at time t^{n-1}

  2. Advance from t^{n-1} to t^n on each subgrid

    (a) Define the structural position $\boldsymbol{\varphi}_h^{s,n}$ using Eq. (6.7)

    (b) Determine positions of vertices of triangles on the fluid domain $\Omega_h^f(t^n)$
   by solving Eq. (3.104) on $\Omega_h^f(0)$

    (c) Use result from (b) to determine the updated mesh on each subgrid

    (d) Evaluate $\check{\boldsymbol{v}}_h^f$ and $\boldsymbol{w}_h^n$ by Eqs. (6.30) and (6.31)

    (e) Determine the element level stabilization parameters τ_m and τ_c using
   Eqs. (6.26) and (6.28) respectively

    (f) Solve for the updated field properties $\boldsymbol{v}_h^{f,n}, p_h^n$, and $\boldsymbol{v}_h^{s,n}$ at current time t^n
   using Eq. (6.29)

6.7 Convergence and Verification

Here, numerical experiments are performed to assess the numerical properties of the quasi-monolithic formulation presented in the previous section. Moreover, the accuracy of the two-dimensional and three-dimensional nonlinear coupled FSI framework based on the quasi-monolithic (Section 6.3) and the fully stabilized quasi-monolithic (Section 6.5) formulations, respectively are verified.

6.7.1 Numerical Assessment of Temporal Accuracy

We begin by assessing the temporal accuracy of the second-order formulation discussed in Section 6.3.2. The details of the implementation can be found in [43]. A two-dimensional laminar incompressible flow around a linearly elastic semi-circular cylinder of diameter D placed in a channel is considered. The schematic is shown in Fig. 6.2. The computational domain is rectangular with size $[0, 6.5] \times [-0.5, 1]$. The semi-circular cylinder of $D = 1$ centered at $z_0 = [1.5, -0.5]$ is placed on the floor of the channel. A parabolic velocity profile of $\boldsymbol{v}^f = (U(y,t), 0) = (g(t)(1 + 2y)(1 - y), 0)$ is prescribed at the inlet boundary Γ_{in}^f, where $g(t)$ is a relationship between $U(y,t)$ and t:

$$g(t) = \begin{cases} 0 & t \leq 0 \\ 1 - \cos(\frac{\pi}{4}t) & t \in (0, 2] \\ 1 & t > 2 \end{cases} . \tag{6.33}$$

The top and bottom walls of the domain are considered rigid and a no-slip condition is imposed on those surfaces. A traction-free boundary condition is satisfied at the outlet boundary $\Gamma_{\text{out}}^{\text{f}}$.
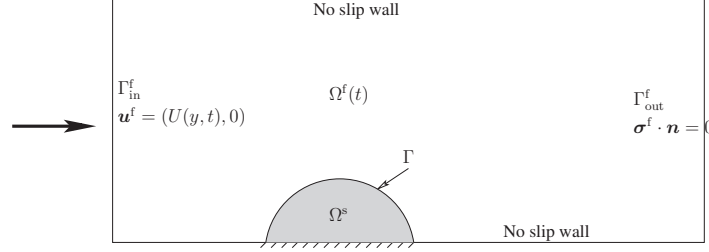
Fig. 6.2 Schematic and computational domain of elastic half-cylinder problem, and details of the boundary conditions.

The density and Lamé's constants for the elastic semi-circular cylinder are considered as $\rho^{\text{s}} = 1$, $\lambda^{\text{s}} = 500$ and $\mu^{\text{s}} = 50$ respectively. The fluid density and kinematic viscosity are $\rho^{\text{f}} = 1$ and $\nu^{\text{f}} = 1$ respectively. Time convergence study is performed by taking different time step sizes of $\Delta t = 1/40$, $1/80$, $1/120$, and $1/160$. For this problem, the spatial discretization of the domain consists of $\mathbb{P}_3/\mathbb{P}_2/\mathbb{P}_3$ higher-order iso-parametric finite elements for the fluid velocity, pressure and structural velocity, respectively. The fluid and structural mesh comprises of 1239 and 370 triangular elements respectively.

(a)   (b)
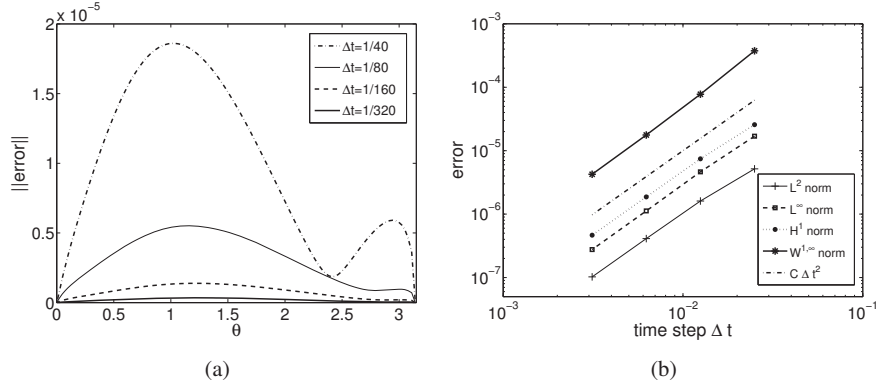
Fig. 6.3 Elastic half-cylinder problem: (a) error in position along the interface at t=1, where $|\boldsymbol{\varphi}(\boldsymbol{X},1) - \boldsymbol{\varphi}_{\text{h}}(\boldsymbol{X},1)|_{\ell^2}$ versus θ and $\theta = \theta(\boldsymbol{X})$ is the angle between $(\boldsymbol{X} - \boldsymbol{X}_0)$ and the positive x-axis. (b) 2nd order convergence of structural velocity in various norms.

The temporal accuracy is determined by computing the error in the solutions of fluid velocity, pressure and structural displacement for the various values of Δt con-
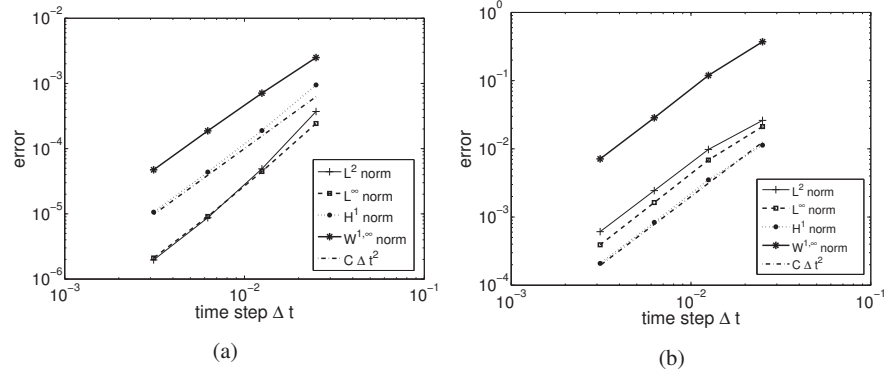
Fig. 6.4 Second order convergence in various norms at time t=1 for fluid (a) velocity, (b) pressure.

sidered. The numerical solution at $\Delta t = 2 \times 10^{-5}$ is selected as the reference solution to compute the errors. The L_2 error of the interface position at $t = 1$ considering various Δt is computed as

$$\|\text{error}(\boldsymbol{\theta})\| = \left(\left|\boldsymbol{\varphi}(\boldsymbol{X},1)_{\Delta t=2\times10^{-5}} - \boldsymbol{\varphi}_{\text{h}}(\boldsymbol{X},1)\right|_{\ell^2}\right) \ \forall \ \boldsymbol{X} \in \Gamma, \qquad (6.34)$$

where $\theta = \theta(z)$ is the angle measured for each of the interface nodes with respect to the positive X-axis. This error is shown in Fig. 6.3(a). Moreover, Figs. 6.3(b) and 6.4 depict the errors in the structural velocity, fluid velocity and fluid pressure respectively for the different discrete norms, Lebesgue L_∞, L_2, Hilbert H^1, and Sobolev W^1_∞. It is evident that the slope of the plot is 2, which shows a second-order of temporal accuracy for the quasi-monolithic formulation presented in Section 6.3.2.

6.7.2 Verification of 2D and 3D FSI Frameworks

In the current section, a two-dimensional FSI benchmark given in [216] is performed to verify the 2D and 3D frameworks based on the formulations presented in Sections 6.3 and 6.5 respectively. The benchmark consists of a stationary rigid cylinder with a flexible bar Ω^s attached to its end, placed in a channel flow $\Omega^\text{f}(t)$, as shown in Fig. 6.5. The channel is modeled as a rectangular computational domain with length $L = 2.5$ and height $H = 0.41$. For the 3D framework, the width of the domain in the third dimension is considered as $W = 1$. The origin of the coordinate system lies at the bottom-left corner of the domain. The center of the cylinder is at $C = (0.2, 0.2)$ with $D = 0.1$ as its diameter. The length and thickness of the bar attached to the cylinder are $l = 0.35$ and $h = 0.02$ respectively. The fluid-structure interface is denoted by Γ.

A parabolic velocity is prescribed at the inlet of the channel $\Gamma^\text{f}_\text{in}$ as
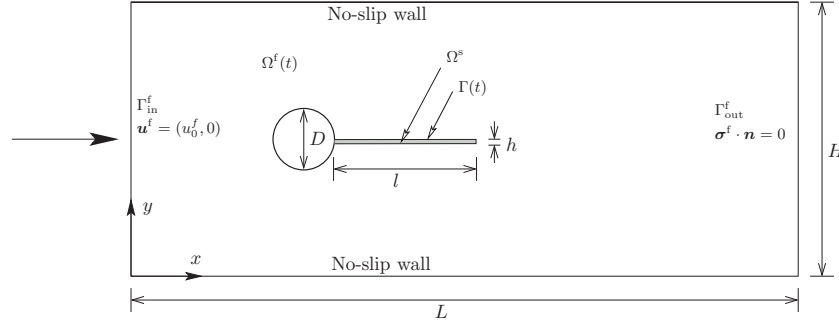
Fig. 6.5 Schematic and computational domain of cylinder-bar problem, and details of the boundary conditions and fluid-structure interface.

$$\boldsymbol{v}^{\mathrm{f}} = (U(y,t),0) = \frac{6.0}{0.1641} g(t) \bar{U} y (0.41 - y), \qquad (6.35)$$

where $\bar{U}$ represents the mean inlet velocity and $g(t)$ is defined as

$$g(t) = \begin{cases} 0 & t \leq 0 \\ 1 - \cos(\frac{\pi}{4}t) & t \in (0,2] \\ 1 & t > 2 \end{cases} . \qquad (6.36)$$

A traction-free boundary condition is satisfied at the outlet boundary $\Gamma_{\mathrm{out}}^{\mathrm{f}}$. The stationary cylinder, the top and the bottom walls of the channel are assumed as rigid surfaces and a no-slip condition is imposed on these surfaces.

Two test cases are considered for the FSI benchmark of [216], consisting of a steady and unsteady FSI problem. For the steady FSI case, the non-dimensional parameters are given as $Re = 20$, $\bar{U} = 0.2$, $\rho^{\mathrm{s}}/\rho^{\mathrm{f}} = 1$, $\nu^{\mathrm{s}} = 0.4$ and $E/(\rho^{\mathrm{f}} \times \bar{U}^2) = 3.5 \times 10^4$. Similarly, the non-dimensional parameters for the unsteady FSI case are $Re = 100$, $\bar{U} = 1.0$, $\rho^{\mathrm{s}}/\rho^{\mathrm{f}} = 10$, $\nu^{\mathrm{s}} = 0.4$ and $E/(\rho^{\mathrm{f}} \times \bar{U}^2) = 1.4 \times 10^3$.

6.7.2.1 2D Quasi-Monolithic Formulation

We first consider the two-dimensional implementation of the quasi-monolithic formulation discussed in Section 6.3. The spatial discretization meshes considered for the two FSI cases are identical. The higher-order finite-element fluid and structural meshes consist of 9156 $\mathbb{P}_2/\mathbb{P}_1$ and 1064 $\mathbb{P}_2$ elements, respectively.

The first steady state FSI case is carried out at a constant $\Delta t = 0.005$. The evolution of the displacements of the tip of the trailing edge of the flexible bar in the streamwise and cross-stream directions are shown in Fig. 6.6. The steady state response of the FSI case can be clearly seen from the figure. The drag and lift forces on the cylinder-bar system have been plotted in Fig. 6.7. The results of the 2D computation for the steady state FSI problem are summarized in Table 6.1, where they
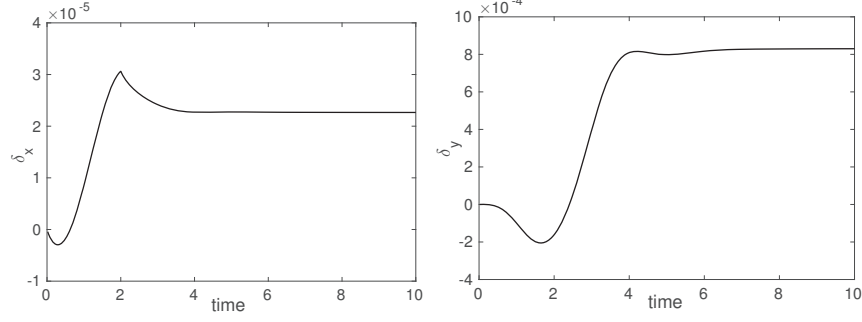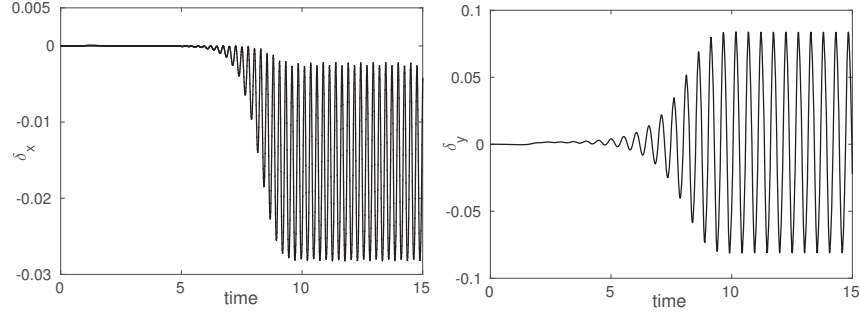
Fig. 6.6 Time history of trailing edge tip-displacements in lateral (left) and transverse (right) directions for cylinder bar problem simulated using 2D quasi-monolithic FSI solver with $\rho^s/\rho^f = 1$, $Re_D = 20$ and $E/\rho^f U_0^2 = 3.5 \times 10^4$.
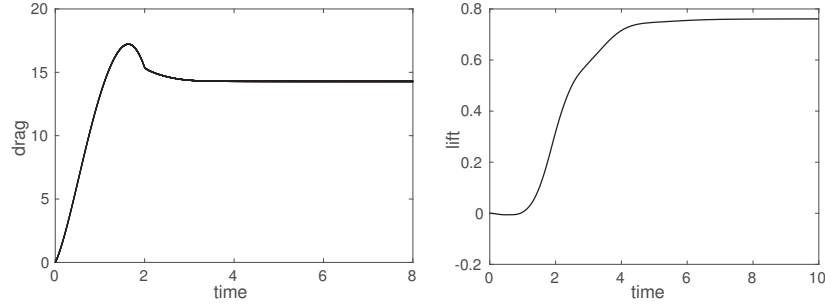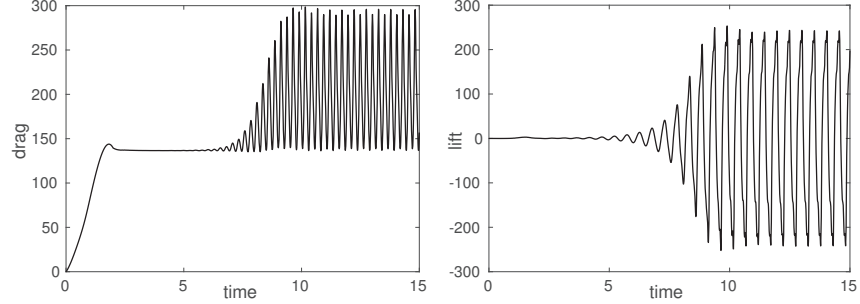

Fig. 6.7 Time history of dynamic forces drag (left) and lift (right) acting on a cylinder with flexible bar simulated using 2D quasi-monolithic FSI solver. Simulation parameter considered are $\rho^s/\rho^f = 1$, $Re_D = 20$ and $E/\rho^f U_0^2 = 3.5 \times 10^4$.

are compared with the result from [216]. It is observed that the results agree very well with the benchmark data. The maximum difference between the computation results and the benchmark data is approximately 1%.

Table 6.1 Summary of simulation results for the steady FSI problem simulated using the 2D quasi-monolithic formulation.

Quantity	Present	Turek et al. [216]
$u_x \times 10^{-4}$	0.2265(0.22%)	0.2270
$u_y \times 10^{-3}$	0.830(1.09%)	0.821
Drag	14.28(0.07%)	14.27
Lift	0.761(0.26%)	0.763

The unsteady FSI case at $Re = 100$ are performed considering a constant $\Delta t = 0.001$. The tip displacements of the trailing edge of the flexible bar and the fluid forces on the combined cylinder-bar system are shown in Figs. 6.8 and 6.9, respectively. The unsteady periodic results are summarized in Table 6.2 and compared with that of the benchmark in [216]. A good agreement with the results from the literature is observed. The percentage difference in the unsteady component compared to the benchmark results is given in the parentheses.
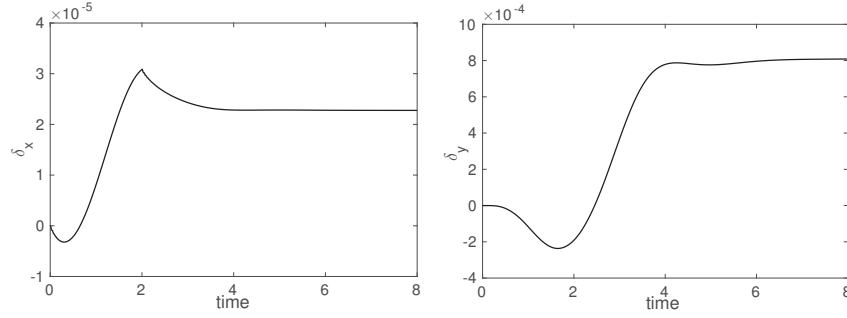

Fig. 6.8 Time history of trailing edge tip-displacements in lateral (left) and transverse (right) directions for cylinder bar problem simulated using 2D quasi-monolithic FSI solver with $\rho^s/\rho^f = 10$, $Re_D = 100$ and $E/\rho^f U_0^2 = 1.4 \times 10^3$.
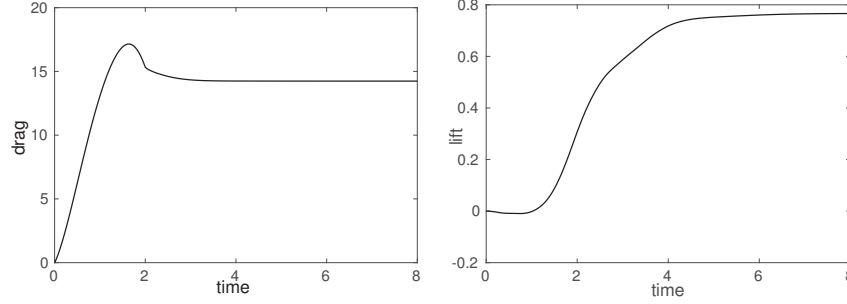

Fig. 6.9 Time history of dynamic forces drag (left) and lift (right) acting on a cylinder with flexible bar simulated using 2D quasi-monolithic FSI solver. Simulation parameter considered are $\rho^s/\rho^f = 10$, $Re_D = 100$ and $E/\rho^f U_0^2 = 1.4 \times 10^3$.

6.7.2.2 3D Fully-Stabilized Quasi-Monolithic Formulation

Next, we consider the three-dimensional fully-stabilized quasi-monolithic formulation discussed in Section 6.5. Here, we perform pseudo-2D computations taking

Table 6.2 Summary of simulation results for the unsteady FSI problem simulated using the 2D quasi-monolithic formulation.

Quantity	Present		Turek et al.[216]	
	Value	Frequency	Value	Frequency
$u_x \times 10^{-3}$	-15.25 ± 12.65 (1.68%)	3.8	-14.58 ± 12.44	3.8
$u_y \times 10^{-3}$	1.30 ± 82.43 (2.28%)	1.9	1.23 ± 80.60	2.0
Drag	215 ± 75.25 (2.03%)	3.8	208 ± 73.75	3.8
Lift	2.70 ± 239 (2.05%)	2.0	-0.88 ± 234.20	2.0

the three-dimensional mesh to be one element thick in the third dimension. A typical three-dimensional computational domain for the problem is shown in Fig. 6.10. The boundary conditions are similar to the set-up in 2D computational domain in Fig. 6.5, but also includes the periodic condition on the sides in the third dimension.
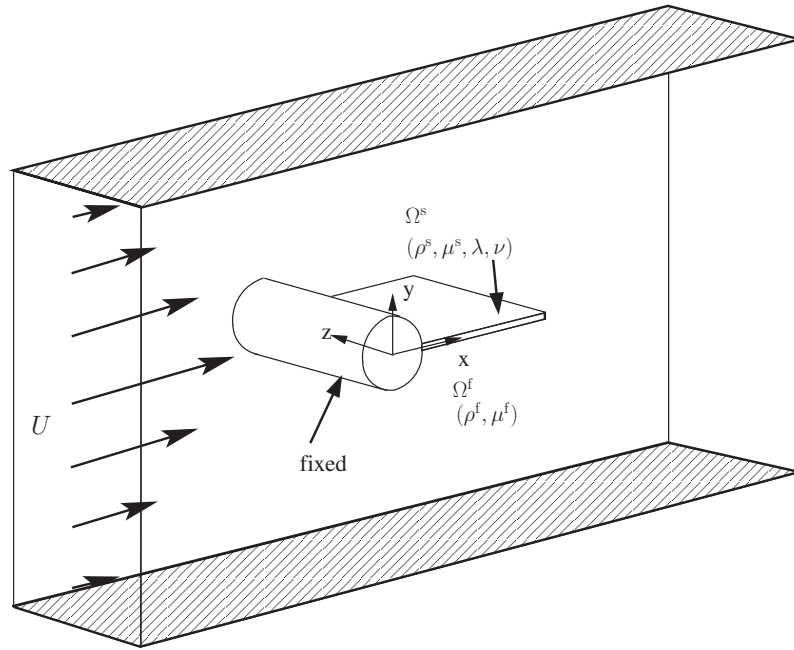
Fig. 6.10 Schematic of 3D rigid fixed cylinder attached with a flexible plate in a channel flow.

The fluid mesh comprises of 15348 six-node wedge elements and 16342 nodes. Identical order elements are used for both fluid velocity and pressure interpolations in the fully-stabilized formulation. The computation results for the steady and un-

steady cases are shown in Figs. 6.11-6.14. The results are also summarized in Tables 6.3 and 6.4 and compared to the benchmark results for the cases $Re = 20$ and 100, respectively. The percentage error between the computation and the benchmark results is shown in the parentheses, where we observe a maximum error of less than 2%. Therefore, the 3D fully-stabilized quasi-monolithic formulation provides a good agreement with the benchmark solutions in [216].
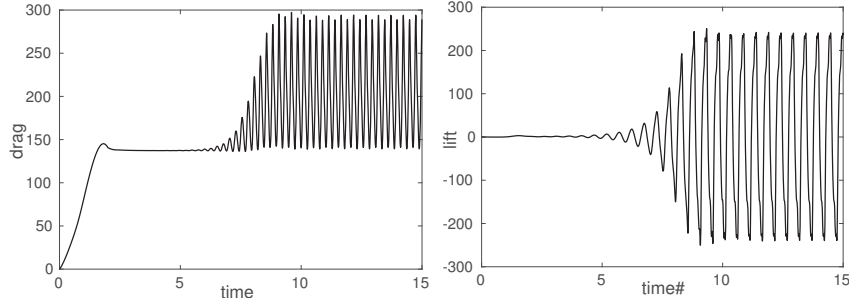

Fig. 6.11 Time history of trailing edge tip-displacements in lateral (left) and transverse (right) directions for cylinder bar problem simulated using fully stabilized 3D quasi-monolithic formulation with $\rho^s/\rho^f = 1$, $Re_D = 20$ and $E/\rho^f U_0^2 = 3.5 \times 10^4$.

Fig. 6.12 Time history of dynamic forces drag (left) and lift (right) acting on a cylinder with flexible bar for the numerical simulations carried out using fully stabilized 3D quasi-monolithic formulation. Simulation parameter considered are $\rho^s/\rho^f = 1$, $Re_D = 20$ and $E/\rho^f U_0^2 = 3.5 \times 10^4$.

Table 6.3 Summary of simulation results for the steady FSI problem simulated using the fully stabilized 3D quasi-monolithic formulation.

Quantity	Present	Turek et al. [216]
$u_x \times 10^{-3}$	0.0227(0%)	0.0227
$u_y \times 10^{-3}$	0.810(1.34%)	0.821
Drag	14.24(0.21%)	14.27
Lift	0.754(1.18%)	0.763

Table 6.4 Summary of simulation results for the unsteady FSI problem simulated using the fully stabilized 3D quasi-monolithic formulation.

Quantity	Present		Turek et al.[216]	
	Value	Frequency	Value	Frequency
$u_x \times 10^{-3}$	$-14.90 \pm 12.60(1.26\%)$	3.8	-14.58 ± 12.44	3.8
$u_y \times 10^{-3}$	$0.80 \pm 81.06(0.82\%)$	1.9	1.23 ± 80.60	2.0
Drag	$216 \pm 75.0(1.69\%)$	3.8	208 ± 73.75	3.8
Lift	$0.50 \pm 239.05(1.77\%)$	2.0	-0.88 ± 234.20	2.0
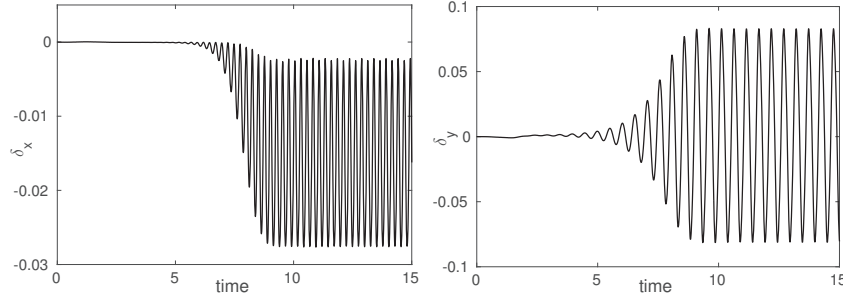
Fig. 6.13 Time history of trailing edge tip-displacements in lateral (left) and transverse (right) directions for cylinder bar problem with $\rho^s/\rho^f = 10$, $Re_D = 100$ and $E/\rho^f U_0^2 = 1.4 \times 10^3$.

6.7.3 Verification for Flapping Dynamics

After the verification of the quasi-monolithic FSI framework for the benchmark FSI problem, we demonstrate the framework for two-dimensional flapping dynamics of a thin flexible foil of length L subjected to a uniform axial flow. The leading edge of the foil is clamped, while the trailing edge is free to undergo flapping. The non-dimensional parameters for the demonstration are mass-ratio $m^* = 0.1$, Reynolds numbers $Re = 1000$ and non-dimensional bending rigidity $K_B = 0.0001$. The results are compared with the results in [51].

Fig. 6.14 Time history of trailing edge tip-displacements in lateral (left) and transverse (right) directions for cylinder bar problem with $\rho^s/\rho^f = 10$, $Re_D = 100$ and $E/\rho^f U_0^2 = 1.4 \times 10^3$.

The 2D formulation is verified by considering a rectangular computational domain of size $[-2L, 20L] \times [-5L, 5L]$. The origin is located at the leading edge center of the foil. The thickness h of the foil is assumed very less than its length, $h \ll L$ and $h/L = 0.01$. A uniform velocity $\boldsymbol{v}^f = (U_0, 0)$ is applied at the inlet boundary Γ_{in}^f and a traction-free condition is satisfied at the outlet Γ_{out}^f. The freestream velocity condition $\boldsymbol{v}^f = (U_0, 0)$ is given at the top and bottom sides of the computational domain. The mesh consists of higher-order finite-element fluid and structural meshes comprising of 15699 and 792 triangular $\mathbb{P}_2/\mathbb{P}_1$ and $\mathbb{P}_2$ respectively.

The 3D formulation is verified by constructing a pseudo-2D domain, extruding the 2D mesh by a single element in the third dimension. Periodic conditions are imposed in the spanwise direction. An isometric view of the 3D fluid mesh consisting of 116461 six-node wedge elements and 117402 nodes is depicted in Fig. 6.15(a). The close-up view of the fluid boundary layer mesh around the foil is also shown in Fig. 6.15(b).

The results obtained from the 2D and 3D formulations for the non-dimensional parameters $m^* = 0.1$, $Re = 1000$ and $K_B = 0.0001$ are summarized in Table 6.5. The flapping amplitude, frequency and trailing edge root mean square displacement are compared with the results from the literature [51]. A reasonable agreement is found among the flapping properties from both the 2D and 3D formulations.

Table 6.5 Numerical comparison of the fully-stabilized 3D quasi-monolithic solver against reference results of [51, 139] for $m^* = 0.1$, $Re = 1000$ and $K_B = 0.0001$.

Quantity	Connell et al. [51] (2D simulations)	2D solver	3D solver
A/L	0.2540	0.2440	0.2420
δ_y^{rms}/L	-	0.0846	0.0826
fL/U_0	0.9152	0.9495	0.955
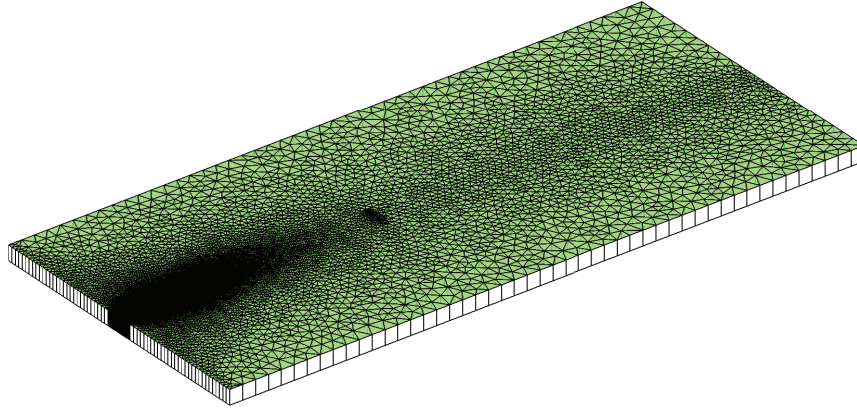
(a)
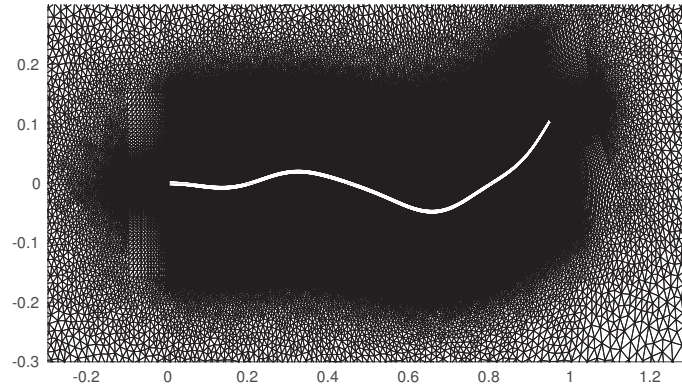
(b)

Fig. 6.15 3D finite-element fluid mesh considered for the validation of the 3D coupled fluid-structure solver for $m^* = 0.1$, $Re = 1000$ and $K_B = 0.0001$: (a) isometric view, (b) closeup view of the fluid boundary layer mesh around the foil while performing flapping motion.

To summarize, we discussed monolithic strategy for dealing with coupled fluid-structure interaction problems in this chapter. Different quasi-monolithic formulations were presented and verified with standard FSI benchmarks available in the literature. Finally, flapping dynamics of a flexible foil was demonstrated with the help of the underlying presented formulations. Next, we deal with the second type of strategy for FSI problems, i.e., partitioned type of techniques.

Chapter 7
Partitioned Fluid-Structure Interaction Methods

7.1 Introduction

In the previous chapters, we formulated the finite element discretization of the fluid-structure interaction equations and looked into the monolithic type of coupling methods. An essential requirement of such a coupled system is the accurate description of the fluidstructure interface. In the monolithic technique, this feature is naturally taken care by the formulation as the dynamic equilibrium is easily satisfied. In this chapter, we look into the treatment of the fluid-structure interface and interface conditions for partitioned type of methods. While partitioning refers to the decomposition into the fluid and structural subdomains at a given time level, staggering is the sequence in which time integration is carried out along the interface between the subdomains, by satisfying the kinematic and dynamic equilibrium conditions at the interface.

For such problems under the partitioned staggered approach, one faces two key challenges. The first challenge is how to deal with the displacement and traction transfer across different mesh discretizations across the fluid and structural subdomains. The discretizations of the subdomains can be generally non-matching. The issue then arises into how to couple the subdomains in space while satisfying the interface equilibrium conditions in an accurate and conservative manner. These give rise to different spatial coupling techniques at the fluid-structure interface.

The second challenge is the stability, accuracy and convergence of the staggered time integration scheme at the fluid-structure interface which is used to couple the different subdomains in time. With regard to temporal coupling, the techniques can be categorized into (i) loosely coupled, and (ii) strongly coupled schemes. Loosely coupled schemes involve explicit time integration where the fluid and structural subdomains are evolved in time once at each time step. These schemes are simple and have the advantage of low computational cost, but they often suffer from numerical instabilities and temporal inaccuracy. The latter involves predictor-corrector sub-iterations to ensure convergence of the properties at the interface at each time step.

In this chapter, we discuss the various types of spatial and temporal coupling techniques helpful in partitioned methods for fluid-structure coupling. We carry out error analysis for some of the coupling methods along with the verification with results from the literature. Finally, we demonstrate the partitioned staggered coupling technique for a problem of vortex-induced vibration of an offshore riser subjected to uniform flow current.

7.2 Spatial Coupling Techniques

This section deals with the different kinds of coupling techniques based on the spatial discretization of the fluid-structure interface. It discusses how the displacement and tractions can be transferred across the interface in a conservative and accurate manner. First, we define some notations to be used in the upcoming subsections and then dive into the details of the techniques.

Let N_i^{f} and N_j^{s} denote the finite element shape functions associated with node i and j of the fluid and structural mesh respectively at the fluid-structure interface Γ. The approximate tractions at the corresponding nodes of the discrete mesh are given by $\tilde{t}_i^{\mathrm{f}} \in L^2(\Omega^{\mathrm{f}}(t))$ and $\tilde{t}_j^{\mathrm{s}} \in L^2(\Omega^{\mathrm{s}})$. The continuum fields for the traction are thus given by t^{f} and t^{s} as

$$t^{\mathrm{f}} \approx \sum_{i=1}^{m^{\mathrm{f}}} N_i^{\mathrm{f}} \tilde{t}_i^{\mathrm{f}}, \qquad (7.1)$$

$$t^{\mathrm{s}} \approx \sum_{j=1}^{m^{\mathrm{s}}} N_j^{\mathrm{s}} \tilde{t}_j^{\mathrm{s}}, \qquad (7.2)$$

where m^{f} and m^{s} denote the number of fluid and structural nodes on the interface respectively and $\tilde{t}_i^{\mathrm{f}}$ and $\tilde{t}_j^{\mathrm{s}}$ denote the discrete values of the traction for the fluid and structural interfaces respectively.

Based on the type of spatial coupling, the techniques can be categorized into: (a) point-to-point mapping, (b) point-to-element projection, and (c) common-refinement projection.

7.2.1 Point-to-Point Mapping

In the case of interaction of fluid and multiple components of a flexible multibody system, it is essential that there is accurate and conservative data transfer across the fluid-structure interface. For problems considering large deformations of the structure, global conservation methods such as point-to-point mapping (e.g., radial basis function with compact support) are preferred which is like an interpolation with the help of scattered data points. The benefit with such mapping is that it does

not require connectivity of the mesh while transferring the data across the fluid-structure interface.

Remark 7.1. The global conservation property is satisfied by equating the virtual work done by the forces in the structural domain (δW^{s}) by that carried out by the fluid loads (δW^{f}) at the fluid-structure interface. The interpolation with the help of radial basis function is constructed in such a manner that the global conservation is satisfied across the interface. Let the interpolation of the fluid displacement at the interface be given by $\boldsymbol{u}^{\mathrm{f}} = \boldsymbol{H}\boldsymbol{u}^{\mathrm{s}}$, where $\boldsymbol{u}^{\mathrm{s}}$ is the structural displacement to be transferred and $\boldsymbol{H}$ is some interpolation matrix. The force transfer from the fluid nodes to the structural nodes is represented as $\boldsymbol{f}^{\mathrm{s}} = \boldsymbol{H}^T \boldsymbol{f}^{\mathrm{f}}$, where $\boldsymbol{f}^{\mathrm{s}}$ and $\boldsymbol{f}^{\mathrm{f}}$ denote the contributions of the forces from the structural and fluid domains, respectively. The virtual work done at the fluid-structure interface can be expressed as

$$\delta W^{\mathrm{f}} = \delta \boldsymbol{u}^{\mathrm{f}} \cdot \boldsymbol{f}^{\mathrm{f}} = (\delta \boldsymbol{u}^{\mathrm{f}})^T \boldsymbol{f}^{\mathrm{f}}, \tag{7.3}$$

$$= (\delta \boldsymbol{u}^{\mathrm{s}})^T \boldsymbol{H}^T \boldsymbol{f}^{\mathrm{f}}, \tag{7.4}$$

$$= (\delta \boldsymbol{u}^{\mathrm{s}})^T \boldsymbol{f}^{\mathrm{s}}, \tag{7.5}$$

$$= \delta \boldsymbol{u}^{\mathrm{s}} \cdot \boldsymbol{f}^{\mathrm{s}} = \delta W^{\mathrm{s}}, \tag{7.6}$$

Thus, if an approximation matrix $\boldsymbol{H}$ exists, it can be utilized for both displacement and force interpolations across the interface [24, 89]. Here, we discuss the construction of the interpolation matrix $\boldsymbol{H}$ with the help of radial basis functions.

7.2.1.1 Review of Radial Basis Functions

We next review the concept of radial basis functions. A radially basis function (RBF) is radially symmetric and forms the basis of the interpolation matrix. A d-variate interpolation function $g(\boldsymbol{x})$ from a given scattered data $\{g_1, g_2, ..., g_N\}$ at the arbitrary distinct source locations $X^{\mathrm{c}} = \{\boldsymbol{x}_1^{\mathrm{c}}, \boldsymbol{x}_2^{\mathrm{c}}, ..., \boldsymbol{x}_N^{\mathrm{c}}\} \subseteq \mathbb{R}^d$ is given as

$$g(\boldsymbol{x}) = \sum_{j=1}^{N} \alpha_j \phi(||\boldsymbol{x} - \boldsymbol{x}_j^{\mathrm{c}}||), \tag{7.7}$$

where $|| \cdot ||$ is the Euclidean norm and α_j are the weights for the basis functions. If the weights are known, the interpolated values at the requested target data points $X^{\mathrm{t}} = \{\boldsymbol{x}_1^{\mathrm{t}}, \boldsymbol{x}_2^{\mathrm{t}}, ..., \boldsymbol{x}_M^{\mathrm{t}}\}$ are thus given by

$$g(\boldsymbol{x}_i^{\mathrm{t}}) = \sum_{j=1}^{N} \alpha_j \phi(||\boldsymbol{x}_i^{\mathrm{t}} - \boldsymbol{x}_j^{\mathrm{c}}||), \ 1 \leq i \leq M, \tag{7.8}$$

where the matrix $\phi(||\boldsymbol{x}_i^{\mathrm{t}} - \boldsymbol{x}_j^{\mathrm{c}}||)$ is also known as kernel matrix for the interpolation.

The coefficients α_j are determined by the condition, $g(\boldsymbol{x}_j^{\mathrm{c}}) = g_j, \ 1 \leq j \leq N$. Therefore, the interpolation recovers to the exact values at the scattered control points, i.e., for $\boldsymbol{x}^{\mathrm{t}} = \boldsymbol{x}^{\mathrm{c}}$,

$$g_j = g(\boldsymbol{x}_j^{\mathrm{c}}) = \sum_{j=1}^{N} \alpha_j \phi(||\boldsymbol{x}_i^{\mathrm{c}} - \boldsymbol{x}_j^{\mathrm{c}}||), \ 1 \leq i \leq N, \tag{7.9}$$

which is a system of linear equations with α_j as unknowns and let $(\boldsymbol{A}_{\mathrm{cc}})_{ij} = \phi(||\boldsymbol{x}_i^{\mathrm{c}} - \boldsymbol{x}_j^{\mathrm{c}}||)$. To have a guaranteed solvability for these coefficients, the symmetric matrix $\boldsymbol{A}_{\mathrm{cc}}$ should be positive definite which depends on the positive-definiteness of the radial basis function $\phi(|| \cdot ||)$.

Remark 7.2. The positive definite property can be imparted to a radial basis function by adding polynomials to the interpolant as

$$g(\boldsymbol{x}^{\mathrm{t}}) = \sum_{j=1}^{N} \alpha_j \phi(||\boldsymbol{x}^{\mathrm{t}} - \boldsymbol{x}_j^{\mathrm{c}}||) + q(\boldsymbol{x}^{\mathrm{t}}), \tag{7.10}$$

where $q(\boldsymbol{x}^{\mathrm{t}})$ is a polynomial. Now, with additional degrees of freedom of the coefficients of the polynomial, the condition $\sum_{j=1}^{N} \alpha_j p(\boldsymbol{x}_j^{\mathrm{t}}) = 0$, has to be satisfied for unique solvability of the coefficients, for any polynomial $p(\boldsymbol{x})$ with degree less than or equal to the degree of $q(\boldsymbol{x})$. A minimal degree of the polynomial $q(\boldsymbol{x}^{\mathrm{t}})$ depends on the radial basis function.

The radial basis function can be selected among many alternatives, namely Gaussian, multiquadric, polyharmonic, etc., satisfying certain conditions for the positive definite property. Besides the positive definiteness property, the property of localization or compact support is also beneficial for a radial basis function. Such localization ensures that the system matrix is sparse, which is helpful in its inversion. A good example of functions having compact support is the class of Wendland's function, which are always positive definite up to a maximal space dimension and have smoothness C^{2k}. They are of the form

$$\phi(r) = \begin{cases} p(r), & 0 \leq r \leq 1, \\ 0, & r > 1, \end{cases} \tag{7.11}$$

where $p(r)$ is a univariate polynomial. Considering a truncated power function $\phi_l(r) = (1-r)^l$ which satisfies the positive definiteness property for $l \geq \lfloor d/2 \rfloor + 1$, d being the spatial dimensions and $\lfloor x \rfloor$ represents an integer n such that $n \leq x < n+1$. Using this definition, a new class of functions is constructed $\phi_{l,k}(r)$ which are positive definite in the dimension d and are C^{2k} with degree $\lfloor d/2 \rfloor + 3k + 1$ [237]. If one defines an operator $I(f)(r) = \int_r^{\infty} f(t)t dt$, these new class of functions can be constructed via integration as $\phi_{l,k}(r) = I^k \phi_l(r)$, which can be represented by

$$\phi_{l,k}(r) = \sum_{n=0}^{k} \beta_{n,k} r^n \phi_{l+2k-n}(r), \tag{7.12}$$

where $\beta_{0,0} = 1$ and

$$\beta_{j,k+1} = \sum_{n=j-1}^{k} \beta_{n,k} \frac{[n+1]_{n-j+1}}{(l+2k-n+1)_{n-j+2}}, \qquad (7.13)$$

where $[q]_{-1} = 1/(q+1)$, $[q]_0 = 1$, $[q]_l = q(q-1)...(q-l+1)$ and $(q)_0 = 1$, $(q)_l = q(q+1)...(q+l-1)$. It has also been shown in [237] that a function $\Phi_{l,k}(x) = \phi_{l,k}(||x||)$ has strictly positive Fourier transform and produces a positive definite radial basis function, except when $d = 1$ and $k = 0$. Furthermore, it has been proven that the function is $2k$ times continuously differentiable and their polynomial degree is minimal for a given smoothness, and they are related to certain Sobolev spaces [241, 237, 238]. Considering Wendland's C^2 function for the three-dimensional study ($d = 3$) with $k = 1$ and choosing $l = \lfloor d/2 \rfloor + k + 1$ as $\phi_{3,1}(r)$ written as

$$\phi(||\boldsymbol{x}||) = \begin{cases} (1 - ||\boldsymbol{x}||)^4(1 + 4||\boldsymbol{x}||), & 0 \le ||\boldsymbol{x}|| \le 1, \\ 0, & ||\boldsymbol{x}|| > 1. \end{cases} \qquad (7.14)$$

7.2.1.2 Application to Fluid-Structure Interaction Framework

For the three-dimensional fluid-structure interaction problems and the use of Wendland's C^2 function, we can employ a linear polynomial $q(\boldsymbol{x}) = \lambda_0 + \lambda_1 x + \lambda_2 y + \lambda_3 z$, which is exactly reproduced and recovers any rigid body translation and rotation in the mapping. Note that the radial basis function can be scaled by a compact support radius r which gives the advantage of covering enough number of interpolation points depending on the application. This scaling, however, does not have any effect on the positive definiteness and the compact support properties of the function. The scaled Wendland's C^2 function is given by

$$\phi(||\boldsymbol{x}||/r) = \begin{cases} (1 - ||\boldsymbol{x}||/r)^4(1 + 4||\boldsymbol{x}||/r), & 0 \le ||\boldsymbol{x}||/r \le 1, \\ 0, & ||\boldsymbol{x}||/r > 1. \end{cases} \qquad (7.15)$$

Next, we discuss how the interpolation matrix obtained from radial basis functions can be used to obtain the displacements and fluid tractions across the fluid-structure interface. Suppose the structural displacement field is known at the fluid-structure interface as $\boldsymbol{u}_I^s$ and we want to interpolate the fluid displacement at the interface $\boldsymbol{u}_I^f$. Based on the RBF interpolation, the coefficients β_j can be found by the fact that $\boldsymbol{u}_I^s = \boldsymbol{C}_{ss}\boldsymbol{\beta}$, where $\boldsymbol{C}_{ss}$ is given as

$$
\boldsymbol{C}_{\mathrm{ss}} =
\begin{bmatrix}
0 & 0 & 0 & 0 & 1 & 1 & \cdots & 1 \\
0 & 0 & 0 & 0 & x_1^{\mathrm{c}} & x_2^{\mathrm{c}} & \cdots & x_N^{\mathrm{c}} \\
0 & 0 & 0 & 0 & y_1^{\mathrm{c}} & y_2^{\mathrm{c}} & \cdots & y_N^{\mathrm{c}} \\
0 & 0 & 0 & 0 & z_1^{\mathrm{c}} & z_2^{\mathrm{c}} & \cdots & z_N^{\mathrm{c}} \\
1 & x_1^{\mathrm{c}} & y_1^{\mathrm{c}} & z_1^{\mathrm{c}} & \phi_{1,1}^{\mathrm{c,c}} & \phi_{1,2}^{\mathrm{c,c}} & \cdots & \phi_{1,N}^{\mathrm{c,c}} \\
1 & x_2^{\mathrm{c}} & y_2^{\mathrm{c}} & z_2^{\mathrm{c}} & \phi_{2,1}^{\mathrm{c,c}} & \phi_{2,2}^{\mathrm{c,c}} & \cdots & \phi_{2,N}^{\mathrm{c,c}} \\
\vdots & \vdots & \vdots & \vdots & \vdots & \vdots & \ddots & \vdots \\
1 & x_N^{\mathrm{c}} & y_N^{\mathrm{c}} & z_N^{\mathrm{c}} & \phi_{N,1}^{\mathrm{c,c}} & \phi_{N,2}^{\mathrm{c,c}} & \cdots & \phi_{N,N}^{\mathrm{c,c}}
\end{bmatrix},
\tag{7.16}
$$

where $\phi_{i,j}^{\mathrm{c,c}} = \phi(||\boldsymbol{x}_i^{\mathrm{c}} - \boldsymbol{x}_j^{\mathrm{c}}||)$, where $\boldsymbol{x}_i^{\mathrm{c}}$ are the coordinates of the points on the structural interface at Γ_i. The displacement field of the fluid nodes at the interface can be interpolated by $\boldsymbol{u}_I^{\mathrm{f}} = \boldsymbol{A}_{\mathrm{fs}} \boldsymbol{C}_{\mathrm{ss}}^{-1} \boldsymbol{u}_I^{\mathrm{s}}$, where $\boldsymbol{A}_{\mathrm{fs}}$ is given by

$$
\boldsymbol{A}_{\mathrm{fs}} =
\begin{bmatrix}
1 & x_1^{\mathrm{t}} & y_1^{\mathrm{t}} & z_1^{\mathrm{t}} & \phi_{1,1}^{\mathrm{t,c}} & \phi_{1,2}^{\mathrm{t,c}} & \cdots & \phi_{1,N}^{\mathrm{t,c}} \\
1 & x_2^{\mathrm{t}} & y_2^{\mathrm{t}} & z_2^{\mathrm{t}} & \phi_{2,1}^{\mathrm{t,c}} & \phi_{2,2}^{\mathrm{t,c}} & \cdots & \phi_{2,N}^{\mathrm{t,c}} \\
\vdots & \vdots & \vdots & \vdots & \vdots & \vdots & \ddots & \vdots \\
1 & x_M^{\mathrm{t}} & y_M^{\mathrm{t}} & z_M^{\mathrm{t}} & \phi_{M,1}^{\mathrm{t,c}} & \phi_{M,2}^{\mathrm{t,c}} & \cdots & \phi_{M,N}^{\mathrm{t,c}}
\end{bmatrix},
\tag{7.17}
$$

where $\phi_{i,j}^{\mathrm{t,c}} = \phi(||\boldsymbol{x}_i^{\mathrm{t}} - \boldsymbol{x}_j^{\mathrm{c}}||)$, $\boldsymbol{x}_i^{\mathrm{t}}$ being the coordinates of the fluid points on the interface. Therefore, the mapping of the fluid displacements to the structural displacements can be described as $\boldsymbol{u}_I^{\mathrm{f}} = \boldsymbol{A}_{\mathrm{fs}} \boldsymbol{C}_{\mathrm{ss}}^{-1} \boldsymbol{u}^{\mathrm{s}} = \boldsymbol{H} \boldsymbol{u}_I^{\mathrm{s}}$.

The same technique can be applied for the transfer of tractions from fluid points to the structural points at the interface by considering the control points to be that of the fluid side of the interface and target points as that of the structural side. Similar to the finite element method, the local support of RBF makes the system matrices to be sparse along the interface. Moreover, the Wendland's function provides positive definite property for the matrix computation.

Apart from the transfer of data along the fluid-structure interface, the fluid mesh nodes inside the fluid domain can also be displaced based on the radial basis function mapping where the matrix $\boldsymbol{A}_{\mathrm{fs}}$ is constructed based on the volumetric nodes of the fluid domain rather than just the fluid-structure interface carried out previously, i.e., the target nodes now contain the volumetric data of the fluid domain.

7.2.1.3 Convergence of RBF Mapping: Static Load Data Transfer

In this section, we carry out a systematic convergence analysis of the radial basis function mapping approach described in the previous section to transfer data across the fluid-structure interface. To accomplish this, we consider a semi-circular surface as the fluid-structure interface with varying discretization on the fluid and the structural sides of the interface as shown in Fig. 7.1. In the schematic, the outer domain consists of fluid (Ω^{f}) and the inner domain is the structure (Ω^{s}). A fluid traction acts on the fluid side of the fluid-structure interface Γ^{fs} as
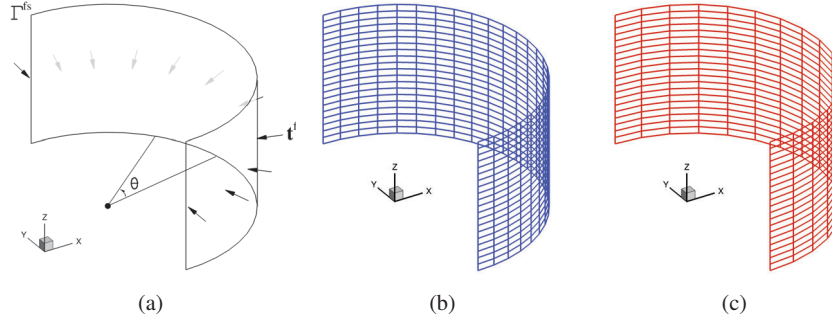
Fig. 7.1 Convergence test for radial basis function mapping: (a) Schematic of the traction transfer from the fluid to the structural meshes along Γ^{fs}, (b) fluid and (c) structural meshes for the case $A^{\mathrm{f}}/A^{\mathrm{s}} = 0.67$ and $n_c^{\mathrm{s}} = 16$.

$$\mathbf{t}^{\mathrm{f}} = \mathbf{t}^{\mathrm{f}}(\theta, z) = -\left(\frac{1}{2}\rho^{\mathrm{f}}U_\infty^2(1 - 4\sin^2\theta) + \rho^{\mathrm{f}}gz\right)\begin{pmatrix}0.5\cos\theta\\ 0.5\sin\theta\\ 0\end{pmatrix}, \qquad (7.18)$$

where $\rho^{\mathrm{f}} = 1000 \text{ kg/m}^3$, $U_\infty = 1.0 \text{ m/s}$, $g = 9.81 \text{ m/s}^2$, z is the Z-coordinate and $\theta \in [-\pi/2, \pi/2]$ is the angle shown in Fig. 7.1(a). This prescribed load represents the static pressure along the Z-direction as a result of potential flow around a cylinder. We only consider the downstream half of the cylinder for the convergence study. The support radius r for the radial basis function is selected as 2.

We employ two ratios of mismatch between the fluid and the structural meshes. The discretization in the Z-direction is kept constant at the number of elements of $n_z^{\mathrm{f}} = n_z^{\mathrm{s}} = 20$. The number of elements along the circumference of the semi-circle is varied on the fluid (n_c^{f}) as well as structural (n_c^{s}) meshes. The element area can thus be written as $A^{\mathrm{f}} = \pi R z/(n_c^{\mathrm{f}} n_z^{\mathrm{f}})$ and $A^{\mathrm{s}} = \pi R z/(n_c^{\mathrm{s}} n_z^{\mathrm{s}})$, where $R = 1$ and $z = 1$ are the radius and height of the semi-circular cylinder. The refinement is carried out such that the area mismatch is $A^{\mathrm{f}}/A^{\mathrm{s}} \in [0.67, 2]$. The refinement degree of the structural mesh is $n_c^{\mathrm{s}} \in [16, 32, 64, 128, 256]$ which is kept equivalent for the two cases of mismatch considered. The different meshes on the fluid and structural sides at Γ^{fs} are shown in Figs. 7.1(b) and (c) for $A^{\mathrm{f}}/A^{\mathrm{s}} = 0.67$ and $n_c^{\mathrm{s}} = 16$.

The interpolated traction values at the structural nodes are shown for the representative case of $A^{\mathrm{f}}/A^{\mathrm{s}} = 0.67$ and $n_c^{\mathrm{s}} = 16$ in Fig. 7.2. The relative error in the interpolation is quantified as

$$e_{\mathrm{r}} = \frac{|\mathbf{t}^{\mathrm{s}} - \mathbf{t}^{\mathrm{s}}(\theta, z)|}{|\mathbf{t}^{\mathrm{s}}(\theta, z)|}, \qquad (7.19)$$

where $\mathbf{t}^{\mathrm{s}}$ is the interpolated traction values at the structural nodes and $\mathbf{t}^{\mathrm{s}}(\theta, z)$ is the exact value at the corresponding nodes based on Eq. (7.18). The contour of the relative error is shown in Fig. 7.2 (right) for the structural mesh. It is observed that the error is less than 1.5% for the cases considered. We also quantify the convergence
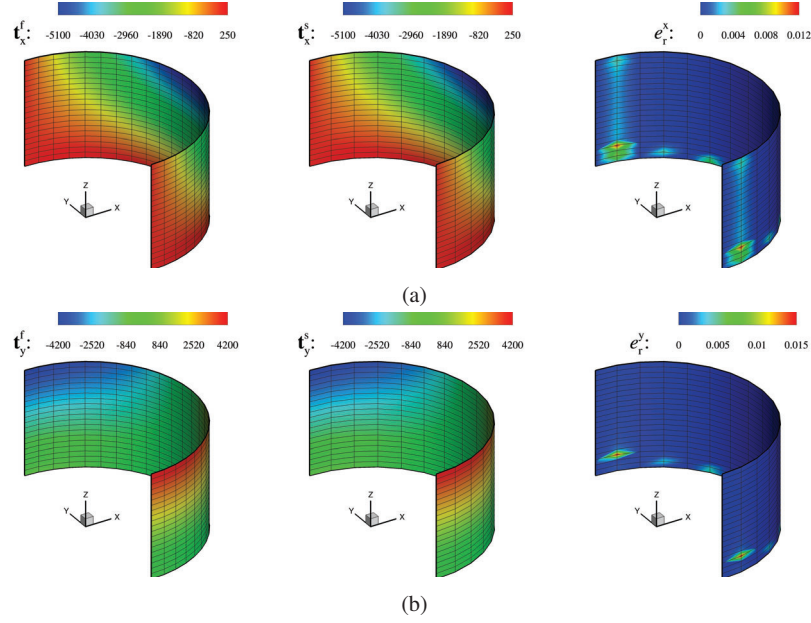
Fig. 7.2 Comparison of interpolation via radial basis function mapping for $A^f/A^s = 0.67$ and $n_c^s = 16$ for the fluid (left) and structural (middle) meshes for traction in (a) X-direction, and (b) Y-direction. The relative error of the traction values are also shown for the structural mesh (right).
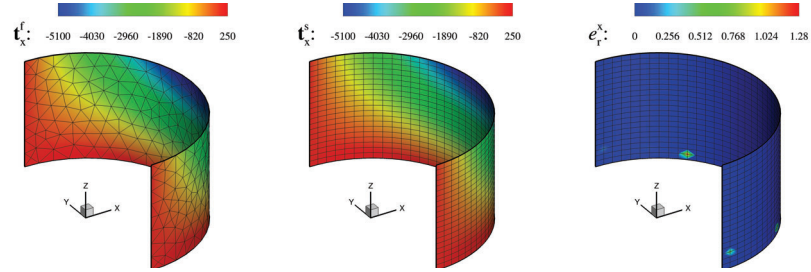

Fig. 7.3 Comparison of interpolation via radial basis function mapping for $A^f/A^s = 2$ with unstructured triangular mesh for the fluid (left) and structured quadrilateral mesh for the solid (middle) for traction in X-direction when $n_z^s = 20$ and $n_c^s = 40$. The relative error of the traction values are also shown for the structural mesh (right).

of the RBF interpolation by evaluating the error in the transfer of the traction as

$$e_1 = \frac{||\mathbf{t}^s - \mathbf{t}^s(\boldsymbol{\theta}, z)||_2}{||\mathbf{t}^s(\boldsymbol{\theta}, z)||_2}, \tag{7.20}$$

The behavior of the error with mesh refinement has been plotted in Fig. 7.4(a) where convergence of order close to 3 is observed which is consistent with the Wendland's

C^2 function interpolation. Note that in this case, $h = A^s$ as the number of elements in the Z-direction is constant.
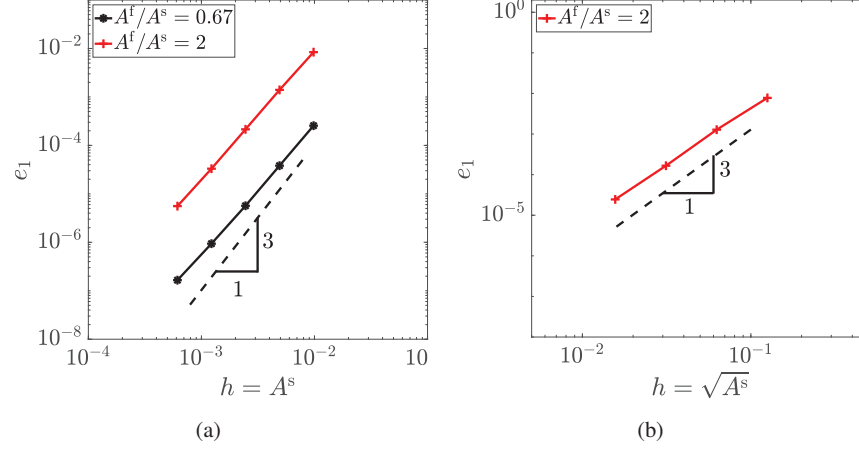
Fig. 7.4 Error convergence for the radial basis function interpolation method for varying mesh mismatch on the fluid and structural sides of the fluid-structural interface for (a) structured grid, and (b) unstructured grid with different shapes.

A further analysis is carried out to quantify the error for unstructured non-matching meshes across the fluid and structural domains at the interface consisting of different shapes such as triangular mesh on the fluid and quadrilateral on the structural side. In this case, the number of elements in the structural mesh $n_z^s \in [10, 20, 40, 80]$ and $n_c^s \in [20, 40, 80, 160]$ such that $A^f/A^s = 2$. As the element size is varying in both the directions, the element size is defined as $h = \sqrt{A^s}$. The convergence for the unstructured meshes across the interface is shown in Fig. 7.4(b) where a third order of convergence is observed, as expected. The interpolation data is shown in Fig. 7.3 for the representative mesh with $n_z^s = 20$ and $n_c^s = 40$.

The error convergence study for the RBF interpolation technique shows a higher order of convergence and independence of the mesh connectivity, emphasizing its generality for scattered data interpolation and efficiency for fluid-structure interaction problems.

7.2.2 Point-to-Element Projection

We next discuss about the second category of spatial coupling technique, which is point-to-element projection. Two types of point-to-element projection schemes are commonly used for FSI problems, viz., (a) Node projection, and (b) Quadrature projection.

7.2.2.1 Nodal Projection

At the fluid structure interface Γ, the kinematic equilibrium conditions impose that $\boldsymbol{u}^{\mathrm{f}} = \boldsymbol{u}^{\mathrm{s}}$. Based on the property of the shape functions for the fluid and structural subdomains, the displacement of the fluid nodes at Γ at the nodes can be expressed as

$$\tilde{\boldsymbol{u}}_j^{\mathrm{f}} = \sum_{i=1}^{m^{\mathrm{s}}} c_{ji} \tilde{\boldsymbol{u}}_i^{\mathrm{s}}, \tag{7.21}$$

where $\tilde{\boldsymbol{u}}_j^{\mathrm{f}}$ is the discrete value of the displacement of the fluid node j, c_{ji} is an approximation matrix based on the shape functions of the discretization and m^{s} is the number of structural nodes on the interface. Let the virtual displacement of the fluid nodes be given by

$$\tilde{\boldsymbol{u}}^{\mathrm{f}} = \sum_{j=1}^{m^{\mathrm{f}}} D_j \tilde{\boldsymbol{u}}_j^{\mathrm{f}}, \tag{7.22}$$

where m^{f} is the number of fluid nodes and D_j is some interpolatory function of the discrete values $\tilde{\boldsymbol{u}}_j^{\mathrm{f}}$. Therefore, the virtual work for the fluid tractions can be written as

$$\delta W^{\mathrm{f}} = \int_{\Gamma^{\mathrm{f}}} \boldsymbol{t}^{\mathrm{f}} \tilde{\boldsymbol{u}}^{\mathrm{f}} d\Gamma = \sum_{j=1}^{m^{\mathrm{f}}} \int_{\Gamma^{\mathrm{f}}} \boldsymbol{t}^{\mathrm{f}} (D_j \tilde{\boldsymbol{u}}_j^{\mathrm{f}}) d\Gamma = \sum_{j=1}^{m^{\mathrm{f}}} \boldsymbol{F}_j^{\mathrm{f}} \tilde{\boldsymbol{u}}_j^{\mathrm{f}}, \tag{7.23}$$

where $\boldsymbol{F}_j^{\mathrm{f}} = \int_{\Gamma^{\mathrm{f}}} \boldsymbol{t}^{\mathrm{f}} D_j d\Gamma$. From Eq. (7.21),

$$\delta W^{\mathrm{f}} = \sum_{j=1}^{m^{\mathrm{f}}} \boldsymbol{F}_j^{\mathrm{f}} \sum_{i=1}^{m^{\mathrm{s}}} c_{ji} \tilde{\boldsymbol{u}}_i^{\mathrm{s}} = \sum_{i=1}^{m^{\mathrm{s}}} \left(\sum_{j=1}^{m^{\mathrm{f}}} \boldsymbol{F}_j^{\mathrm{f}} c_{ji} \right) \tilde{\boldsymbol{u}}_i^{\mathrm{s}} = \sum_{i=1}^{m^{\mathrm{s}}} \boldsymbol{F}_i^{\mathrm{s}} \tilde{\boldsymbol{u}}_i^{\mathrm{s}} = \delta W^{\mathrm{s}}, \tag{7.24}$$

where $\boldsymbol{F}_i^{\mathrm{s}} = \sum_{j=1}^{m^{\mathrm{f}}} \boldsymbol{F}_j^{\mathrm{f}} c_{ji}$ is the structural force.

The nodal projection scheme consists of the following steps [62]:

1. Pair each fluid mesh point S_j on Γ^{f} with the closest structural element Ω_e^{s} on Γ^{s}
2. Find the natural coordinates of the projection χ_j on the structural element of the fluid point S_j
3. Interpolate the structural displacement at the projected point to obtain the fluid displacement using the shape functions of the structural discretization, i.e.,

$$\tilde{\boldsymbol{u}}_j^{\mathrm{f}} = \tilde{\boldsymbol{u}}^{\mathrm{f}}(S_j) = \tilde{\boldsymbol{u}}^{\mathrm{s}}(\chi_j) = \sum_{i=1}^{i_e} N_i^{\mathrm{s}}(\chi_j) \tilde{\boldsymbol{u}}_{S_j}^{\mathrm{s}}, \tag{7.25}$$

i_e being the number of element nodes in the structural element.

Comparing Eqs. (7.21) and (7.25), $c_{ji} = N_i(\boldsymbol{\chi}_j)$. Therefore,

$$\boldsymbol{F}_i^s = \sum_{j=1}^{m^f} \boldsymbol{F}_j^f N_i^s(\boldsymbol{\chi}_j). \tag{7.26}$$

Hence, with the knowledge of the load vectors at the node points of the fluid interface, the loads on the structural points can be interpolated by projecting the fluid node to the structural interface.
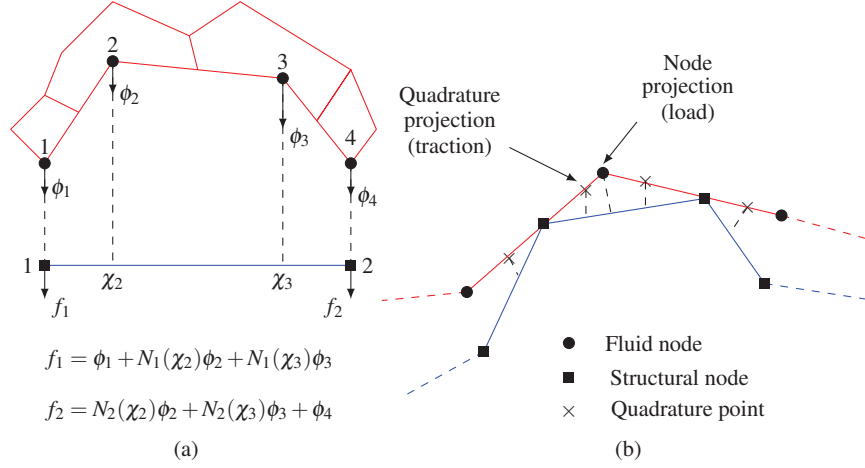

$$f_1 = \phi_1 + N_1(\chi_2)\phi_2 + N_1(\chi_3)\phi_3$$

$$f_2 = N_2(\chi_2)\phi_2 + N_2(\chi_3)\phi_3 + \phi_4$$

(a)   (b)

Fig. 7.5 (a) Nodal projection method, (b) Comparison of nodal and quadrature projection techniques.

7.2.2.2 Quadrature Projection

For obtaining an accurate estimate of the traction on the structural subdomain, our aim is to calculate $\tilde{t}_j^s$ for given $\tilde{t}_i^f$, N_i^f and N_j^s. We use the Galerkin weighted residual method for minimizing the residual $t^s - t^f$ to get the required approximation for load vector on the structural interface. Multiplying by N_i^s on both sides of the residual and integrating over the interface boundary, we get

$$\int_\Gamma N_i^s t^s \mathrm{d}\Gamma = \int_{\Gamma^{fs}} N_i^s t^f \mathrm{d}\Gamma. \tag{7.27}$$

Using Eq. (7.1),

$$\int_\Gamma N_i^s N_j^s \tilde{t}_j^s \mathrm{d}\Gamma = \int_\Gamma N_i^s N_j^f \tilde{t}_j^f \mathrm{d}\Gamma \tag{7.28}$$

The tractions on the structural mesh is thus given as

$$\tilde{t}_k^{\mathrm{s}} = \left[M_{ki}^{\mathrm{s}} \right]^{-1} \left\{ f_i^{\mathrm{s}} \right\}, \tag{7.29}$$

where

$$\left[M_{ki}^{\mathrm{s}} \right] = \int_{\Gamma} N_i^{\mathrm{s}} N_k^{\mathrm{s}} d\Gamma, \qquad \left\{ f_i^{\mathrm{s}} \right\} = \int_{\Gamma} N_i^{\mathrm{s}} N_j^{\mathrm{f}} \tilde{t}_j^{\mathrm{f}} d\Gamma. \tag{7.30}$$

Therefore, for evaluating the traction on the fluid-structure interface for the structural equation, the above mass matrix and the force vector needs to be evaluated which consists of the shape functions of both the structural and fluid subdomains. For matching meshes across Γ, this operation is straight forward. However, for non-matching meshes, the inconsistency in the shape functions can lead to integrations across discontinuities.

The challenge here is to evaluate f_i^{s} across non-matching meshes at Γ. There are two ways of obtaining the expression via quadrature projection from the fluid to structure interface [40]:

1. Loop over structural elements and introduce quadrature points in each element. The vector is then given by

$$\left\{ f_i^{\mathrm{s}} \right\} = \sum_{i=1}^{m_{\mathrm{el}}^{\mathrm{s}}} \sum_{g=1}^{ngp} N_i^{\mathrm{s}}(\chi_g^{\mathrm{s}}) \det(\boldsymbol{J}) w(g) N_j^{\mathrm{f}} \tilde{t}_j^{\mathrm{f}}(\chi_g^{\mathrm{s}}), \tag{7.31}$$

   where $m_{\mathrm{el}}^{\mathrm{s}}$ is the number of structural elements, ngp is the number of Gauss quadrature points on an element, $\boldsymbol{J}$ is the Jacobian of the transformation from global to natural coordinates, $w(g)$ is the Gauss weights at point χ_g^{s}. Here, the structural shape functions are known at the quadrature points and the fluid traction is interpolated at these points. This scheme is not conservative because there can be some fluid elements without any quadrature points.

2. Loop over fluid elements and introduce quadrature points in each element. In this case, the vector is

$$\left\{ f_i^{\mathrm{s}} \right\} = \sum_{i=1}^{m_{\mathrm{el}}^{\mathrm{f}}} \sum_{g=1}^{ngp} N_i^{\mathrm{s}}(\chi_g^{\mathrm{f}}) \det(\boldsymbol{J}) w(g) N_j^{\mathrm{f}} \tilde{t}_j^{\mathrm{f}}(\chi_g^{\mathrm{f}}), \tag{7.32}$$

   where $m_{\mathrm{el}}^{\mathrm{f}}$ is the number of fluid elements at the fluid-structure interface. In this technique, the shape functions on the structural interface are evaluated by using optimized searching algorithms to find out the corresponding structural element of the fluid traction Gauss quadrature points χ_g^{f}. The looping over all the fluid elements ensures that the fluid traction is transferred completely to the structural interface, thus maintaining the conservation property. However, some structural nodes may not receive traction in doing so. Therefore, sometimes it is essential to

either take higher order Gauss integration or recursively divide the fluid element so that all the structural nodes receive traction.

7.2.3 Common-Refinement Projection

Both the nodal and quadrature projection schemes are conservative but do not satisfy the traction continuity due to inaccurate transfer of loads from the fluid to the structural subdomain. Therefore, such schemes lead to local errors for non-matching meshes [109].
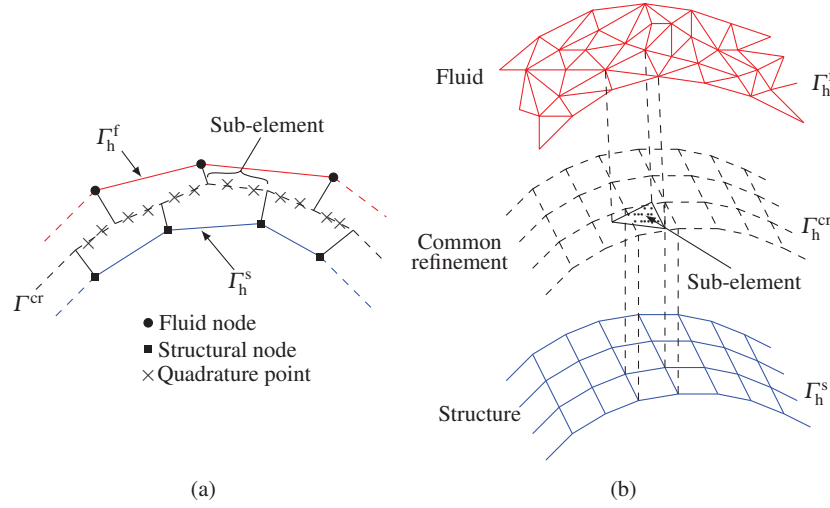

Fig. 7.6 Common-refinement method for load projection in (a) 2D and (b) 3D.

The common-refinement projection is a special data structure for transferring data between non-matching meshes with varying degree of mismatch. We construct a common-refinement surface between the fluid and structural boundaries at Γ. It consists of polygons that subdivide the input boundary meshes of the structure and fluid subdomains simultaneously. Each sub-element of a common-refinement mesh has two geometrical realizations, in general, which are different but must be close to each other to obtain a physically consistent data transfer. The topology of the common-refinement sub-elements are defined by the intersection of the surface elements of the input meshes. In this technique, the load vector defined in Eq. (7.30) is given by

$$\left\{ f_i^{\mathrm{s}} \right\} = \sum_{j=1}^{n_{\mathrm{el}}^{\mathrm{cr}}} \sum_{g=1}^{ngp} N_i^{\mathrm{s}}(\boldsymbol{\chi}_g^{\mathrm{cr}}) \det(\boldsymbol{J}) w(g) N_j^{\mathrm{f}} \tilde{\boldsymbol{t}}_j^{\mathrm{f}}(\boldsymbol{\chi}_g^{\mathrm{cr}}), \qquad (7.33)$$

(a)

(b)
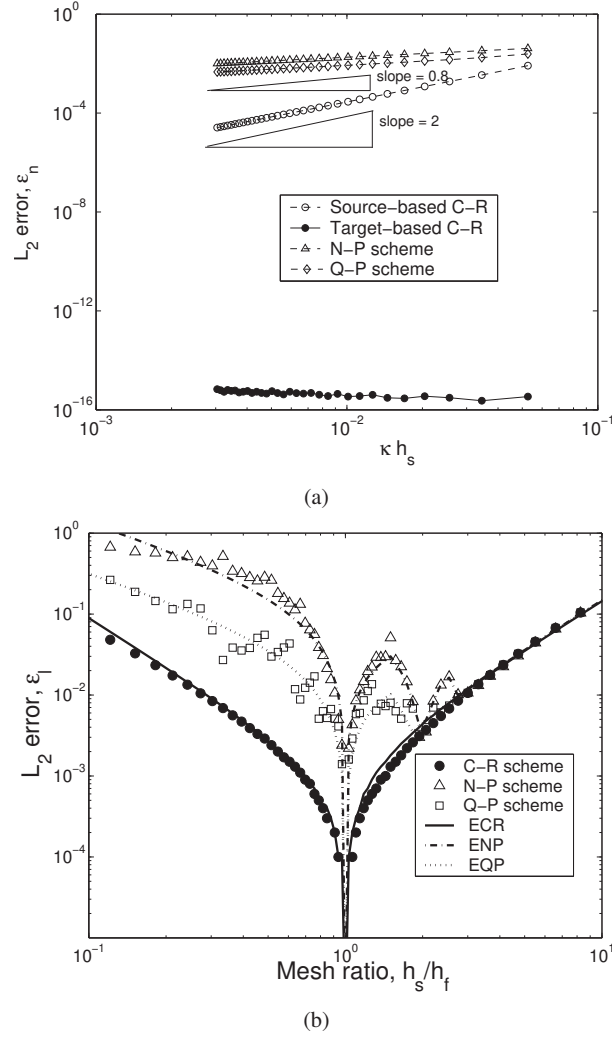
Fig. 7.7 Error assessment for the common-refinement scheme: (a) accuracy of load transfer schemes in L_2 norm error ε_n from analytical solution, and (b) dependence of load vector error on relative mesh ratio h_s/h_f for the load transfer schemes.

where n_{el}^{cr} is the number of sub-elements in the common-refinement interface and χ_g^{cr} is the quadrature projection of the common-refinement points on the structural interface. More details about this projection can be found in [106]. The error analyses for load transfer across a static circular arc, conducted in [106] shows an optimal convergence for source-based common-refinement and exact transfer for target-based common-refinement scheme (Fig. 7.7(a)). Furthermore, the grid mismatch study showed that the common-refinement scheme performed within the interpolant error

for all the cases considered (Fig. 7.7(b)), while the errors depended strongly on the grid mismatch for the nodal and quadrature projection schemes.

7.3 Temporal Coupling Techniques

In the previous section, we discussed the various types of spatial coupling techniques at the fluid-structure interface for accurate and stable transfer of forces and displacements. Next, we focus on the temporal coupling where the sequence of the data transfer at the interface across the partitioned subdomains is discussed. These can be classified into (a) loosely coupled, and (b) strongly coupled schemes. They are discussed in the following subsections.

7.3.1 Staggered Loosely Coupled Techniques

Loosely coupled techniques consist of explicit time integration of the fluid-structure interface data transfer. They are straightforward and easy to implement and are very computationally efficient. Here, we discuss conventional sequential staggered, generalized serial staggered and combined interface boundary condition methods.

7.3.1.1 Conventional Sequential Staggered Method

The most popular temporal coupling scheme is called the conventional sequential staggered (CSS) scheme shown in Fig. 7.8. The algorithm consists of the following steps: For each $t \in [t^n, t^{n+1}]$,

1. Solve structural equation using the known traction $t^{s,n}$ to obtain the structural velocity $v^{s,n+1}$
2. Apply kinematic equilibrium condition at the interface by imposing structural motion

$$v^{f,n+1} = (1 - \alpha)v^{s,n+1} + \alpha v^{s,n}, \text{ on } \Gamma, \text{ where } \alpha \in [0,1] \qquad (7.34)$$

3. Set $\dot{u}^{f,n+1} = v^{f,n+1}$ and update the fluid mesh displacements and solve the ALE fluid equations for updated values of velocity and pressure
4. Extract new interface traction $t^{f,n+1}$ and satisfy dynamic equilibrium at the interface

$$t^{s,n+1} = (1 - \beta)t^{f,n+1} + \beta t^{f,n}, \text{ on } \Gamma, \text{ where } \beta \in [0,1] \qquad (7.35)$$

In the algorithm, α and β are the weighting parameters to interpolate the structural velocity and the fluid tractions respectively between the time interval t^n and t^{n+1}. When $\alpha = \beta = 1$, the solution at the previous time step is transferred to the respective subdomains, given a method that is called parallel conventional staggered method [64] as the fluid and structural subdomains can start their computations at the same time level and perform their inner subdomain integration in a parallel way. Figure 7.8 refers to the case when $\alpha = \beta = 0$.

The CSS scheme may suffer significantly from destabilizing effects introduced through the interface discretization. High nonlinearity in the problem can make the one-sided approximation inaccurate. More precisely, the numerical treatment of boundary conditions create inconsistencies in omitting and retaining some terms on the neighbouring discrete space and time slabs along the interface. Depending on the direction of the interface acceleration, high under- or over-prediction of pressure may occur due to lack of energy equilibrium across the fluid-structure interface. In other words, any small error in the interface displacements imposed onto the fluid by the structure may result in large errors in the fluid pressure. In general, due to a time lag between the structural and fluid subdomains, the CSS technique is at most first-order energy accurate due to $\mathcal{O}(\Delta t)$ in time on Γ.
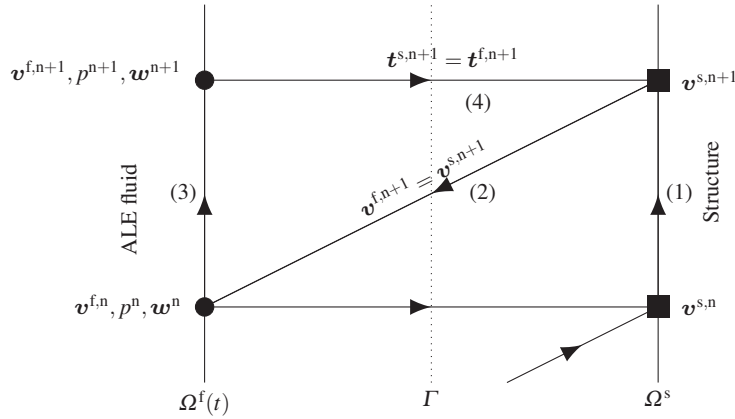
Fig. 7.8 Conventional sequential staggered (CSS) scheme for $\alpha = \beta = 0$.

7.3.1.2 Generalized Serial Staggered Method

The temporal accuracy of the scheme can be improved by applying a structural prediction step based on the higher-order interface velocity extrapolation and momentum averaging. It consists of the following steps: For each $t \in [t^n, t^{n+1}]$,

1. Solve structural equation using the known traction at interface $t^{I,n}$ to obtain the structural velocity $v^{s,n+1}$

2. Apply kinematic equilibrium condition at the interface by predicting interface velocity

$$v^{\mathrm{I},\mathrm{n}+1} = v^{\mathrm{s},\mathrm{n}} + \Delta t(\alpha_0 \dot{v}^{\mathrm{s},\mathrm{n}} - \alpha_1 \dot{v}^{\mathrm{s},\mathrm{n}-1}), \text{ on } \Gamma \qquad (7.36)$$

3. Set $\dot{u}^{\mathrm{f},\mathrm{n}+1} = v^{\mathrm{I},\mathrm{n}+1}$ and update the fluid mesh displacements and solve the ALE fluid equations for updated values of velocity and pressure
4. Extract new interface traction $t^{\mathrm{f},\mathrm{n}+1}$ and satisfy dynamic equilibrium at the interface

$$t^{\mathrm{I},\mathrm{n}+1} = (1 - \beta)t^{\mathrm{f},\mathrm{n}+1} + \beta t^{\mathrm{f},\mathrm{n}}, \text{ on } \Gamma, \text{ where } \beta \in [0,1] \qquad (7.37)$$

In the GSS algorithm, $\alpha_0 = 3/2$ and $\alpha_1 = 1/2$ are required for second-order accuracy in the satisfaction of the kinematic condition and $\beta = 1/2$ for the improved momentum or load averaging.

7.3.1.3 Combined Interface Boundary Condition Method

In the temporal coupling techniques discussed in the previous subsections, the governing equations of each subdomain have no direct influence along the equilibrium conditions satisfied at the fluid-structure interface, which are enforced sequentially with a time lag. In the combined interface boundary condition (CIBC) technique, the interface solution is influenced explicitly by the neighbouring subdomains. The approach achieves improved precision and numerical stability by solving the transformed conditions for the interface quantities based on their spatial and temporal derivatives [181].

The combined residual operators for the kinematic and dynamic equilibrium conditions can be constructed as

$$\mathscr{R}^{D,N}\left(\rho^{\mathrm{f}}\frac{\partial v^{\mathrm{s}}}{\partial t}, \frac{\partial t^{\mathrm{s}}}{\partial t}, \frac{\partial t^{\mathrm{f}}}{\partial t}, \frac{\partial t^{\mathrm{f}}}{\partial n}\right) = \mathbf{0}, \text{ along } \Gamma, \qquad (7.38)$$

where ρ^{f} is the density of the fluid, $\partial/\partial t$ and $\partial/\partial n$ denote the time derivative and normal spatial derivative of the interface quantities respectively. The idea relies on constructing a local discrete energy-preserving property for the staggered stencil between the pair of differential equations. Based on the current solutions on both sides of the interface, these operators calculate successive corrections to the staggered solutions on Γ.

The conventional kinematic and dynamic equilibrium conditions can be transformed into

$$\frac{\partial t^{\mathrm{f}}}{\partial n^{\mathrm{f}}} = \rho^{\mathrm{f}}\frac{\partial v^{\mathrm{s}}}{\partial t}, \qquad\qquad \text{on } \Gamma, \qquad (7.39)$$

$$\frac{\partial t^{\mathrm{s}}}{\partial t} \cdot n^{\mathrm{s}} = \frac{\partial t^{\mathrm{f}}}{\partial t} \cdot n^{\mathrm{f}}, \qquad\qquad \text{on } \Gamma. \qquad (7.40)$$

Combining the above equations and using the fact that $n^{\mathrm{f}} = -n^{\mathrm{s}}$, the relation for the structural velocity at the interface and the fluid traction are obtained as

$$\rho^{\mathrm{f}}\frac{\partial v^{\mathrm{s}}}{\partial t} + \omega\frac{\partial t^{\mathrm{s}}}{\partial t} = \frac{\partial t^{\mathrm{f}}}{\partial n^{\mathrm{f}}} - \omega\frac{\partial t^{\mathrm{f}}}{\partial t}, \qquad\qquad \text{on } \Gamma^{\mathrm{s}}, \qquad (7.41)$$

$$\frac{\partial t^{\mathrm{f}}}{\partial n^{\mathrm{f}}} + \omega\frac{\partial t^{\mathrm{f}}}{\partial t} = \rho^{\mathrm{f}}\frac{\partial v^{\mathrm{s}}}{\partial t} - \omega\frac{\partial t^{\mathrm{s}}}{\partial t}, \qquad\qquad \text{on } \Gamma^{\mathrm{f}}, \qquad (7.42)$$

where ω is a positive dimensional parameter and small enough to ensure that the interface energy is always stable [106]. It provides appropriate combination of the applied traction forces with the appropriate corrections into the interfacial acceleration.

The above relationships can be written in the explicit staggered form as

$$\rho^{\mathrm{f},\mathrm{n}}\left(\frac{\partial v^{\mathrm{s}}}{\partial t}\right)^{\mathrm{n}} = \left(\frac{\partial t^{\mathrm{f}}}{\partial n^{\mathrm{f}}}\right)^{\mathrm{n}} - \omega\left[\left(\frac{\partial t^{\mathrm{f}}}{\partial t}\right)^{\mathrm{n}} - \left(\frac{\partial t^{\mathrm{s}}}{\partial t}\right)^{\mathrm{n}}\right], \qquad\qquad \text{on } \Gamma^{\mathrm{s}},$$

$$(7.43)$$

$$\left(\frac{\partial t^{\mathrm{f}}}{\partial t}\right)^{\mathrm{n}+1} = -\left(\frac{\partial t^{\mathrm{s}}}{\partial t}\right)^{\mathrm{n}+1} + \frac{1}{\omega}\left[\left(\rho^{\mathrm{f}}\frac{\partial v^{\mathrm{s}}}{\partial t}\right)^{\mathrm{n}+1} - \left(\frac{\partial t^{\mathrm{f}}}{\partial n^{\mathrm{f}}}\right)^{\mathrm{n}+1}\right], \qquad \text{on } \Gamma^{\mathrm{f}}.$$

$$(7.44)$$

The above equations provide the corrections for the velocity and tractions at the fluid-structure interface. Instead of applying the equilibrium conditions directly, we apply a corrected velocity and traction at Γ as

$$v^{\mathrm{f},\mathrm{n}+1} = v^{\mathrm{s},\mathrm{n}+1} + \delta v_*^{\mathrm{n}}, \qquad\qquad \text{on } \Gamma^{\mathrm{s}}, \qquad (7.45)$$

$$t^{\mathrm{s},\mathrm{n}+1} = t^{\mathrm{f},\mathrm{n}+1} + \delta t_*^{\mathrm{n}+1}, \qquad\qquad \text{on } \Gamma^{\mathrm{f}}, \qquad (7.46)$$

where the corrections are given by

$$\delta v_*^{\mathrm{n}} = \frac{\Delta t}{\rho^{\mathrm{f}}}\left[\left(\frac{\partial t^{\mathrm{f}}}{\partial n^{\mathrm{f}}}\right)^{\mathrm{n}} - \omega\left\{\left(\frac{\partial t^{\mathrm{f}}}{\partial t}\right)^{\mathrm{n}} - \left(\frac{\partial t^{\mathrm{s}}}{\partial t}\right)^{\mathrm{n}}\right\}\right], \qquad\qquad \text{on } \Gamma^{\mathrm{s}},$$

$$(7.47)$$

$$\delta t_*^{\mathrm{n}+1} = \Delta t\left[-\left(\frac{\partial t^{\mathrm{s}}}{\partial t}\right)^{\mathrm{n}+1} + \frac{1}{\omega}\left\{\left(\rho^{\mathrm{f}}\frac{\partial v^{\mathrm{s}}}{\partial t}\right)^{\mathrm{n}+1} - \left(\frac{\partial t^{\mathrm{f}}}{\partial n^{\mathrm{f}}}\right)^{\mathrm{n}+1}\right\}\right], \qquad \text{on } \Gamma^{\mathrm{f}}.$$

$$(7.48)$$

At each time step, the prediction of the displacement and the correction of tractions are formed in a sequential manner. The algorithm for CIBC consists of the following steps: For each $t \in [t^{\mathrm{n}}, t^{\mathrm{n}+1}]$,

1. Solve structural equation using the known traction at interface $t^{\mathrm{s},\mathrm{n}}$ to obtain the structural velocity $v^{\mathrm{s},\mathrm{n}+1}$
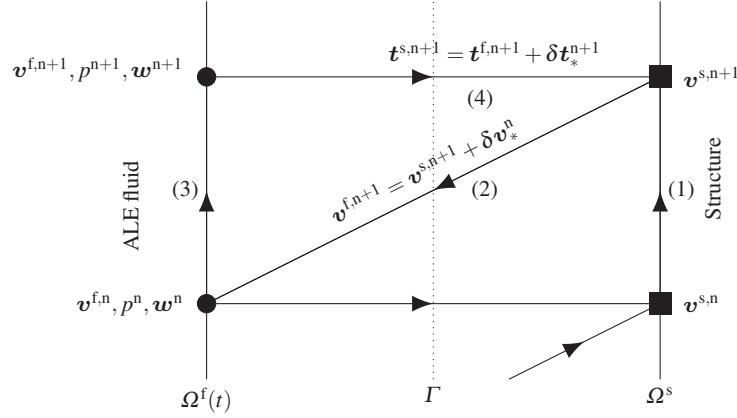
Fig. 7.9 Combined interface boundary condition (CIBC) scheme.

2. Solve for the velocity prediction δv_*^n given in Eq. (7.47) and apply kinematic equilibrium condition at the interface

$$v^{f,n+1} = v_*^{n+1} = v^{s,n+1} + \delta v_*^n \qquad (7.49)$$

3. Set $\dot{u}^{f,n+1} = v^{f,n+1}$ and update the fluid mesh displacements and solve the ALE fluid equations for updated values of velocity and pressure

4. Solve for the traction correction δt_*^{n+1} in Eq. (7.48) and satisfy dynamic equilibrium at the interface

$$t^{s,n+1} = t_*^{n+1} = t^{f,n+1} + \delta t_*^{n+1} \qquad (7.50)$$

Note that we only considered explicit corrections in the staggered algorithm. It can be extended to a semi-implicit predictor-corrector procedure by forming the structural velocity as predictor and traction as corrector. This forms the basis of the strongly coupled techniques which are discussed in the next subsection.

7.3.2 Strongly Coupled Techniques

In this section, we discuss the partitioned iterative coupling for the FSI system, which is considered to be a strongly coupled technique. We begin with the coupled linearized matrix form and discuss the quasi-Newton updates that are carried out to correct the fluid forces on the structure. Then, the algorithm for the coupling is presented for the block-type partitioned system.

Consider the decomposition of the set of degrees of freedom (DOFs) of the fluid-structure system into interior DOFs and the DOFs at the fluid-structure interface. With the help of Newton-Raphson linearization, the coupled fluid-structure system

in a partitioned format can be expressed as

$$
\begin{bmatrix}
\boldsymbol{A}^{ss} & \boldsymbol{0} & \boldsymbol{0} & \boldsymbol{A}^{Is} \\
\boldsymbol{A}^{sI} & \boldsymbol{I} & \boldsymbol{0} & \boldsymbol{0} \\
\boldsymbol{0} & \boldsymbol{A}^{If} & \boldsymbol{A}^{ff} & \boldsymbol{0} \\
\boldsymbol{0} & \boldsymbol{0} & \boldsymbol{A}^{fI} & \boldsymbol{I}
\end{bmatrix}
\begin{Bmatrix}
\Delta\boldsymbol{u}^{s} \\
\Delta\boldsymbol{u}^{I} \\
\Delta\boldsymbol{q}^{f} \\
\Delta\boldsymbol{f}^{I}
\end{Bmatrix}
=
\begin{Bmatrix}
\mathscr{R}^{s} \\
\mathscr{R}^{I}_{D} \\
\mathscr{R}^{f} \\
\mathscr{R}^{I}_{N}
\end{Bmatrix},
\tag{7.51}
$$

where $\Delta\boldsymbol{u}^{s}$ denotes the increment in the structural displacement, $\Delta\boldsymbol{u}^{I}$ and $\Delta\boldsymbol{f}^{I}$ represent the increments in the displacement and the forces along the fluid-structure interface. The increment in the unknowns associated with the fluid domain is denoted by $\Delta\boldsymbol{q}^{f} = (\Delta\boldsymbol{v}^{f}, \Delta p)$. On the right hand side, $\mathscr{R}^{s}$ and $\mathscr{R}^{f}$ represent the weighted residuals of the structural and stabilized flow equations respectively, whereas $\mathscr{R}^{I}_{D}$ and $\mathscr{R}^{I}_{N}$ denote the residuals corresponding to the imbalances during the enforcement of the kinematic (Dirichlet) condition (Eq. (3.96)) and the dynamic (Neumann) condition (Eq. (3.97)) at the fluid-structure interface respectively.

The block matrices on the left-hand side are described as follows. The matrix comprising of the mass, damping and stiffness matrices of the structural system for the non-interface structural DOFs is given by $\boldsymbol{A}^{ss}$. The transformation of the fluid forces at the interface to obtain the force vector for the structural system is denoted by $\boldsymbol{A}^{Is}$. The mapping of the structural displacements to the fluid-structure interface satisfying the kinematic condition is represented by $\boldsymbol{A}^{sI}$, where $\boldsymbol{I}$ is an identity matrix. $\boldsymbol{A}^{fI}$ denotes the transfer of the fluid forces to the fluid-structure interface satisfying the dynamic equilibrium condition and $\boldsymbol{A}^{If}$ is associated with the ALE mapping of the fluid spatial points. Finally, $\boldsymbol{A}^{ff}$ comprises of the transient, convection, diffusion and stabilization terms for the Navier-Stokes fluid system.

The idea behind the strong coupling procedure is to construct the cross-coupling between the fluid and the structure without forming the off-diagonal Jacobian term ($\boldsymbol{A}^{Is}$ in Eq. (7.51)) with the help of nonlinear iterations. This cross-coupling effect gives rise to force corrections at the interface resulting in what we call here nonlinear iterative force correction (NIFC) procedure. This correction relies on an input-output relationship between the structural displacement and the force transfer at each nonlinear iteration. This feedback process can be considered as a nonlinear generalization of the steepest descent method which transforms a divergent fixed-point iteration to a stable and convergent update of the approximate forces at the interface degrees of freedom [110]. Unlike the brute-force iterations in the strongly coupled FSI which lead to severe numerical instabilities for low structure-to-fluid mass ratios, the NIFC procedure provides a desired stability to the partitioned fluid-structure coupling, without the explicit evaluation of the off-diagonal Jacobian term. As derived in [110], the idea of partitioning is to eliminate the off-diagonal term $\boldsymbol{A}^{Is}$ to facilitate the staggered sequential updates for strongly coupled fluid-structure system. Through static condensation, Eq. (7.51) can be re-written as

$$
\begin{bmatrix} A^{ss} & 0 & 0 & 0 \\ A^{sI} & I & 0 & 0 \\ 0 & A^{If} & A^{ff} & 0 \\ 0 & 0 & 0 & A^{II} \end{bmatrix} \begin{Bmatrix} \Delta u^{s} \\ \Delta u^{I} \\ \Delta q^{f} \\ \Delta f^{I} \end{Bmatrix} = \begin{Bmatrix} \mathscr{R}^{s} \\ \mathscr{R}^{I}_{D} \\ \mathscr{R}^{f} \\ \widetilde{\mathscr{R}}^{I}_{N} \end{Bmatrix}. \tag{7.52}
$$

In the nonlinear interface force correction, we form the iterative scheme of the following matrix-vector product form

$$
\Delta f^{I} = \left(A^{II} \right)^{-1} \widetilde{\mathscr{R}}^{I}_{N}, \tag{7.53}
$$

where $\left(A^{II} \right)^{-1}$ is not constructed explicitly. Instead, the force correction vector Δf^{I} at the nonlinear iteration (subiteration) k can be constructed by successive matrix-vector products. This process essentially provides the control for the interface fluid force $f^{I} = \int_{\Gamma} \sigma^{f} \cdot n^{f} d\Gamma$ to stabilize strong fluid-structure interaction at low structure-to-fluid mass ratio. The scheme proceeds in a similar fashion as the predictor-corrector schemes by constructing the iterative interface force correction at each iteration. Let the error in the interface fluid force between the initial and first nonlinear iteration be $\Delta E^{I}_{(0)} = f^{I}_{(1)} - f^{I}_{(0)}$. Similarly, the force at the iteration $k+1$ is given by

$$
f^{I}_{(k+1)} = f^{I}_{(k)} + \Delta f^{I}_{(k)} = f^{I}_{(k)} + \left[\left(A^{II} \right)^{-1} \widetilde{\mathscr{R}}^{I}_{N} \right]_{(k)}. \tag{7.54}
$$

For the iterative correction of the fluid forces, a power method is considered for the above matrix problem. We assume an iteration matrix M which is diagonalizable in such a way that $M v_{(k)} = \lambda_{(k)} v_{(k)}$ for each k and eigenvalues $\lambda_{(k)}$ are distinct and nonzero with the corresponding eigenvectors $v_{(k)}$. The correction to the forces is then constructed with the aid of the error vector $\Delta E^{I}_{(0)}$ as

$$
f^{I}_{(k+1)} = f^{I}_{(k)} + M^{k} \Delta E^{I}_{(0)}, \tag{7.55}
$$

which can be written in terms of successive estimates as

$$
f^{I}_{(k+1)} = f^{I}_{(0)} + \sum_{i=0}^{k} M^{i} \Delta E^{I}_{(0)}, \quad \text{for } k = 1, 2, ... \tag{7.56}
$$

The error vectors $\Delta E^{I}_{(k)}$ can then be expressed in terms of the eigenvalues and eigenvectors λ and v respectively to obtain a sequence of transformation for the force vector $f^{I}_{(k+1)}$ similar to the Aitken's iterated Δ^{2} process [110].

This interface force correction can also be interpreted as a quasi-Newton update

$$
\Delta f^{I}_{(k+1)} = \Delta f^{I}_{(k)} + \Lambda_{(k)} \Delta E^{I}_{(0)}, \tag{7.57}
$$

where $\Delta f^{I}_{(k+1)} = f^{I}_{(k+1)} - f^{I}_{(k)}$, $\Delta f^{I}_{(k)} = f^{I}_{(k)} - f^{I}_{(k-1)}$ and $\Lambda_{(k)} = (M^{k} - M^{k-1})$ is an $n \times n$ matrix. There are three possible alternatives for the matrix $\Lambda_{(k)}$, namely,
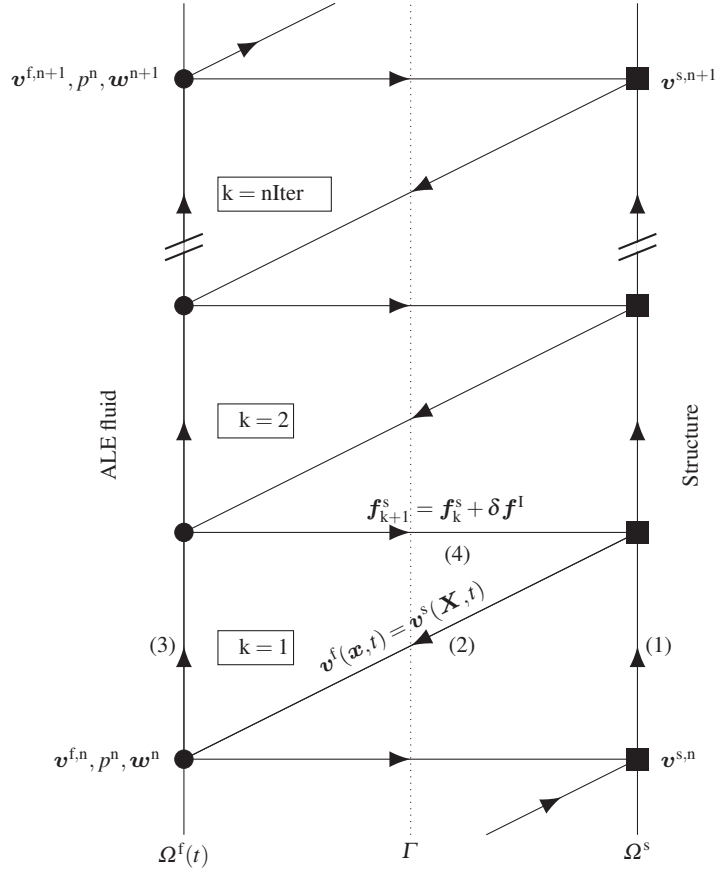
Fig. 7.10 Strong coupling with nonlinear iterative force correction for the fluid-structure system.

scalar, diagonal and full matrix. We consider $\Lambda_{(k)} = \alpha_{(k)}\mathbf{I}$ for the iterative quasi-Newton update, which can be considered as a minimal residual iteration method when $(\boldsymbol{y}, \Delta \boldsymbol{f}^{\mathrm{I}}_{(k+1)}) = 0$ for some $\boldsymbol{y}$, where $(\cdot, \cdot)$ denotes the standard inner product. Thus, we have

$$(\boldsymbol{y}, \Delta \boldsymbol{f}^{\mathrm{I}}_{(k+1)}) = (\boldsymbol{y}, \Delta \boldsymbol{f}^{\mathrm{I}}_{(k)}) + \alpha_{(k)}(\boldsymbol{y}, \Delta \boldsymbol{E}^{\mathrm{I}}_{(0)}) = 0, \tag{7.58}$$

$$\implies \alpha_{(k)} = -\frac{(\boldsymbol{y}, \Delta \boldsymbol{f}^{\mathrm{I}}_{(k)})}{(\boldsymbol{y}, \Delta \boldsymbol{E}^{\mathrm{I}}_{(0)})}. \tag{7.59}$$

It can be observed that the choice of $\boldsymbol{y} = \Delta \boldsymbol{E}^{\mathrm{I}}_{(0)}$ minimizes $||\Delta \boldsymbol{f}^{\mathrm{I}}_{(k+1)}||$ and this type of iterative procedure is similar to the minimal residual method [32, 31].

The algorithm for the NIFC scheme, shown in Fig. 7.10 can be summarized as follows: In a typical nonlinear iteration k,

1. Solve structural equation using the known traction at interface $\boldsymbol{f}_{(k)}^{s,n}$ to obtain the structural velocity $\boldsymbol{v}_{(k+1)}^{s,n+1}$

2. Apply kinematic equilibrium condition and the ALE compatibility condition at the interface. This is accomplished as follows:

- Mesh displacement $\boldsymbol{u}_{(k+1)}^{m,n+1}$ is equated to structural displacement as

$$\boldsymbol{u}_{(k+1)}^{m,n+1} = \boldsymbol{u}_{(k+1)}^{s,n+1} \text{ on } \Gamma \tag{7.60}$$

- Conservation property between moving elements in the fluid domain is satisfied by equating fluid velocity to mesh velocity as

$$\boldsymbol{v}_{(k+1)}^{f,n+\alpha^f} = \boldsymbol{w}_{(k+1)}^{n+\alpha^f} \text{ on } \Gamma, \tag{7.61}$$

where

$$\boldsymbol{w}_{(k+1)}^{n+\alpha^f} = \frac{\boldsymbol{u}_{(k+1)}^{m,n+1} - \boldsymbol{u}_{(k+1)}^{m,n}}{\Delta t} = \boldsymbol{v}_{(k+1)}^{s,n+\alpha^s} \text{ on } \Gamma \tag{7.62}$$

3. Evaluate the mesh velocity of spatial points and solve for ALE fluid equation to get updated velocity $\boldsymbol{v}_{(k+1)}^{f,n+1}$ and pressure $p_{(k+1)}^{n+1}$

4. Compute the updated hydrodynamic forces on the interface Γ and apply the NIFC force correction, thus satisfying the dynamic equilibrium as

$$\boldsymbol{f}_{(k+1)}^{s,n+\alpha^s} = \boldsymbol{f}_{(k+1)}^{I} = \boldsymbol{f}_{(k)}^{I} + \Delta \boldsymbol{f}_{(k)}^{I} \tag{7.63}$$

This concludes the description about the strongly coupled partitioned iterative techniques, where we have discussed one type of method known as nonlinear iterative force correction (NIFC). Next, we consider the common-refinement projection for the spatial coupling and the NIFC algorithm for the strong temporal coupling and assess the scheme by performing numerical tests on benchmark problems and then demonstrate the partitioned framework for a practical application.

7.4 Common-Refinement Projection with Nonlinear Iterative Force Correction

In this section, we investigate the effectiveness and accuracy of the common-refinement projection scheme along with the nonlinear iterative force correction scheme in the partitioned coupling between the fluid and the structural domains. The scheme is then applied to validate a problem of three-dimensional FSI consisting of non-matching meshes across the two fluid and structural domains. Finally, the partitioned coupling is demonstrated for a flow across an offshore riser.

7.4.1 Error Analysis and Convergence Study

A typical FSI simulation deals with an intact interface between the fluid and the structural domains without any gaps or overlaps. At the fluid-structure interface, the fluid forces are transferred to the structural surface and the structural displacement is projected from the structure to the fluid surface. Such data transfer across the interface is repeated multiple times over a single time step, and predominantly leads to two types of errors in the data transfer: (a) error during a single transfer from one surface to another across a non-matching mesh, and (b) error resulting due to repeated transfers. These errors are analyzed and assessed for the common-refinement projection scheme in this section.

7.4.1.1 Static Data Transfer

The first type of error resulting from a single transfer of data across the interface consisting of non-matching meshes is investigated here. Two intact surfaces with different mesh sizes are employed for quantification of this error, one of which is termed as fluid boundary and the other surface represents the deformable structure/solid. The geometry of both the surfaces resembles a circular cylinder with diameter $D = 1$ and height $H = 100D$, as shown in Fig. 7.11(a). The surfaces are discretized into $w_z = 36$ uniform elements in the Z-direction. Along the circumference of the cylinder, the surface is discretized into N_s and N_f uniform elements. Thus, the total number of elements on the fluid and solid surfaces are $w_z N_f$ and $w_z N_s$, respectively. A typical patch of the non-matching fluid and solid surface meshes is shown in Fig. 7.11(b).
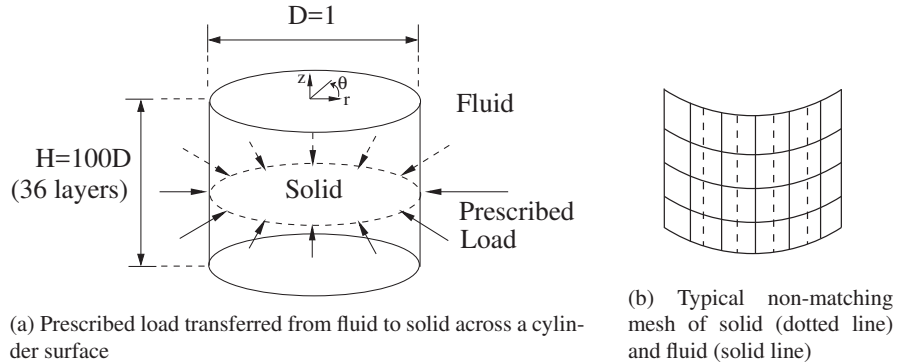

(a) Prescribed load transferred from fluid to solid across a cylinder surface

(b) Typical non-matching mesh of solid (dotted line) and fluid (solid line)

Fig. 7.11 3D non-matching meshes for static error analysis of common-refinement method.

The size of the element on each surface is defined by the area of each element as

$$A_s = \frac{\pi DH}{w_z N_s}, \quad A_f = \frac{\pi DH}{w_z N_f}. \tag{7.64}$$

Furthermore, the degree of non-matching meshes along the fluid-structure interface is given by the mesh ratio between the two surfaces, A_s/A_f. Various mesh refinements are generated by $N_s, N_f \in \{36, 54, 108, 162, 216\}$ leading to the mesh ratio of $A_s/A_f \in [1/6, 6]$. For the static load data transfer, a prescribed load is applied on the nodes of the fluid surface mesh at position x^f, which is then transferred to the structural surface mesh by the common-refinement technique. This is carried out for each set of the generated meshes. The prescribed load is given by the estimation of the static pressure along the Z-direction generated by a potential flow around the cylinder as

$$\boldsymbol{t}^s = \boldsymbol{t}^s(\theta, z) = -\left(\frac{1}{2} \rho^f U_\infty^2 (1 - 4\sin^2 \theta) + \rho^f gz \right) \begin{pmatrix} 0.5\cos\theta \\ 0.5\sin\theta \\ 0 \end{pmatrix} \tag{7.65}$$

where $(\theta, z) \in \Gamma^{fs}$ is the cylindrical position vector on the surface of the cylinder and $U_\infty = 1$. The origin of the cylindrical coordinates lies at the center of the top surface of the cylinder. Let (θ_j^s, z_j^s) be the position vector of node j on the solid surface mesh and $\boldsymbol{T}_j^s$ be the corresponding load transferred to that node, then the relative error ε_1 is quantified as

$$\varepsilon_1 = \frac{\sum_j ||\boldsymbol{T}_j^s - \boldsymbol{t}^s(\theta_j^s, z_j^s)||_2}{\sum_j ||\boldsymbol{t}^s(\theta_j^s, z_j^s)||_2}, \tag{7.66}$$

where $||\cdot||_2$ is the ℓ_2 norm. This error is computed for each mesh ratio ranging from 0.1667 to 6.0 and is summarized in Table 7.1. It can be observed that the common-refinement projection performs well within the interpolation error for all the mesh ratios. It is worth to note that the error is consistent for both $h_s/h_f > 1$ and $h_s/h_f < 1$ as the overlay mesh surface constructed in the common-refinement method involves both the fluid and the structural meshes.

A spatial convergence study is also carried out to further analyze the common-refinement technique by considering $h_s/h_f = 1.5$ and $h_s/h_f = 0.6667$ as the reference mesh ratios. Both N_s and N_f are increased simultaneously while keeping the mesh ratio fixed to reduce the error introduced by the spatial discretization. The relative error ε_1 computed for the mesh convergence is shown in Fig. 7.12. The slope of the convergence plot shows a second-order convergence rate implying that the common-refinement method is optimally accurate up to the geometric interpolation.

Capability of the common-refinement projection to handle different mesh shapes is assessed by considering a transfer of data from a triangular (fluid) to a quadrilateral (solid) mesh. The traction on the fluid mesh is prescribed as given by Eq. (7.65) and the error is computed by Eq. (7.66). Different mesh sizes (h ranging from 0.04 to 0.2) are employed for the study and the error is shown in Fig. 7.13, where

Table 7.1 Dependence of load vector error ε_1 on different mesh ratios h_s/h_f

N_s	N_f	A_s/A_f	Error, ε_1
36	216	6.0	2.94896×10^{-3}
36	162	4.5	2.88308×10^{-3}
36	108	3.0	2.69495×10^{-3}
36	54	1.5	1.6836×10^{-6}
36	36	1.0	2.51×10^{-16}
54	36	0.6667	1.76919×10^{-6}
108	36	0.3333	3.30083×10^{-3}
162	36	0.2222	3.29819×10^{-3}
216	36	0.1667	3.32599×10^{-3}
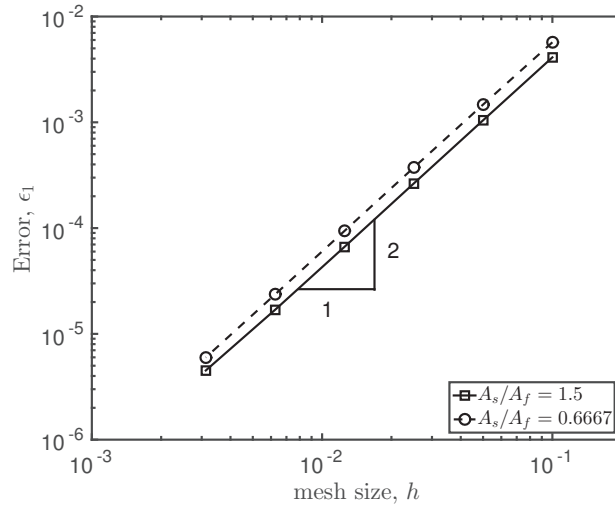
Fig. 7.12 Spatial mesh convergence study of common-refinement method for non-matching meshes.

a second-order of accuracy is obtained for load transfer across meshes of different shapes, thus demonstrating the generality of the technique.

7.4.1.2 Transient Data Transfer

This section analyses the second error resulting from the repeated transfer of data across the non-matching meshes. To accomplish this, a long deformable cylinder in a flow channel is considered with varying degrees of mismatches along the fluid-structure interface. The schematic of the problem is shown in Fig. 7.14(a). The cylin-
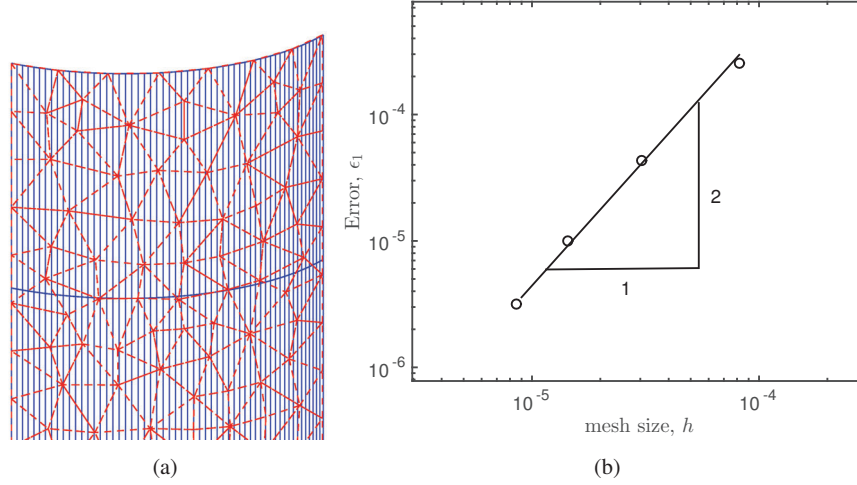
Fig. 7.13 Demonstration of common-refinement method for triangular-to-quadrilateral data transfer: (a) the representative surface meshes, and (b) the spatial error ε_1 versus mesh size h.

der has a diameter of D and is modeled as en elastic tube of length $50D$. The inlet and outlet boundaries are at a distance of $10D$ and $30D$ from the center of the cylinder, respectively. The ends of the cylinder are fixed at Γ_{top} and Γ_{bottom} boundaries. A freestream velocity of $u^{\mathrm{f}} = U$ is given at the inlet boundary Γ_{in}, where u^{f} is the X-component of the fluid velocity $v^{\mathrm{f}} = (u^{\mathrm{f}}, v^{\mathrm{f}}, w^{\mathrm{f}})$. A tress-free boundary condition is satisfied at the outlet boundary Γ_{out}. A slip boundary condition is imposed on Γ_{top} and Γ_{bottom}, while a no-slip condition is satisfied on the surface of the cylinder.

Similar to the static load data transfer, the fluid and the solid surfaces are decomposed into $w_\theta = 32$ and $w_z = 25$ elements along the circumference and the spanwise directions, respectively, giving a mesh ratio of $A_s/A_f = 1$, where the areas of the fluid and the solid elements are the identical. Then, a mismatch across the meshes is generated by fixing the fluid mesh and rotating the solid mesh along the spanwise axis of the cylinder. This kind of mismatch is depicted in Fig. 7.14(b). Corresponding to each fluid element k and the solid element j, a sub-element on the common-refinement interface is generated which is the intersection of the projected elements from both the subdomains. Consider $A_{k,j}$ to be the area of the sub-element corresponding to the fluid element k and the solid element j. Thus, the degree of mismatch with respect to the fluid element k ($\delta_k^{F \to S}$), can be defined as

$$\delta_k^{F \to S} = \left(1 - \frac{\max_j A_{k,j}}{\sum_j A_{k,j}} \right). \tag{7.67}$$

Furthermore, the degree of mismatch with respect to the fluid surface ($\delta^{F \to S}$) can be written as the mean of the degree of mismatch with respect to each fluid element, i.e.,